

Modelling the Dynamics of an Artificial Micro-swimmer in a Viscous Fluid



Priyanka

Department of Physics

Malaviya National Institute of Technology

This dissertation is submitted for the degree of

Doctor of Philosophy

February 2019

Dedicated to My Family

DECLARATION

I, **Priyanka**, declare that this thesis titled, “*Modelling the Dynamics of an Artificial Micro-swimmer in a Viscous Fluid*” and the work presented in it, are my own. I confirm that:

- This work was done wholly or mainly while in candidature for a research degree at this university.
- Where any part of this thesis has previously been submitted for a degree or any other qualification at this university or any other institution, this has been clearly stated.
- Where I have consulted the published work of others, this is always clearly attributed.
- Where I have quoted from the work of others, the source is always given. With the exception of such quotations, this thesis is entirely my own work.
- I have acknowledged all main sources of help.
- Where the thesis is based on work done by myself, jointly with others, I have made clear exactly what was done by others and what I have contributed myself.

Date:

Priyanka
2013RPH9028

CERTIFICATE

This is to certify that the thesis entitled “*Modelling the Dynamics of an Artificial Micro-swimmer in a Viscous Fluid*” being submitted by **Ms. Priyanka** (ID No. 2013RPH9028) is a bonafide research work carried out under our supervision and guidance in fulfillment of the requirement for the award of the degree of Doctor of Philosophy in the Department of Physics, Malaviya National Institute of Technology, Jaipur, India. The matter embodied in this thesis is original and has not been submitted to any other University or Institute for the award of any other degree.

Dr. Subhayan Mandal

Assistant Professor

Department of Physics

MNIT Jaipur (India)

Dr. Sujin Babu

Assistant Professor

Department of Physics

IIT Delhi (India)

Acknowledgements

Writing a PhD thesis is not an individual experience; rather it takes place in a social context and includes several persons, whom I would like to thank sincerely. Foremost, I want to offer this endeavor to our God Almighty for the wisdom he bestowed on me, the strength, peace of mind and good health in order to finish this research.

I express my sincere gratitude and the best regards to my supervisor Dr. Shubayan Mandal. He gave me the freedom to select a thesis topic which was unique to my abilities, and provided me wise guidance whenever I needed it. I am very thankful for his kind hearted, supportive and cooperative behavior during my entire journey.

I am heartily thankful and greatly indebted to my mentor Dr. Sujin Babu who proved to be a beacon holder by his constant supervision, guidance and endorsement by providing a secure and healthy environment by reflecting his enthusiasm and dynamism in this journey. In the backdrop of my Hindi background, he always read my texts patiently, pointed out my mistakes and assisted me with his great skills in structuring the papers and thesis. He was always a source of inspiration for me and under his umbrella I never felt disheartened during my PhD work at IIT Delhi.

I would take a deep sense of pleasure to express my thanks to the Department of Physics MNIT Jaipur and Department of Physics IIT Delhi in allowing me to work smoothly by facilitating me with all the necessary permissions like semester visit leave and computer center facilities at both the institutes. I would like to thank all the faculty members and technical staff of the Department of Physics MNIT Jaipur for their kind support and a special thanks to Dr. Kamlendra Awasthi for his help & support in this journey.

I would like to thank Isha Malhotra, research scholar at IIT Delhi, who was always there to help me whenever I was in need, even at times when she was consumed by her own PhD work. The unforgettable moments spent together, hers providing me mental support in stressful moments and always creating a positive and amicable environment

generated a bond of sisterhood with her. Her presence was enough to drive away the haunting negativities of mine in the pursuit of this journey. I would also take the chance to thank Mr. Hemant Kumar Suman (PhD student at IIT Delhi), Mr. Onkar Siyag (BTech student at IIT Delhi) and all the lab mates of the Einstein research scholar lab at IIT Delhi for their help and support.

A message of thanks is also conveyed to my friends Nisha Goyal, Nishu Kansal and Dr. Yogita for ineffable moments spent together, for their kind and moral support and being always available with a solution to my problems. A special thanks to Mr. Lokesh Jangid for sharing his technical knowledge in this research. I would also like to thank all my lab mates from Theoretical and computational lab, MNIT Jaipur, all research scholars of Department of Physics, MNIT Jaipur, especially, Mr. Rajesh Kumar, Mr. Himanshu Sharma and Mr. Shushant Kumar Singh for their help and support.

From the deep of my heart, I am thankful to my parents and my in-laws who always encouraged me to pursue my goals and for always being my strength to face every difficulty and challenge in my research. At last but not the least, I want to give a big thank to the person who has travelled this journey with me and keep motivating me to be on track every time. He is always like a pillar of strength in my life. The most important person in my life, my husband, Mr. Pourush Potalia, thank you so much for everything. This journey was not possible without your support.

(PRIYANKA)

Abstract

As we know that in a low Reynolds number regime the swimming strategies those are used in high Reynolds number regime are inefficient because of the dominating viscous forces. Therefore, micro-swimmers have developed different moving strategies that have successfully overcome and have exploited drag. In the present study, we are proposing a new artificial swimmer, which we call a one-hinge swimmer. Here, we show that at low Reynolds number the flexibility plays a crucial role to break the Scallop theorem in the case of one-hinge swimmer. To model a one-hinge artificial swimmer, we use bead spring model. To make the arms of the swimmer semi-flexible, we use a three body bending potential. The two semi-flexible arms of the swimmer are joined by a hinge and a bending wave potential provides the opening & closing to the swimmer. The dynamics of the swimmer is studied in a two dimensional Newtonian fluid. The fluid is simulated using a particle based mesoscopic simulation method known as the multi-particle collision dynamics with Anderson thermostat. Here, we show that when the swimmer has rigid arms, it performs reciprocal motion and due to that it is not able to propel itself as expected from the Scallop theorem. Instead of rigid arms, if we consider semi-flexible arms, the time reversal symmetry breaks in the case of the one-hinged swimmer. At first, we consider that both the arms have same bending rigidity (symmetric arms). We find that in case of symmetric arms, the swimmer follows the straight swimming trajectory. We calculate the scaled velocity of the swimmer for parameters like bending rigidity, amplitude and beating frequency. We show the flow field created by the swimmer. We also calculate the dimensionless Sperm number for the swimmer and get the maximum velocity when the Sperm number is around ~ 1.8 .

Further, we show that the arrangements of the bending rigidity along the arms of the swimmer can change the dynamics of the swimmer. To do so, we consider a non-uniform distribution of the bending rigidity K_b along the arms. Where we progressively change

the bending rigidity in a geometric sequence and show that this pattern can enhance the swimming speed. Next, we show that when the arms of the swimmer have different bending rigidity (asymmetric arms), then instead of straight path it follows the circular path. The direction of the circular pattern depends upon the combination of the bending rigidity of both the arms. Here, we obtain the swimming trajectories, rotation rate and dependency on the amplitude & the sperm number S_p of the swimmer. We show that when one of the arm is pretty rigid and second has moderate rigidity with $S_p \sim 1.8$, this combination creates maximum rotation rate and the swimming trajectory has larger curvature here.

Hydrodynamic interactions due to the objects in the vicinity are also one of the ingredients that can make a micro-swimmer motile. To show the importance of such kind of hydrodynamic interactions, here we investigate a 2-D rigid one-hinge swimmer near no-slip boundaries. Here, we show that if we place a scallop near a wall, it gets rotated and the direction of rotation depends upon the orientation of the scallop as expected. Instead of one wall, if we place the scallop between two closely spaced walls, initially it rotates and then slowly starts moving in backward direction due to the hydrodynamic interaction with the walls. Then we show that how the speed of the scallop is affected as we change the width of the channel.

Further, we study the dynamics of the swimmer in three dimensions, where we consider a width of the swimmer. Now the swimmer is similar to a 3-D flexible scallop. The scaled velocity of the 3-D scallop is studied as a function of width W of the flaps, where we show that by varying the width we can change the dynamics of the swimmer. Since the width plays an important role, we further consider a well known Taylor sheet model with a finite width. To model the waving Taylor sheet, we use bead spring model with the bending potentials. To consider the hydrodynamic interaction between the beads, we employ the Rotne-Prager mobility tensor. We show that for the rectangular sheet the frequency of the undulation is proportional to the velocity also the flow field created by the sheet is the similar to that of the infinitely long Taylor sheet. In the present study, we also show that the ratio of the perpendicular and parallel friction coefficient is no longer a constant but varies with the dimensions of the sheet. The stroke efficiency of the swimmer is also calculated for different lengths and widths.

Table of contents

List of tables	xvii
List of figures	xix
List of Abbreviations	xxv
1 Introduction	1
1.1 Low Reynolds number swimming	2
1.1.1 Overview of swimming mechanisms of the micro biological entities	3
1.1.2 Basic swimming strategies of the artificial micro-swimmers . . .	6
1.2 Motivation	8
1.3 Objectives of the thesis	10
1.4 Overview of the thesis	10
2 Literature review	13
2.1 Fluid dynamics	13
2.1.1 Fluid properties	13
2.1.2 Continuum hypothesis	16
2.1.3 Continuity equation	16
2.1.4 Navier-Stokes equations	17
2.2 Life around scallop theorem	21
2.3 Flagellar swimming	23
2.3.1 Taylor sheet	23
2.3.2 Slender-body hydrodynamics	24
2.3.3 Theory of the flexible filament	26
2.4 A brief literature review	28

3	Modelling and simulation techniques	35
3.1	Multi-Particle Collision Dynamics	36
3.1.1	Streaming step	36
3.1.2	Collision step	37
3.1.3	Grid shifting	38
3.1.4	Angular momentum conservation	39
3.1.5	Expressions for transport coefficients	40
3.1.6	Boundary Conditions	41
3.1.7	Brownian MPC	44
3.2	Modelling of the swimmer	45
3.2.1	2-D one-hinge or scallop swimmer	45
3.2.2	3-D scallop swimmer	46
3.2.3	3-D Taylor sheet	48
3.3	Coupling of the swimmer with the fluid particles	50
3.4	Implementation	50
4	Locomotion of a flexible one-hinge swimmer in Stokes regime	53
4.1	Introduction	54
4.2	Results	56
4.2.1	Breakdown of the time inversion symmetry	56
4.2.2	Mean square displacement	57
4.2.3	Flow field	60
4.2.4	Effect of Flexibility	61
4.2.5	Beating frequency	63
4.2.6	Amplitude of the actuation	64
4.2.7	Sperm number	65
4.3	Discussion	68
4.4	Conclusions	69
5	An exploration of one-hinge self-propelled swimmer in stokes flow	71
5.1	Introduction	72
5.2	Results and discussion	73
5.2.1	Constant but asymmetric rigidity	73

5.2.2	Varying but symmetric rigidity	82
5.3	Conclusions	85
6	Swimming of a 3-D elastic scallop in a viscous fluid	87
6.1	Introduction	87
6.2	Results and discussion	89
6.2.1	Enhanced diffusion	89
6.2.2	Ballistic motion	90
6.2.3	Speed	91
6.3	Conclusions	93
7	Swimming of a waving sheet in a viscous fluid	95
7.1	Introduction	95
7.2	Results and discussion	97
7.3	Conclusions	104
8	Conclusions and Future Scope of Work	105
8.1	Conclusions	105
8.2	Future scope of the work	107
	References	113
	Appendix	122

List of tables

3.1	Units associated with MPC algorithm.	51
-----	--	----

List of figures

1.1	Pictorial representation of a micro surgeon (image source [1]).	2
1.2	Pictorial representation of micro-organisms. (a) Spermatozoon (image source [2]). (b) Escherichia coli (image source [3]). (c) Caulobacter (image source [4]). (d) Rhodobacter sphaeroides (image source [5]). . .	4
1.3	Pictorial representation of micro-organisms. (a) Spirochetes (image source [6]). (b) Paramecium (image source [7]). (c) Chlamydomonas reinhardtii (image source [8]). (d) Spiroplasma (image source [9]). . .	5
1.4	Here, in (a) a one-hinge swimmer is exhibiting reciprocal motion and in (b) a Purcell's two-hinge swimmer is exhibiting non-reciprocal motion. .	7
1.5	Theoretical swimmers adapted from Purcell's "Life at Low Reynolds numbers" [10]. (a) Corkscrew, (b) flexible oar and (c) the two-hinge swimmer.	8
1.6	Artificial micro-swimmers. (a) Swimmer with a passive head and a flexible tail (image source [11]). (b) Swimmer with two tails and without head.	9
2.1	Flow profile between two parallel planes (image source [12]).	14
2.2	Momentum diffusion of fluid particles between two parallel planes. One of the plane is stationary and the other one is moving at velocity \mathbf{V} (image source [12]).	15
2.3	Representation of viscous stresses and pressure that are acted on a fluid element (image source [12]).	18
2.4	Motion of the scallop at low Reynolds number.	22
2.5	Resistive force theory relates the local viscous force to the local velocity in terms of the resistive or drag coefficients (image source [13]).	24

2.6	Flexible filament, where base of the filament is situated at the origin. The shape of the filament is given by the position vector $\mathbf{r}(s)$. Inset shows ds length element of the filament and local angle ψ (image source [14]).	26
2.7	Deformation of a single filament as the value of Sperm number changes, obtained from our simulations.	29
2.8	Schematic representation of a flexible magnetic filament, proposed by Dreyfus et al [15].	30
2.9	Schematic of the nano-wire magnetic swimmer, proposed by Wei Gao et al [16].	30
2.10	Schematic of a biohybrid swimmer actuated by heart muscles, proposed by B. J. Williams et al [17].	31
2.11	Schematic of soft robotic light sensitive micro swimmer and light irradiation system, proposed by C. Haug et al [18].	32
2.12	Schematic of multi-filament swimmer. (a) Swimming with two symmetric filaments, in planer motion. (b) Swimming with six filaments in planar motion, proposed by E. Lauga [19].	33
3.1	The streaming step (algorithm 3.1)	37
3.2	Depiction of MPC-AT collision algorithm. (a) Sort particle into cells, (b) calculate the center of mass velocity \mathbf{u} of the cell, (c) for each particle generate a random velocity such that the center of mass velocity remains \mathbf{u} and (d) apply this new velocity to each particle.	38
3.3	Picture of random shift of the collision cell.	39
3.4	Periodic boundary conditions. The positions of particles that are outside the constrained area are shifted to the opposite end.	41
3.5	Schematic of a 2-D periodic boundary conditions. PBC's wrap the system.	42
3.6	Schematic of solid boundary conditions.	42
3.7	Inclusion of the virtual particles. In case of (a) virtual particles are not required and in (b) virtual particles are needed. In the figure, virtual particles are colored as yellow.	43
3.8	Distortion of hydrodynamic interactions (Brownian fluid) by randomly interchanging the velocity of the solvent particles.	44

- 3.9 The snapshot of a model one-hinge artificial swimmer with flexible arms. Three mass points are given blue color to show that the bending waves pass through only these three points. We have magnified the bond vectors \mathbf{t}_i and \mathbf{t}_{i+1} , which connect neighboring mass points and make an angle θ . φ is the angle between two arms near the hinge. 45
- 3.10 The schematic for 3-D model scallop; here middle beads are given in red color to show that the bending waves pass only through these beads. The blow up (i) illustrates that nearest and next nearest beads are connected with spring potential; blow up (ii) shows the bond vectors \mathbf{t}_i and \mathbf{t}_{i+1} which connect neighboring beads and makes an angle θ 47
- 3.11 (a) Snapshot of waving sheet swimmer as obtained from the simulation. (b) Magnification of bond vectors between the beads and θ is the angle between the bond vectors along the width. (c) 2-D projection of the sheet that depicts two wave trains each having wavelength λ 48
- 3.12 Coupling of the swimmer with fluid particles, where fluid particles can pass through the swimmer body. 50
- 4.1 Sequence of conformation of the arms (here different colors are used just for the better visualization) of the one-hinged swimmer over one complete beat cycle, (a) represents the case for a flexible arms and (b) for the case of rigid arms. From right to left, we observe the sequence of closing, from the center bold conformation shows the opening of the arms of the swimmer. The black arrow at the top shows the direction of swimming for the flexible swimmer. 58
- 4.2 MSD of a rigid scallop of arm length $L = 15$ in four different boxes (box sizes are mentioned in figure). Here solid black line has slope one. . . . 60
- 4.3 Mean square displacement of the center of mass position of the swimmer is plotted as a function of time t for the flexible arms (blue) and rigid arms (red). The solid line has slope of 1 indicating diffusive motion and dotted line has slope of 2 representing directed motion of the swimmer. 61
- 4.4 Flow field created by a flexible one-hinge swimmer (thin black line). Here, solid black arrow shows the direction of the swimming. 62

- 4.5 The reduced velocity of the swimmer is plotted as a function of bending rigidity of the arms of the swimmer. 63
- 4.6 The reduced velocity is plotted as a function of frequency of the actuation. The solid line has slope of one as predicted for the small amplitude approximation. 64
- 4.7 $\Delta\varphi$ (in radian) is plotted as a function of the amplitude of actuation. The dashed line shows the linear fit given by $(0.43A/a_0 + 0.1)$ 66
- 4.8 Reduced velocity of the swimmer is plotted as a function of $\Delta\varphi$ (in radian), the dashed line (inset) has slope of two as predicted for small amplitude approximation. 66
- 4.9 The reduced velocity of the swimmer is plotted as a function of Sperm number. The value of S_p was varied by changing ν (square), L (circle) and k (triangle), keeping all other parameters same. 67
- 5.1 Schematic of one-hinge swimmer. (a) Both the arms of the swimmer are symmetric and have uniform bending rigidity. (b) Arms are not symmetric. Left arm has bending rigidity K_{b_l} and right has K_{b_r} , though the bending rigidity K_{b_l} & K_{b_r} along the arms are uniformly distributed. (c) Arms are symmetric but bending rigidity along the arms is non-uniform. Bending rigidity is arranged in such a way that it reduces from hinge to edge in a geometric sequence. We can see that near the edges, arms (green) are pretty flexible as compared to the symmetric uniform arms (red), though in both the cases average bending rigidity is same. Three beads are given black color to show that the bending wave potential U_w is applied only on these three beads. The black solid arrow shows the direction of the motion. 74
- 5.2 Trajectories of the swimmer for three different cases where the curvature between the arms changes as $\alpha = A \sin(2\pi\nu t)$. (a) $K_{b_l} = 10^7$, $K_{b_r} = 3 \times 10^5$ and swimmer propels toward left arm. (b) $K_{b_l} = 5 \times 10^4$, $K_{b_r} = 3 \times 10^5$ and swimmer propels toward right arm. (c) $K_{b_l} = 3 \times 10^5$, $K_{b_r} = 3 \times 10^5$ and swimmer perform only diffusive motion 76

- 5.3 Trajectories of the swimmer for three different cases where the curvature between the arms changes as $\alpha = A \sin^2(2\pi\nu t)$. (a) When $K_{b_l} = 10^7$, $K_{b_r} = 3 \times 10^5$ and swimmer has left hand rotation. (b) When $K_{b_l} = 5 \times 10^4$, $K_{b_r} = 3 \times 10^5$ and swimmer has right hand rotation. (c) When $K_{b_l} = 3 \times 10^5$, $K_{b_r} = 3 \times 10^5$ and swimmer has no rotation, it follow straight swimming trajectory 77
- 5.4 Angular velocity w of an asymmetric swimmer for different values of K_{b_r} while keeping $K_{b_l} = 10^7$ (extremely stiff). K_{b_l} and K_{b_r} are the bending rigidities of the left arm and right arm respectively. 78
- 5.5 Trajectories of an asymmetric swimmer for three different values of K_{b_r} while keeping $K_{b_l} = 10^7$. Here K_{b_l} is always greater than K_{b_r} . Due to that swimmer always follows a left circular pattern. 78
- 5.6 Angular velocity of an asymmetric swimmer for different values of K_{b_r} while keeping $K_{b_l} = 5 \times 10^4$ (very flexible). 79
- 5.7 Trajectories of an asymmetric swimmer for different values of K_{b_r} while keeping $K_{b_l} = 5 \times 10^4$. Here K_{b_r} is always greater than K_{b_l} which results into right circular trajectories. 80
- 5.8 Angular velocity of an asymmetric swimmer for different values of K_{b_r} , while keeping $K_{b_l} = 3 \times 10^5$ (moderate). The black crossed point is used in case of symmetric arms ($K_{b_r} = K_{b_l}$). 81
- 5.9 Trajectories of an asymmetric swimmer for different values of K_{b_r} , while keeping $K_{b_l} = 3 \times 10^5$ (moderate). When $K_{b_l} > K_{b_r}$, swimmer follows a left circular pattern and if $K_{b_r} > K_{b_l}$ it moves in a right circular pattern. When $K_{b_l} = K_{b_r}$ (symmetric arms) swimmer goes along a straight path (black). 83
- 5.10 Angular velocity w of an asymmetric swimmer for different values of amplitude A , while keeping all other parameters fixed. 84
- 5.11 Scaled velocity is plotted as a function of R_{K_b} . R_{K_b} = ratio of bending rigidity at hinge bead to bending rigidity at edge bead. The crossed point is used for the case of uniform bending rigidity. 85

5.12	Scaled velocity is plotted as a function of Sperm number. The blue curve and pink curve represent uniform flexibility and varying flexibility along the arms of symmetric swimmer respectively.	86
6.1	Mean square displacement (MSD) of the center of mass is shown as a function of time t for two different cases. One, where the scallop is opening and closing its shells with reciprocal motion with a diffusion coefficient $D \approx 0.004$ and second, where scallop is passive and only thermal fluctuation is there ($D \approx 0.001$).	90
6.2	Mean square displacement (MSD) of the center of mass is shown as a function of time t for an elastic scallop.	91
6.3	The reduced velocity of the scallop is plotted as a function of bending rigidity K_{b_L} along the length of the scallop flaps.	92
6.4	The reduced velocity of the scallop is plotted as a function of Width W of the flaps of an elastic scallop.	93
7.1	Mean square displacement of the center of mass of sheet for $L = 30$ and $W = 3$ as a function of time. The dotted line has a slope of 2, as expected for ballistic motion.	98
7.2	Center of mass velocity of the sheet for $L = 40$ and $W = 1$ as a function of frequency, inset shows the dependency of velocity on frequency in log scale. The dotted line in the inset has slope of one.	99
7.3	Flow field created by the waving sheet. In (a) different colors are shown to explain flow field (see text). The green arrow shows the direction of wave propagation and yellow arrow shows the direction of motion of the sheet. The red arrows represent the unit vector of velocity obtained from simulation.	100
7.4	The ratio of friction coefficient of the swimmer as a function of length of the swimmer for 3 different widths.	101
7.5	The center of mass velocity of the swimmer as a function of the length of the swimmer for 3 different widths. The solid lines represent the analytical calculation from equation 7.2	102

-
- 7.6 Variation in stroke efficiency for the sheet swimmer for different lengths for 3 different widths. The lines are guide to the eyes. 103
- 8.1 Here (a) and (b) shows two different orientations of the initial position of the swimmer near a single wall, where the black arrows show the direction of rotation. When we place swimmer between two walls, in case of (a₁) & (a₂) initially the swimmer was oriented as shown in (a) and in case of (b₁) & (b₂) initially the swimmer was placed as shown in (b). In the beginning swimmer rotate toward any of the wall as indicated by the black arrow and after a rotation it start moving in backward direction as indicated by green arrows. 109
- 8.2 The reduced velocity is plotted as a function of the channel width. . . . 110

List of Abbreviations

2-D	Two dimensions
3-D	Three dimensions
BC	Boundary condition
DNA	Deoxyribonucleic Acid
DPD	Dissipative particle dynamics
HI	Hydrodynamic interaction
LDLC	Light driven liquid crystal
MD	Molecular dynamics
MPC	Multi-particle collision dynamics
MPC-AT	MPC with Anderson thermostat
MPC-AT+a	MPC-AT with angular momentum conservation
MPC-AT-a	MPC-AT without angular momentum conservation
PBC	Periodic boundary condition
RBC	Red blood cell
UV	Ultraviolet

Chapter 1

Introduction

Since the beginning of a journey of the technology, people have tried to replace the man power by machines. Though in the early stages these machines were giant, complicated to handle and also could perform only limited tasks, but nowadays we are approaching to micron size machines those are efficient, easy to handle and can perform multi-tasks. The ever decreasing world around us can be attributed to the technology advancement. Professor R. P. Feynman, for the first time, gave the idea of micron scale technology in his 1959 talk “There is Plenty of Room at the Bottom” [20]. In this talk, he dreamt of a day when machines could be miniaturized as well as a large amount of information could be stored in very small spaces. Feynman also shared one of his friend’s (Albert R. Hibbs) idea that it would be amazing in surgery if one could “swallow the surgeon”. The idea encompassed a situation in which the surgeon is in the form of an externally controlled very tiny machine, with a scalpel, that can go down inside the blood vessels, can examine the different organs and repair the faulty one or can perform the assigned task. The important question comes that how to make a small piece of mechanical machinery that can freely swim in the body fluid. Such a question arises because of various factors, such as the Reynolds number, those come into the picture due to the influence of the fluid, when the machine size changes from macro to micro. Especially, when we are taking into consideration the swimming case of micro-swimmers [10]. Nature has inspired human being in constructing various devices such as aeroplane model was inspired from pigeon wings, caterpillar movement inspired the construction of conveyor belt movement of

military tanks, many surgical instruments are designed from beaks of birds which provide a very precise grip and strength. One such inspiration for constructing micro-robots came from natural biological micro-swimmers such as bacteria, archaea, viruses, protists, etc. They are very small in size and still manage to swim in water and other dense fluids. So, the need arose to have a deep insight in the swimming dynamics of these micro-organisms to design the artificial micro-swimmers.

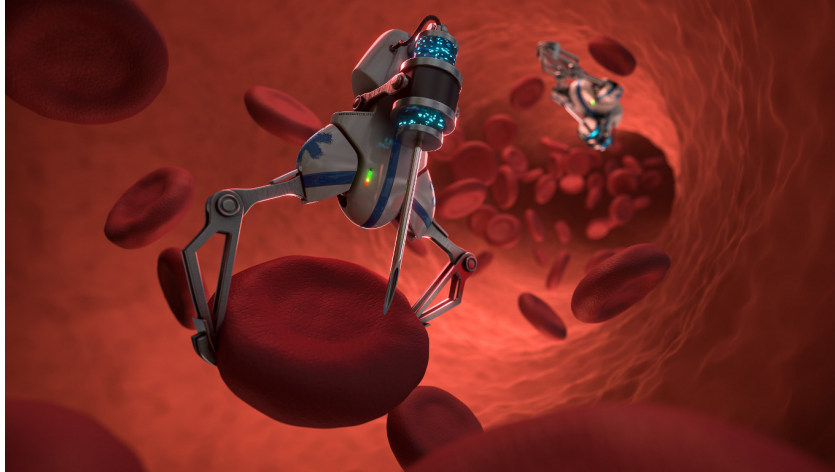


Fig. 1.1 Pictorial representation of a micro surgeon (image source [1]).

Due to huge application of engineering sciences in various sectors of human life, especially in the medical field, people have shown immense interest in the last few decades to study the dynamics of small scale creature and also have proposed many artificial models that work on the mechanism of these biological entities. Researches have leaped forward by constructing prototypes of artificial micro swimmers, but yet we have to wait for few more years till these artificial swimmers find their use in their desired fields.

1.1 Low Reynolds number swimming

The surpassing of viscous forces over inertial forces makes the physics of swimming at micron scale different as compared to macro level swimming. Just think about a situation when a man has jumped into a pool of corn-syrup. The man would find it difficult to swim in corn-syrup than water. This is due to the viscosity difference between corn-syrup and water. Now, if we imagine a situation where the size of the object is comparable to micro-organism and it is swimming in a pool of water, then the situation would be

analogous in terms of difficulty faced by the man swimming in a corn-syrup pool. This analogy is substantiated by the calculation of Reynolds number for both the cases. The Reynolds number is basically the ratio of inertial forces to the viscous forces and it turns out to be $Re = VL/\mu$, where L is the size of the object, V is the typical flow velocity around the object and μ is the kinematic viscosity of the fluid. Let us calculate the Re for different bodies that are surrounded by water. First, we consider a man having a body length $L = 1.7m$ is swimming at speed $V = 1.5m/s$ and the kinematic viscosity of the water $\mu = 10^{-6}m^2/s$ [21]. So, the Reynolds number comes around $Re \sim 10^6$. Here inertial forces are certainly high as compared to the viscous forces and that's why the value of the Reynolds number turns out to be high. Thus, a human in the water filled pool is a "high Reynolds number swimmer". Now let us calculate Re for tiny fishes. Consider a fish which swims at a rate $12mm/s$ and has a body length $60mm$ [22]. As size reduces inertial forces also reduce and Reynolds number comes around $Re \sim 10^3$. While calculating Re number for micron size bodies like bacteria, algae, viruses, etc., it comes out to be in order of 10^{-5} . For instance the bacterium *Escherichia coli* is about $2\mu m$ long and it swims with a typical speed $20\mu m/s$ [23]. This shows that as size decreases the inertia forces get neglected and viscous forces start dominating. Such swimmers are referred to as "Low Reynolds number swimmer" which is the domain of the thesis. Low Re flow is also known as Stokes-flow or viscous-flow and it shows different behavior that is unlike from that obtained in our inertial world.

1.1.1 Overview of swimming mechanisms of the micro biological entities

Most of the micro-organisms employ appendage for locomotion and the appendage can be one or multiple, also can be helical shaped or whip like. For example, the sperm cells have a flexible appendage, as shown in figure 1.2(a), which undergoes whip like motion because of the movement of the molecular motors that are allocated along the length of the appendage [24]. *E. Coli* bacterium has helical shaped appendages and the motor embedded in the cell wall rotates the helical flagellum [25]. The organelles of propulsion in *E. Coli* and *S. Typhimurium* are the bacterial flagella, where the helical flagellum is connected to the motor with the help of a hook [26–29]. These bacteria generally have a number of flagella attached to the cell body and when motor whirls anti-clockwise (from

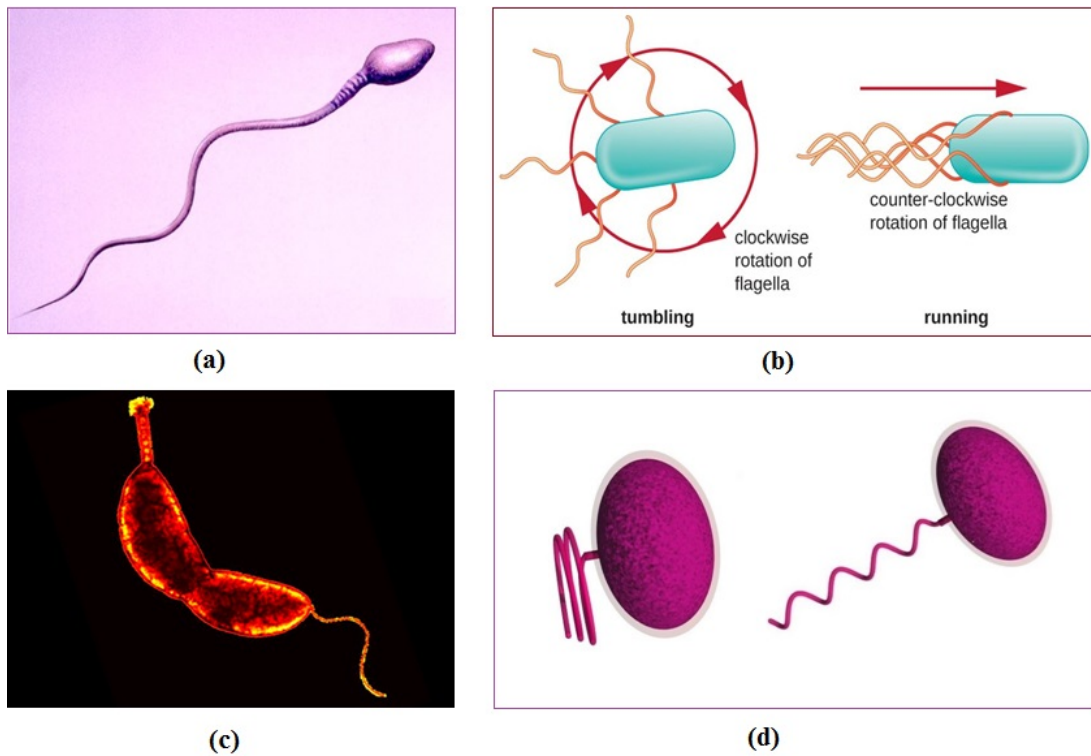


Fig. 1.2 Pictorial representation of micro-organisms. (a) Spermatozoon (image source [2]). (b) Escherichia coli (image source [3]). (c) Caulobacter (image source [4]). (d) Rhodobacter sphaeroides (image source [5]).

the outside view of the cell body) the flagella wrap into a bundle and produce a thrust that pushes the cell body as shown in figure 1.2(b) [30]. When any of the motor invert the direction of rotation, the related flagellum leaves the bundle which change the handedness and the direction of the propulsion as well [31].

There are many differences in the core mechanism of the bacterial swimming. For instance, *Caulobacter crescentus* (see figure 1.2(c)) bacterium has only right-handed helical flagellum that can whirl in either direction. The motor favorably whirls in clockwise direction and pushes the body in the forward direction [32]. An anti-clockwise whirl of the flagellum pulls the cell body rather than pushing. The *Rhodobacter sphaeroides* whirls in a single direction and when the attractant concentration is increased there is no change in rotational behavior. But when an attractant is removed, the motor stop transiently [33]. This shows that rather than swimming and tumbling, *Rhodobacter sphaeroides* take a halt from time to time [34]. When motor comes to a halt, the flagellum of the bacterium makes a compress coil shape and when motor again whirls, the flagellum come back into helical shape as shown in figure 1.2(d). Many archaea also utilize the rotating flagellum

to propel, but archaeon like *Halobacterium* propel at a very slow pace as compared to the bacteria [35]. Though similar to bacteria, archaea also contain a rotary motor, filament and a hook that connects the motor with the filament but molecular analysis exhibits that flagella of archaea and bacteria are not similar [36].

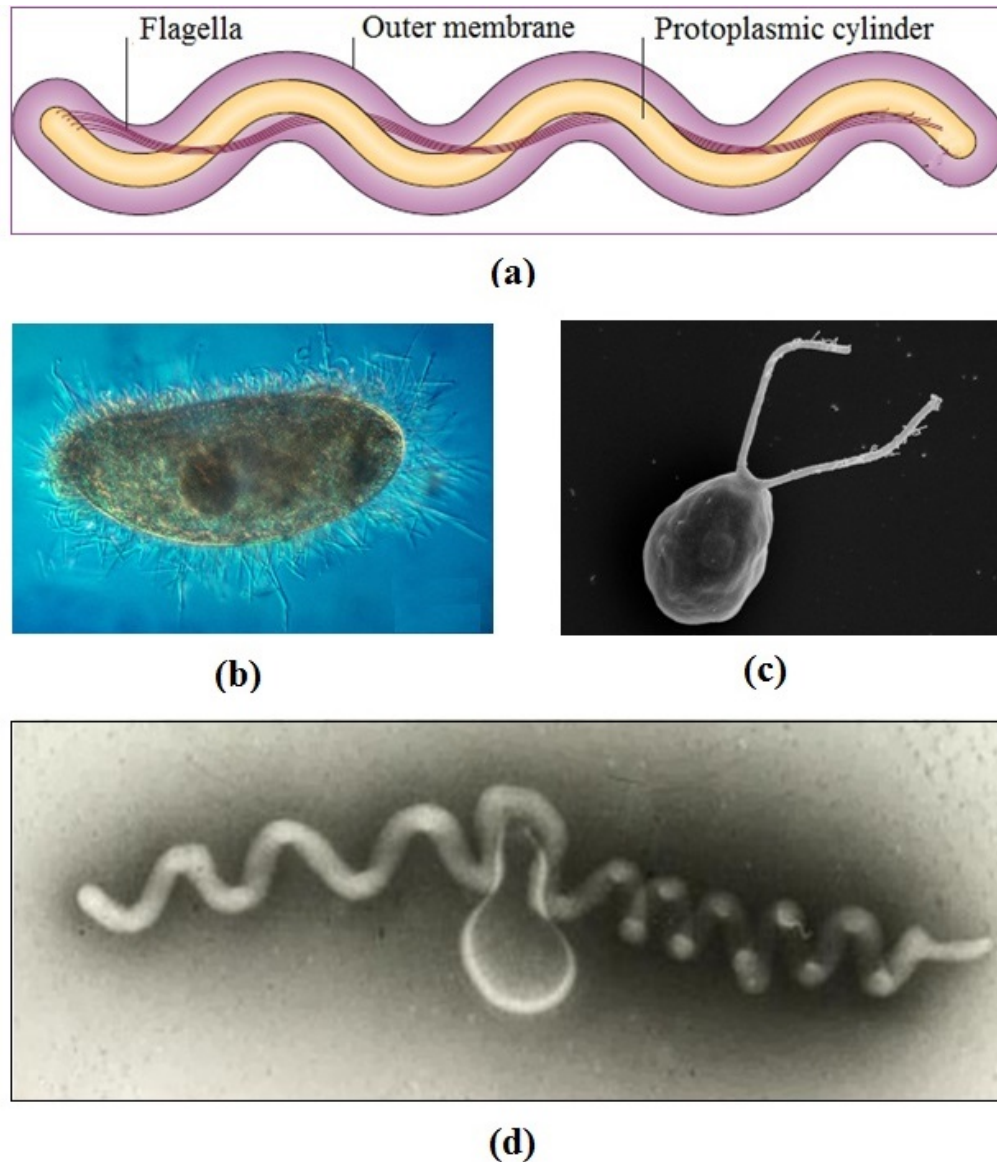


Fig. 1.3 Pictorial representation of micro-organisms. (a) Spirochetes (image source [6]). (b) Paramecium (image source [7]). (c) *Chlamydomonas reinhardtii* (image source [8]). (d) *Spiroplasma* (image source [9]).

There are several bacteria that can propel without external flagella. The spirochetes bacteria have flagella that dwell inside the fine periplasmic area between the outer and inner cell membranes as shown in figure 1.3(a) [37]. The flagella appear from the motor that is enclosed into the cell wall at both the poles of spirochete's body. The flagella wrap

around the spirochete's body and the flagellar filaments can be one or more depends upon the species type. In few conditions, like the Lyme disease spirochete *Borrelia burgdorferi*, the spirochete deforms its body and it is believed that the periplasmic flagella rotate which causes this shape distortion. This deformation successively provides the net propulsion to the body and the deformation may be planar or helical [38, 39]. The bacteria having internal flagella move faster in gel-type viscous environment as compared to the bacteria having external flagella [40, 41]. Another spirochetes, for example *Treponema primitia*, don't deform their body for motion and it is believed that propulsion is produced because of the contrary rotation of the cytoplasmic layer and outer layer [38, 42]. The bacteria *Spiroplasma* have a helical shaped body without any flagella (see figure 1.3(d)) and they employ pairs of kinks for propulsion [43]. These kinks generate due to the contraction of cytoskeleton [44–46].

There is a huge variation in the beating style of the flagella and cilia. Also the length of the same vary from species to species. For instance, the sperm cells of several organisms contain a head and a tail with planar or helical beating style [47]. Also the length of the flagella varies from a few micrometers to millimeters and a few even have centimeter long flagella [48–50]. The alga *Chlamydomonas reinhardtii* has two flagella as shown in figure 1.3(c). These can perform ciliary beating pattern as well as flagellar beating pattern. In the ciliary motion, each flagellum beats asymmetrically [24]. When the flagella perform the power-stroke, they extend and bend at the base similar to the breaststroke motion of the human and in recover-stroke *Chlamydomonas reinhardtii* fold its flagella. *Chlamydomonas reinhardtii* moves in the opposite direction when a bright light falls on it and now each of its flagellum extends and a bending wave passes through it [51]. *Paramecium* is also an excellent example of the micro-organism that contains a lot of cilia (see figure 1.3(b)). The surface of *paramecium* is fully seeded by abundant of cilia that deform in a coordinated pattern [52].

1.1.2 Basic swimming strategies of the artificial micro-swimmers

In highly viscous environment, for sustained self-propelled motion, the movement of the object should be continuous otherwise the viscous forces immediately dissipate the velocity produced by a single stroke. For instance, a micro-swimmer propelling

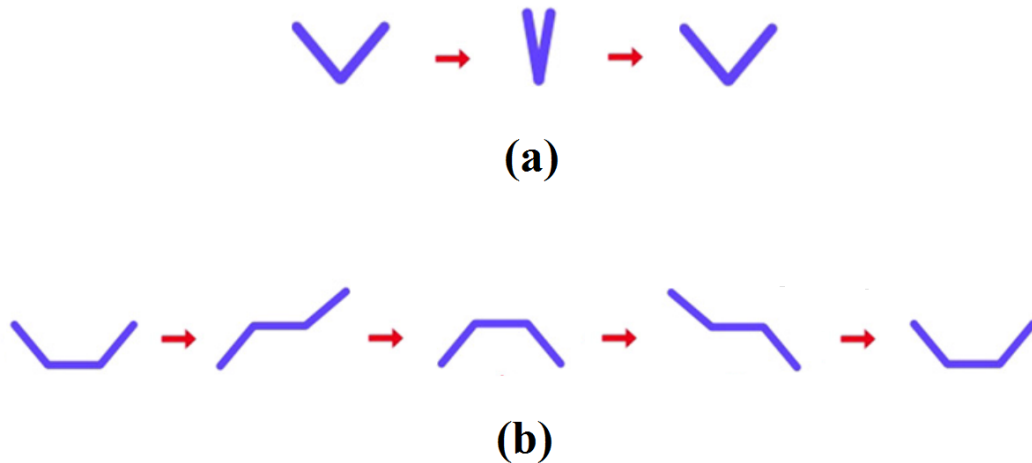


Fig. 1.4 Here, in (a) a one-hinge swimmer is exhibiting reciprocal motion and in (b) a Purcell's two-hinge swimmer is exhibiting non-reciprocal motion.

at speed $30\mu\text{m}/\text{s}$ in the water, suddenly stops its movement. After this it would coast around $0.1A^\circ$ and within $0.6\mu\text{s}$ it will come to the halt [10], which is unlike to the inertial world. So for sustained propulsion the movement strokes have to be cyclic. E. M. Purcell in his 1976 famous talk “Life at low Reynolds number” [10] demonstrated that at low Reynolds number regime, for self propulsion, the movements of the swimmer must not be reciprocal. He highlighted that in the inertia-less world ($Re \ll 1$) the Navier-Stokes equations of flow field reduce to Stokes equations, and because of time independence and the linearity of the Stokes equations if an object tries to move by a reciprocal motion its center of mass does not move, this is the so called Scallop theorem (detailed explanation is provided in the next chapter). If we track the different configurations of motion and the sequence looks identical if we inverse time, then it is a reciprocal motion. Figure 1.4(a) shows the reciprocal motion. Here we can see that the configurations of the swimmer look identical under time inversion. Purcell demonstrated that if an object has one-hinge, then it is bound to do reciprocal motion as shown in 1.4(a). But a “two-hinge swimmer” can perform non-reciprocal motion and hence can break the Scallop theorem. In figure 1.4(b), we can observe that configurations of the two-hinge swimmer are not identical under time inversion. Also, by inspiring from the swimming strategies of the micro-biological entities, Purcell suggested two simple ways to break the Scallop theorem at low Reynolds number that are “corkscrew” motion and “flexible oar” motion.

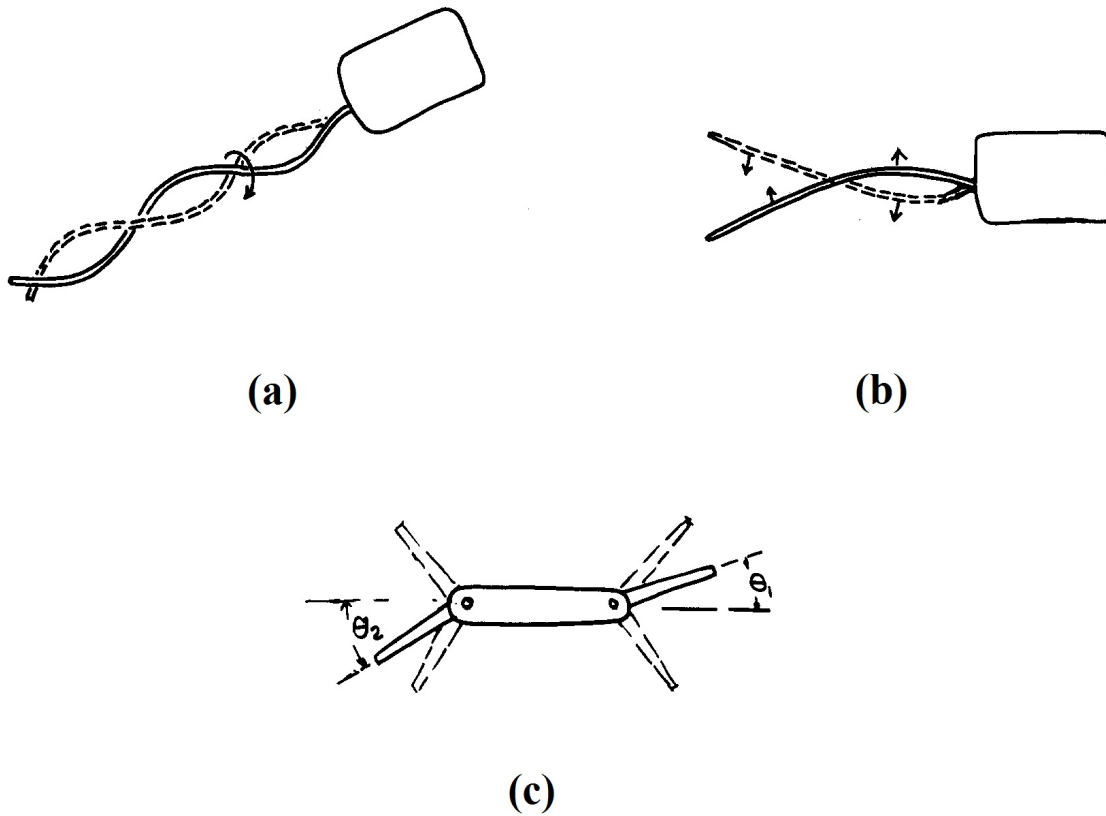


Fig. 1.5 Theoretical swimmers adapted from Purcell’s “Life at Low Reynolds numbers” [10]. (a) Corkscrew, (b) flexible oar and (c) the two-hinge swimmer.

All three proposed movements by Purcell those work at low Reynolds number are shown in figure 1.5. On the basis of these basic swimming strategies many artificial swimmers have been proposed theoretically and realized experimentally as well [11, 15, 18, 19]. We will briefly talk about these artificial swimmers in the next chapter. The present thesis is mainly focused on the “flexible oar” kind of motion.

1.2 Motivation

Study of the swimming at Stokes regime enhances our knowledge of biological systems. It provides us a deeper insight of the dynamics of biological swimmers and how surrounding boundary conditions affect the dynamics of these swimmers. It helps us to construct the new bio-inspired mechanical devices and is also important to improve the performances like enhancement of velocity, efficiency and functionality of the previously built bio-constructs [17, 53–55]. As we have discussed earlier, these artificial micro-swimmers could provide propulsion for medical payloads, and therefore can be employed

for a variety of purposes in the medical field. These can be used for targeted drug delivery, cancer detection and its treatment, minimally invasive surgery, breaking up kidney stones, removal of the defected parts in DNA structure, parasite removal, clearing away the blood clots and so on. Nowadays scientists are imagining a day of nano-medication when people could be close to immortality.

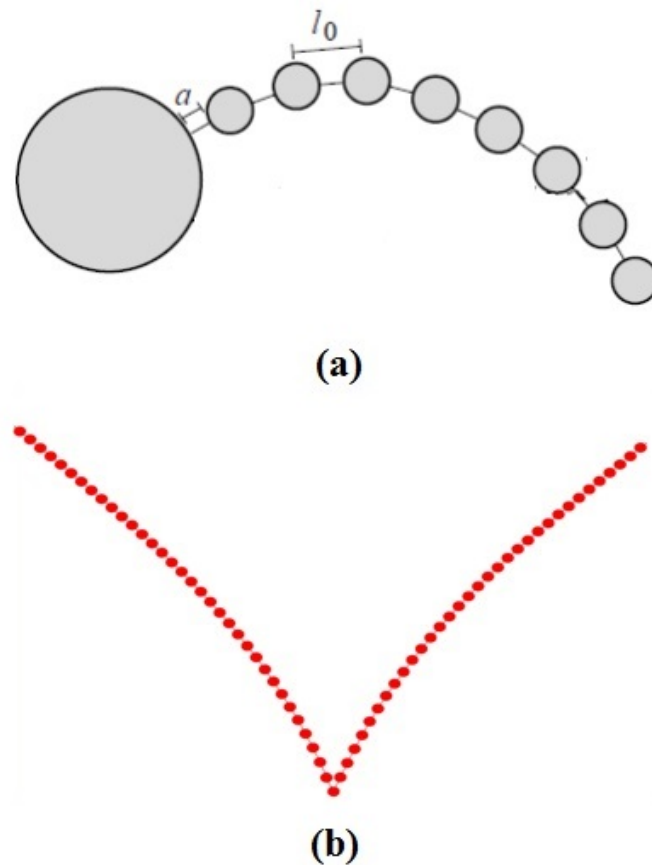


Fig. 1.6 Artificial micro-swimmers. (a) Swimmer with a passive head and a flexible tail (image source [11]). (b) Swimmer with two tails and without head.

To construct an artificial micro-swimmer the main challenges are: *i*) break-down of the Scallop theorem which leads to self propulsion, *ii*) employment of energy sources, and *iii*) provide control or intelligence to the swimmer [56–58]. In the present thesis, we have proposed a new artificial swimmer known as “one-hinge swimmer”. The one-hinge swimmer contains two arms that are connected via a hinge. To break the Scallop theorem, swimmer exploits elasticity of the arms. To provide the propulsion to the swimmer, we have employed a bending wave potential which ensures that total applied force and torque on the body is zero. So any external energy or external field is not required here. Most of

the previously proposed flexible swimmers contain a single tail and a head [15, 18, 19]. In figure 1.6(a), we have shown a simple one head and single tail swimmer. Here, head is essential to break the Scallop theorem [11, 15]. The passive head increases the drag, which reduces the swimming velocity. But in the case of our one-hinge swimmer (see figure 1.6(b)), the Scallop theorem can be broken without a passive head [19]. Initially, we have considered that both the arms of the swimmer have same bending rigidity and are positioned exactly symmetrically with respect to the axis of symmetry, or are mirror image of each other. Then all transverse forces due to one arm are exactly canceled by the second arm. This results in a straight swimming trajectory, which is an advantage over a single arm swimmer. Further, we have considered that both the arms have different bending rigidity, wherein we have taken various combinations of the bending rigidity for both the arms, which changes the direction of the swimming.

1.3 Objectives of the thesis

The main objectives of the present work are as follows

- Model an artificial low Reynolds number swimmer that exploits elasticity for propulsion (using bead-spring model).
- Simulate the designed model in a viscous solvent using the method of multi-particle collision dynamics with Anderson thermostat.
- Study a two dimensional active swimmer after introducing a beating procedure for the swimmer.
- Establish a theoretical framework for such a swimmer.
- Optimization of simulation parameters and improve the performance of the swimmer.
- Study the dynamics of a three dimensional active swimmer.

1.4 Overview of the thesis

In the present thesis, we are studying the dynamics of an artificial low Reynolds number swimmer in a Newtonian fluid. The thesis is organized as follows:

- **Chapter 2 :-** “*Background*”. In this chapter, we will briefly discuss the basic topics of the fluid dynamics that are essential for the understanding of the dynamics of the low Reynolds number swimmers. We will also provide a brief literature review of the artificial swimmers which will contain the brief overview of the theoretical, experimental and simulation based studies. In this, we will mainly focus on the artificial swimmers that perform the flexible oar kind of motion.
- **Chapter 3 :-** “*Modelling and simulation techniques*”. In this chapter, we will talk about the advantage of the coarse grained simulation method known as multi-particle collision dynamics with Anderson thermostat (MPC-AT). This technique includes hydrodynamic interactions with thermal fluctuations and momentum conservation. Then we will provide a brief understanding of the MPC-AT technique, where we will explain how Anderson thermostat works and how one can conserve the angular momentum in MPC-AT. We will also explain how hydrodynamic interactions can be turned off in MPC. Next we will discuss about the implementation of the boundary conditions. In this chapter, we will explain the modelling of our artificial swimmers and also the coupling of the swimmer with the fluid environment. Further, we will explain how the code is implemented.
- **Chapter 4 :-** “*Locomotion of a flexible one-hinge swimmer in Stokes regime*”. In this chapter, we will show how a one-hinge swimmer is able to break the Scallop theorem. We will illustrate the flow field created by a flexible one-hinge swimmer. Then we will vary different parameters and show how the dynamics of the swimmer changes with that. We will also try to provide the theoretical framework for the one-hinge swimmer, where we will show that when the Sperm number is around 2, then we can achieve the maximum velocity for the swimmer. Also, we will discuss how this artificial swimmer can be realized experimentally.
- **Chapter 5 :-** “*An exploration of one-hinge asymmetric swimmer in Stokes flow*”. In this chapter, we will show the dynamics of a one-hinge swimmer which has asymmetrical arms in terms of bending rigidity and therefore shape as well. An asymmetric swimmer follows a curved trajectory contrary to symmetric one-hinge swimmer that always follows a straight swimming trajectory. Here, we will show that by varying the combination of the bending rigidity along the arms, we can

change the direction of the swimming. We will also show that by varying the rigidity (non-uniform rigidity) we can improve the performance of the one-hinge swimmer.

- **Chapter 6 :-** “*Swimming of a 3-D elastic scallop in a viscous fluid*”. In this chapter, we will report the dynamics of a three dimensional version of the flexible swimmer. Here, we will consider a finite width of the flaps of the swimmer and show how this width affects the motion of the swimmer.
- **Chapter 7 :-** “*Swimming of a waving sheet in a viscous fluid*”. In this chapter, we will consider a well known Taylor sheet model in three dimensions. For infinite long two dimensional Taylor sheet the ratio of the parallel and perpendicular component of the friction coefficient is a constant (2). But when we will consider a finite sheet in three dimensions, the ratio will no longer remain a constant and depends on the length and width of the sheet. In this chapter, we will show how the width and the length of the sheet will affect the dynamics of the swimmer. We will also study the stroke efficiency of the swimmer by varying the length and width of the swimmer.
- **Chapter 8 :-** “*Conclusions and future scope of the work*”. In this chapter, we will briefly conclude our results which are followed by the future scope of this work.

Chapter 2

Literature review

2.1 Fluid dynamics

In this thesis, we investigate the dynamics of the artificial swimmers and the surrounding fluid medium using the computer simulations. The fundamental knowledge of the fluid dynamics is required to build and control the artificial swimmers and to understand the involved physical phenomena. Also, the understanding of the basic Physics of fluid flow will allow us to precisely understand the obtained results. In this section we provide an essential knowledge of the fluid dynamics for the present thesis.

2.1.1 Fluid properties

A fluid is defined as a substance that deforms in a continuous manner on the application of a shear stress. The fluids exhibit several properties like,

Viscosity

Viscosity is the property of the fluid which provides resistance to the shear stresses. To explain this property better, we consider a fluid between two long horizontal parallel planes. Let's consider the distance between the planes is H as illustrated in figure 2.1. To provide a motion to the upper plane, we apply a tangential force \mathbf{F} which offers a constant velocity \mathbf{V} to the plane in the x-direction. Now, we analyze the velocity profile of the fluid flow between the planes. In the figure 2.1, we can see that the velocity of the fluid layer adjacent to the stationary lower plane is zero and adjacent to the upper plane it

is \mathbf{V} , which is equal to the upper plane velocity. Experimental observations show that the viscous fluid takes the tangential velocity of the adjacent boundaries also known as **no-slip condition**. Also the layer adjacent to the boundary imposes tangential forces to the next adjacent layer and so on. Because of this we get a linear velocity profile (when H is small), as can be seen in figure 2.1.

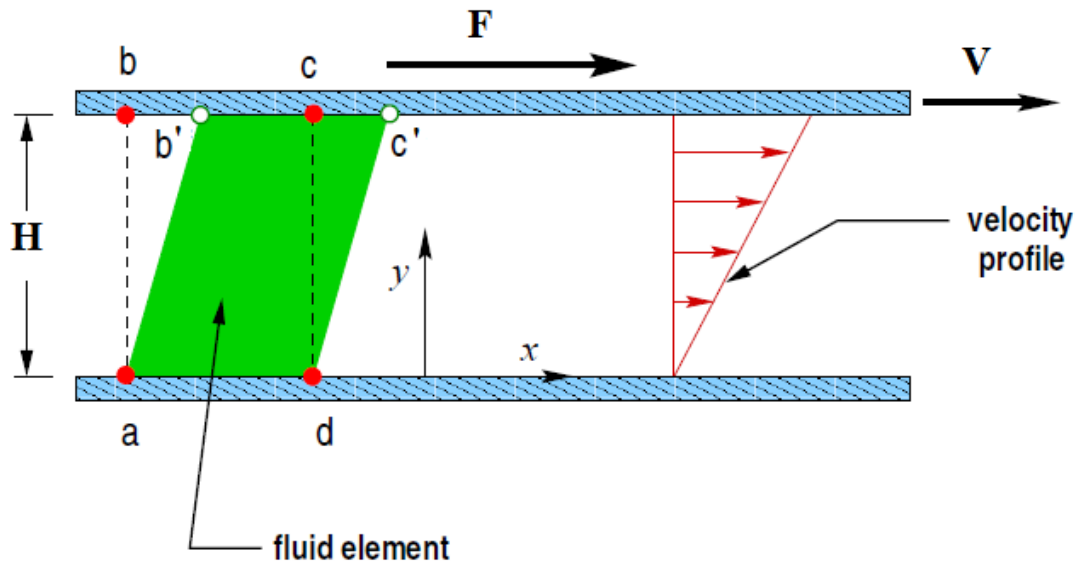


Fig. 2.1 Flow profile between two parallel planes (image source [12]).

According to the experiments, to provide a constant velocity \mathbf{V} to the upper plane if a force \mathbf{F} is required, then \mathbf{F} is proportional to the velocity \mathbf{V} , $1/H$ and the area of plane A . So,

$$\mathbf{F} = \eta \frac{A\mathbf{V}}{H} \quad (2.1)$$

where η is proportionality constant. We know that the shear stress can be written as $\bar{\tau} = \mathbf{F}/A$. So we can rewrite the equation 2.1 as $\bar{\tau} = \eta \frac{\mathbf{V}}{H}$ and more appropriately

$$\tau = \eta \frac{dv_x}{dy}. \quad (2.2)$$

According to **Newton's Law of Viscosity**, in fluids for an applied strain rate, the shear stress is directly proportional to the viscosity. In equation 2.2, if η denotes the viscosity, then the equation is a mathematical expression of Newton's law of viscosity. The fluids that follow the expression 2.2 are known as **Newtonian fluid**. But, all the

fluids do not follow Newton's law of viscosity. For example: blood, polymers, paints, ketchup, etc. and these fluids known as **non-Newtonian fluids**.

Momentum diffusion

To understand the physical description of momentum diffusion, consider a fluid between two parallel planes as shown in figure 2.2. Suppose at time $t = 0$ both the planes are stationary. So the fluid is also at rest between the planes. An instant later, apply a tangential force \mathbf{F} to the upper plane due to which it attain a velocity \mathbf{V} . At this moment the velocity profile appears as shown in figure 2.2(a). The layer of the fluid that is just adjacent to the upper plane moves with the velocity of the plane due to the no-slip boundary condition, but the remaining fluid layers seem almost stationary. The top layer of fluid having velocity \mathbf{V} interacts with the next adjacent layer and exchanges velocity or momentum with it. Thus, after a few moments, the velocity profile might look as shown in figure 2.2(b). We can observe that high momentum fluid particles have diffused away from the moving plane towards the interior of the fluid region. In figure 2.2(c), we can see that at a later time fluid tries to attain a smooth linear velocity profile. When the fluid acquires its steady behavior, then the absolute linear velocity profile can be seen. From the figure 2.2 it is clear that diffusion of momentum occurs from regions of higher momentum to those of low momentum regions.

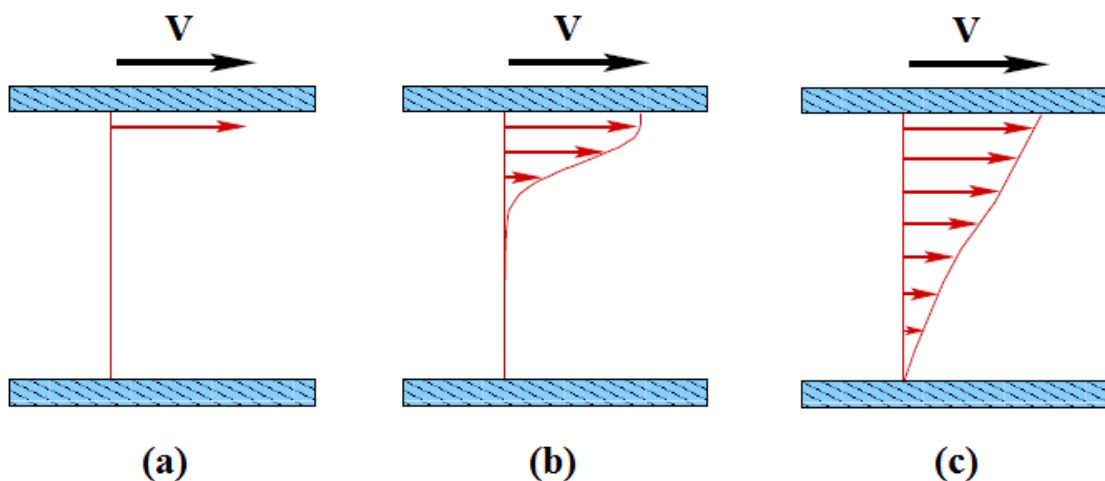


Fig. 2.2 Momentum diffusion of fluid particles between two parallel planes. One of the plane is stationary and the other one is moving at velocity \mathbf{V} (image source [12]).

2.1.2 Continuum hypothesis

The continuum hypothesis says that when dealing with fluids one can ignore the fact that fluids are actually made up of billions of individual particles in a rather small region, and instead can treat that the properties of fluids are varying continuously from one point to the next point within the fluid. To understand the importance of the continuum hypothesis, let us consider a small volume of fluid where particles are moving randomly. The diameter of this volume is smaller as compared to the average distance traveled by particles between successive collisions and as a result it contains only a few particles which are well separated. Now we want to calculate the velocity at a particular point in this volume without considering the continuum hypothesis. We will be able to calculate the velocity of the fluid at the desired point if there is a particle situated at the desired location. If there is no particle situated at the desired point and nearest particles are moving in different directions. Then, we will not be able to calculate the velocity at the desired point, but we can take the average over the velocities of all the surrounding particles to get the estimate of the velocity at the required point. Though, this will not provide significant results because according to the statistical mechanics the sample should be large enough for error less measurements. But, if we take an average over a comparatively large region (larger than the mean free path), we can find out the value of velocity at selected point. Further, if we slide the averaging volume throughout the fluid in a continuous manner, thus can obtain a continuous function defined at each point for the velocity to be treated in more detail in the sequel. Basically, the continuum hypothesis allows the identification of each fluid particle and then consideration of the volume of fluid as a whole to be a continual aggregation of these fluid particles. Thus, the continuum hypothesis is important to provide the framework for the analyses of fluids.

2.1.3 Continuity equation

The continuity equation is a partial differential equation which represents conservation of mass in a fluid flow. To derive the continuity equation, we consider an arbitrary region $\Omega(t)$ which contains fluid (or fluid element) with fixed mass m . The mass m of the fluid element can be written in the form of density as

$$m = \int_{\Omega(t)} \rho d\Omega = \text{constant}. \quad (2.3)$$

Both $\Omega(t)$ and ρ can change with time, but they should change in a manner that m remains constant to maintain the conservation of mass. We can understand this by an example of a balloon filled with hot gas surrounded by cooler environment. The temperature of the gas filled inside the balloon will decrease due to the heat transformation with the surrounding environment. As a result the density of the gas will increase and the size of the balloon will decrease, but the mass of the gas will remain unchanged.

Mathematically, this can be written as

$$\frac{d}{dt} \int_{\Omega(t)} \rho d\Omega = 0. \quad (2.4)$$

By using the general transport theorem and Gauss divergence theorem, we can write the equation 2.4 as

$$\int_{\Omega(t)} \left(\frac{\partial \rho}{\partial t} + \nabla \cdot \rho \mathbf{V} \right) d\Omega = 0. \quad (2.5)$$

The algorithm 2.5 is known as continuity equation and it can also be written in a differential form as

$$\frac{\partial \rho}{\partial t} + \nabla \cdot \rho \mathbf{V} = 0. \quad (2.6)$$

In the case of constant density, $\frac{\partial \rho}{\partial t} = 0$, the equation 2.6 reduces to

$$\nabla \cdot \mathbf{V} = 0. \quad (2.7)$$

The equation 2.7 is the continuity equation for in-compressible fluids.

2.1.4 Navier-Stokes equations

The Navier-Stokes equations are the equations of motion of fluid flow. In the present thesis, we deal with in-compressible fluid. So we will go into the details of the Navier-Stokes equations for in-compressible fluids. For fluids we can express the Newton's

second law of motion in words as

$$\left(\begin{array}{c} \text{rate of change of momentum of a fluid} \\ \text{element with respect to time} \end{array} \right) = \left(\begin{array}{c} \text{sum of the forces acting on} \\ \text{the fluid element} \end{array} \right). \quad (2.8)$$

To calculate the L.H.S. of equation 2.8, we can write it as [12]

$$\left(\begin{array}{c} \text{rate of change of momentum} \\ \text{with time} \end{array} \right) \equiv \frac{D}{Dt} \int_{\Omega(t)} \rho \mathbf{V} d\Omega. \quad (2.9)$$

For in-compressible fluids density is constant and $\nabla \cdot \mathbf{V} = 0$, so the expression of rate change of momentum can be simplified further as

$$\frac{D}{Dt} \int_{\Omega(t)} \rho \mathbf{V} d\Omega = \int_{\Omega(t)} \rho \frac{D\mathbf{V}}{Dt} d\Omega \quad (2.10)$$

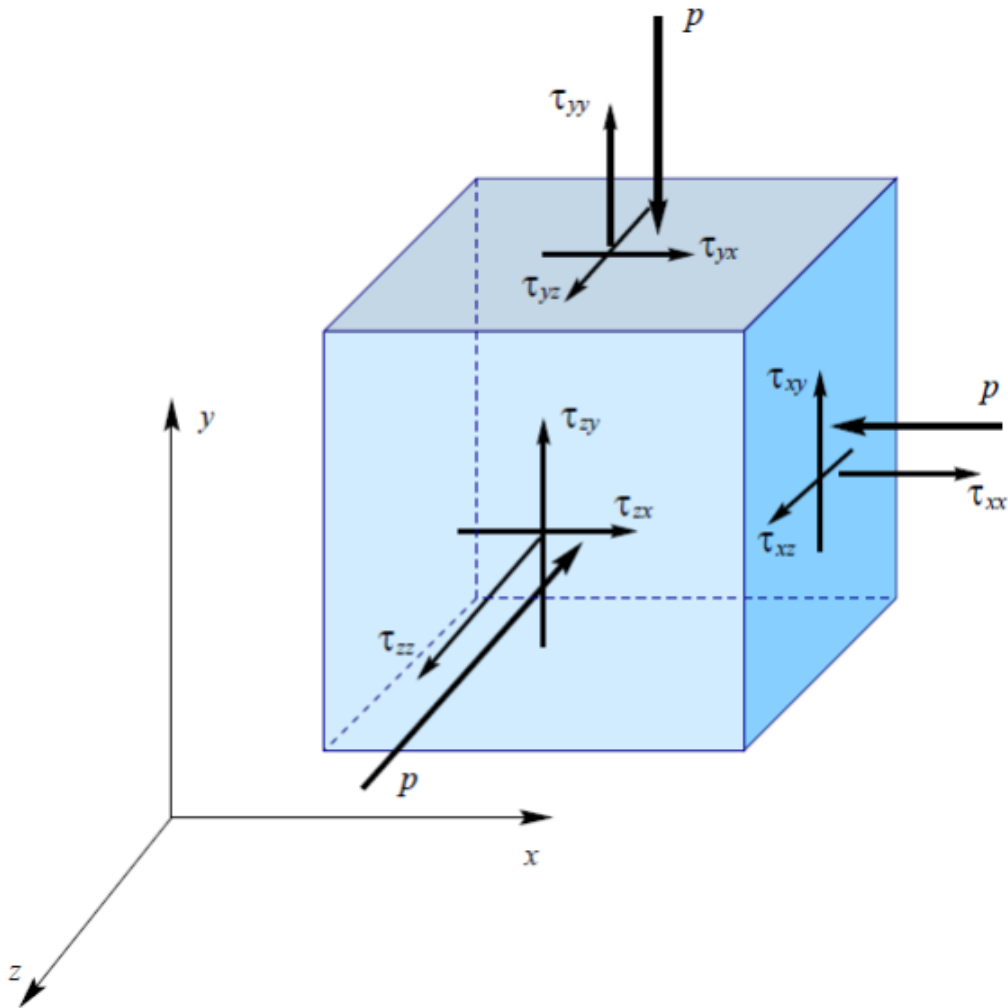


Fig. 2.3 Representation of viscous stresses and pressure that are acted on a fluid element (image source [12]).

Further, we consider R.H.S. of the equation 2.8 that is the summation of the forces acting on the fluid element. There are mainly two types of the forces, one is body forces and another is surface forces. The body forces acting on the region $\Omega(t)$ can be denoted as

$$\int_{\Omega(t)} \mathbf{F}_B d\Omega. \quad (2.11)$$

Generally the body forces include buoyancy force, electromagnetic force and rotational effect. The surface forces acting on the surface $S(t)$ of $\Omega(t)$ can be written as

$$\int_{S(t)} \mathbf{F}_S dS. \quad (2.12)$$

The sum of the forces acting on the fluid element contains a volume integral as well as a surface integral which is not easy for analytical calculations. The surface force \mathbf{F}_S is a vector quantity and can be written in a matrix form as $\mathbf{F}_S = \mathbf{T} \cdot \hat{n}$, where \hat{n} is the unit vector in the outward direction normal to the surface $S(t)$. \mathbf{T} is a 3×3 matrix which contains nine elements. These elements contain the same information found in the components of \mathbf{F}_S . Using Gauss's theorem and equations 2.8 - 2.12, we can find the preliminary version of the Navier-Stokes equation as follows

$$\int_{\Omega(t)} \rho \frac{D\mathbf{V}}{Dt} d\Omega = \int_{\Omega(t)} \mathbf{F}_B d\Omega + \int_{\Omega(t)} \nabla \cdot \mathbf{T} d\Omega, \quad (2.13a)$$

$$\rho \frac{D\mathbf{V}}{Dt} = \mathbf{F}_B + \nabla \cdot \mathbf{T}. \quad (2.13b)$$

The elements of \mathbf{T} are associated with the shear stress and pressure as depicted in figure 2.3. In figure 2.3, the first subscript of τ denotes the face of the cube on which the stress is acting and the second subscript of τ indicates the direction of the stress. For example, in τ_{xy} the subscript x represents that the considered component act on a face normal to the x axis, and the subscript y denotes that the stress is acting in the y direction. It can be easily calculated that the various components of the shear stress shown in figure 2.3 are associated as

$$\tau_{xy} = \tau_{yx}, \quad \tau_{yz} = \tau_{zy}, \quad \tau_{xz} = \tau_{zx} \quad (2.14)$$

From equation 2.14 and Newton's law of viscosity (equation 2.2), we can find that

$$\tau_{xy} = \eta \left(\frac{\partial v_x}{\partial y} + \frac{\partial v_y}{\partial x} \right) = \tau_{yx}, \quad (2.15a)$$

$$\tau_{yz} = \eta \left(\frac{\partial v_y}{\partial z} + \frac{\partial v_z}{\partial y} \right) = \tau_{zy}, \quad (2.15b)$$

$$\tau_{xz} = \eta \left(\frac{\partial v_x}{\partial z} + \frac{\partial v_z}{\partial x} \right) = \tau_{zx}. \quad (2.15c)$$

The pressure is a scalar quantity, and in the present case the forces associated with it are compressive as can be seen in figure 2.3. So we use a minus sign in the pressure terms. The matrix \mathbf{T} contains the viscous stresses as well as pressure contribution, and can be expressed as

$$\mathbf{T} = -p \begin{bmatrix} 1 & 0 & 0 \\ 0 & 1 & 0 \\ 0 & 0 & 1 \end{bmatrix} + \begin{bmatrix} \tau_{xx} & \tau_{xy} & \tau_{xz} \\ \tau_{xy} & \tau_{yy} & \tau_{yz} \\ \tau_{xz} & \tau_{yz} & \tau_{zz} \end{bmatrix}. \quad (2.16)$$

Now if we substitute this into equation 2.13b, it gives

$$\rho \frac{Dv_x}{dt} = -\frac{\partial p}{\partial x} + \frac{\partial \tau_{xx}}{\partial x} + \frac{\partial \tau_{yx}}{\partial y} + \frac{\partial \tau_{zx}}{\partial z} + F_{B_x}, \quad (2.17a)$$

$$\rho \frac{Dv_y}{dt} = -\frac{\partial p}{\partial y} + \frac{\partial \tau_{xy}}{\partial x} + \frac{\partial \tau_{yy}}{\partial y} + \frac{\partial \tau_{zy}}{\partial z} + F_{B_y}, \quad (2.17b)$$

$$\rho \frac{Dv_z}{dt} = -\frac{\partial p}{\partial z} + \frac{\partial \tau_{xz}}{\partial x} + \frac{\partial \tau_{yz}}{\partial y} + \frac{\partial \tau_{zz}}{\partial z} + F_{B_z}. \quad (2.17c)$$

Now if we employ equation ??, 2.7, and 2.15 into equation 2.17, it can be written as

$$\underbrace{\frac{\partial \mathbf{V}}{\partial t}}_{\text{local accel.}} + \underbrace{\mathbf{V} \cdot \nabla \mathbf{V}}_{\text{convective accel.}} = \underbrace{-\frac{\nabla p}{\rho}}_{\text{pressure forces}} + \underbrace{\mu \nabla^2 \mathbf{V}}_{\text{viscous forces}} + \underbrace{\frac{\mathbf{F}_B}{\rho}}_{\text{body forces}}, \quad (2.18)$$

the general representation of Navier-Stokes equations for in-compressible fluids, where μ is the kinematic viscosity and ∇^2 is Laplace operator.

2.2 Life around scallop theorem

The Navier-Stokes equation

$$\rho \left(\frac{\partial \mathbf{V}}{\partial t} + \mathbf{V} \cdot \nabla \mathbf{V} \right) = -\nabla p + \eta \nabla^2 \mathbf{V} + \mathbf{F}_B, \quad (2.19)$$

describe the motion of an in-compressible Newtonian fluid. When we are considering the case of micro-swimmers, $Re \ll 1$ as discussed in section 1.1. At low Reynolds number regime, we can neglect the inertia and equation 2.19 can be reduced as

$$-\nabla p + \eta \nabla^2 \mathbf{V} = 0. \quad (2.20)$$

This equation is called as **Stokes equation** and tells that in inertialess world, when there are no external forces the pressure forces have to balance the viscous forces. As the fluid is in-compressible, then according to conservation of mass, flow field should also be divergence free ($\nabla \cdot \mathbf{V} = 0$) as discussed before. At Stokes regime, the pressure forces have a linear relation with velocity which means in this regime the flow field is kinematically reversible [59–61]. The effect of kinematic reversibility is well explained by E. M. Purcell in “Life at Low Reynolds Number” using an example of micro scallop [10]. In figure 2.4, we have illustrated the motion of a scallop at low Reynolds number. Initially the shells of the scallop are opened as shown in 2.4(a). When the scallop closes its shells, it produces a velocity field \mathbf{V} which induces viscous stresses. According to the Stokes equation 2.20, these viscous stresses should be balanced by pressure. This balancing pressure further induces a force on the scallop, due to which scallop travels a dx distance in the backward direction as depicted in figure 2.4(a) and reaches at a state shown in figure 2.4(b). After this the scallop again open up its shells. Since the fluid is kinematic reversible, a reverse motion of the shells will produce an equal & opposite velocity field $-\mathbf{V}$. Because the pressure has a linear relationship with velocity, so the opening of the shells will produce a force which is equal and opposite to the force that was produced at the time of closing the shells. Due to this force the scallop will travel a $-dx$ distance and reaches at a state shown in 2.4(c). Finally, over a complete cycle of motion, the scallop will reach at the same point from where it started. This is because for a complete cycle there is no net force and hence no net displacement. This result is not

only for the scallop, but is also applicable for all the low Reynolds number swimmers which deform their body in a sequence and go back to the original shape by using the reverse sequence. This type of motion is known as reciprocal motion (explained before in section 1.1.2). This phenomenon is called as a “Scallop Theorem” and a swimmer have to break this for self propulsion.

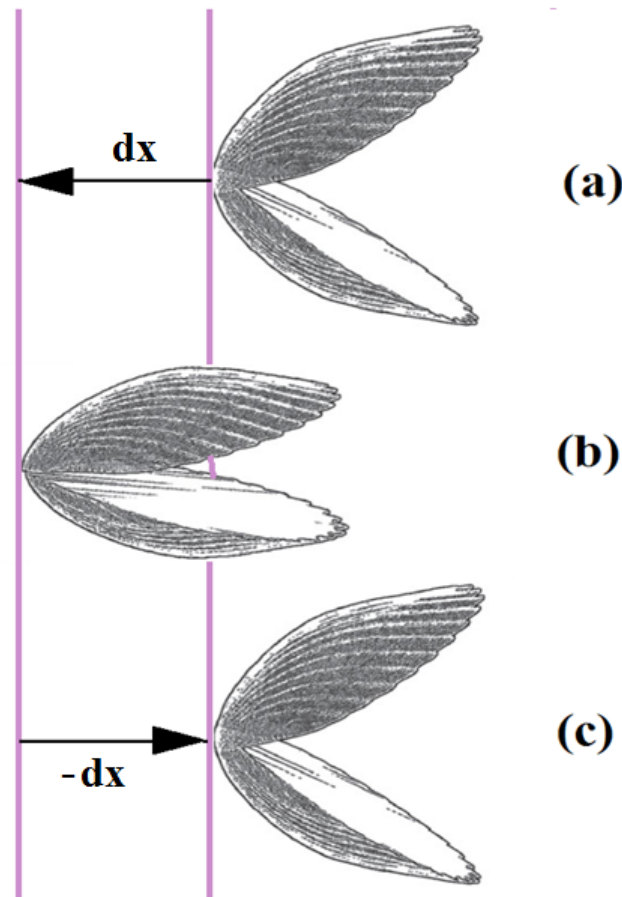


Fig. 2.4 Motion of the scallop at low Reynolds number.

Over the time many theoretical model swimmers have been proposed that successfully break the Scallop theorem. For example; “spherical squirmer” was proposed by M. J. Lighthill, where he showed that the squirming motion of nearly spherical deformable bodies is able to propel at low Reynolds number regime [62]. Sir Taylor Groffrey proposed a “waving sheet model”, where the deformation of the sheet due to propagating wave enables it to propel at low Reynolds number [63]. A simple “three sphere swimmer” was proposed by A. Najafi and R. Golestanian, where the spheres are connected by two slender rods and these rods change their length in nonreciprocal fashion similar to Purcell’s two-hinge swimmer and break the time inversion symmetry [64]. J. E. Avron et

al. proposed “Pushmepullyou swimmer”, where two spheres which exchange volume are connected by a thin rod whose length also can be varied [65]. Here, due to the two degrees of freedom, i.e. the volume of the sphere and the length of the rod, the swimmer can perform nonreciprocal motion. Few other similar examples are “orientation changing two spheres swimmer” [66], “three sphere swimmer with one passive elastic arm” [67], “elastic two sphere swimmer” [68], etc.

2.3 Flagellar swimming

2.3.1 Taylor sheet

In 1951, Sir Geoffrey Taylor showed how the micro-swimmers propel themselves in a viscous fluid medium without inertia [63]. For this, he considered an infinite waving sheet surrounded by a viscous fluid and calculated the flow field generated by the propagating transverse wave. The sheet is similar to the waving flagellum of the sperm cell. The Taylor considered a two-dimensional flow which made the problem easier to handle. The vertical displacement of the sheet is denoted as

$$y_0 = b \sin(kx - wt), \quad (2.21)$$

where k is the wave number, b is the amplitude of the wave, w is the beating frequency and $+x$ is the direction of the wave propagation. The amplitude of wave b is considered small as compared to the wavelength $2\pi/k$ which further simplifies the problem. To calculate the flow field generated by the propagating wave (through sheet), the Stokes equations have to be solved with no-slip boundary conditions,

$$\frac{\partial y_0}{\partial t} = -b w \cos(kx - wt), \quad (2.22)$$

with a flow field far from the sheet

$$\lim_{y \rightarrow \infty} u(x, y) = -\mathbf{V}. \quad (2.23)$$

Here, $-\mathbf{V}$ is the velocity of the sheet, which is opposite to the velocity of wave propagation.

Though \mathbf{V} is unknown, but Taylor obtained that not any extra condition is needed to calculate \mathbf{V} , and there is a unique value of \mathbf{V} consistent with the solution to the Stokes equation and the no-slip boundary conditions 2.22. Though the Stokes equations are linear, but the propulsion velocity \mathbf{V} is not a linear function of b . Due to the symmetry, the propulsion velocity must be invariant under the changing sign of amplitude from b to $-b$ which is equivalent to a phase change of π , indicating that the \mathbf{V} should be an even function of amplitude b . Taylor expanded the boundary condition (equation 2.22) in bk and solved the Stokes equation order by order. Here we will only take the leading term that is quadratic in b . The velocity \mathbf{V} is a vector, so it should be proportional to a vector quantity in the problem i.e. the wave vector $\mathbf{k} = k\hat{x}$. The dimensional analysis tells that the dependency of \mathbf{V} on the other parameters of the problem is $\mathbf{V} \propto w\mathbf{k}b^2$. Taylor calculated the constant of proportionality as

$$\mathbf{V} \sim \frac{1}{2}w\mathbf{k}b^2. \quad (2.24)$$

The dimensional consideration needs that the propulsion velocity should not be dependent on viscosity. So this result holds when there is no load attached to the waving sheet.

2.3.2 Slender-body hydrodynamics

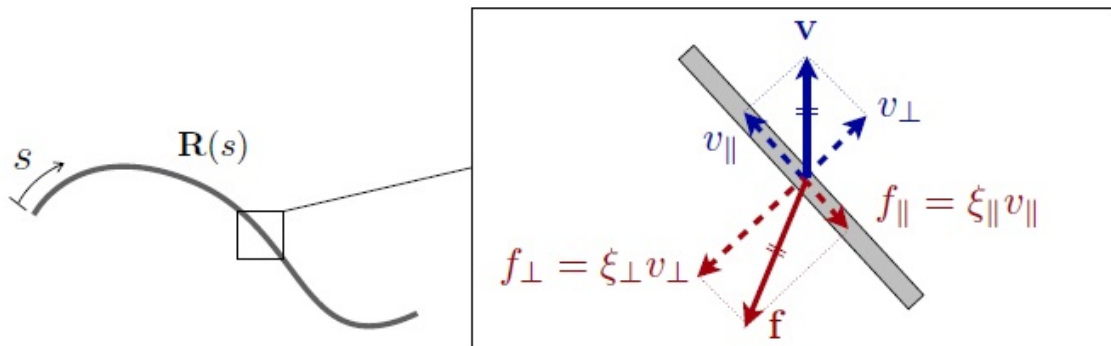


Fig. 2.5 Resistive force theory relates the local viscous force to the local velocity in terms of the resistive or drag coefficients (image source [13]).

Taylor's infinite waving sheet model provided an understanding of the flagellar swimming. Although, the real biological flagellum is a slender filament with a finite amplitude.

These aspects can be covered by using a slender-body theory for Stokes flows [69–74]. This method is appropriate for slender filaments, typically to the aspect ratio of one to a few hundreds. The idea of this theory is to model the flow field generated by an undulating filament by replacing the filament with a line of singular solutions to Stokes flow of appropriate strength. This theory provides a relation between the force acting on the filament to its distribution of velocity relative to the background fluid. The leading order result of slender-body theory is a local-theory which states that the viscous forces acting on the body at a point are linearly proportional to the local velocity of the filament. This local drag theory neglects the hydrodynamic interactions between separated parts of the filament and is known as resistive force theory [14, 75, 76].

The local velocity \mathbf{v} of the filament relative to the fluid can be broken into two components, parallel (v_{\parallel}) and perpendicular (v_{\perp}) to the local filament axis as shown in figure 2.5. Resistive force theory says that the drag force is an-isotropic with parallel and perpendicular drag coefficients to the local filament axis. The local force per unit length can be expressed as

$$f_{\parallel} = -\xi_{\parallel} v_{\parallel} \quad (2.25a)$$

$$f_{\perp} = -\xi_{\perp} v_{\perp}. \quad (2.25b)$$

The drag coefficients ξ_{\parallel} and ξ_{\perp} can be approximately given by

$$\xi_{\parallel} \approx \frac{2\pi\eta}{\ln(L/r) - 1/2} \quad (2.26a)$$

$$\xi_{\perp} \approx \frac{4\pi\eta}{\ln(L/r) + 1/2}, \quad (2.26b)$$

where L is the length of the filament and r is the radius of the filament. The expression 2.26 is valid when $L \gg r$, as $\frac{L}{r} \rightarrow \infty$, the ratio $\frac{\xi_{\perp}}{\xi_{\parallel}} \rightarrow 2$. The viscous force acting on the per unit length of the filament can be written in a combined form as

$$\mathbf{f}_v = -(\xi_{\perp} \hat{\mathbf{n}}\hat{\mathbf{n}} + \xi_{\parallel} \hat{\mathbf{t}}\hat{\mathbf{t}}) \cdot \mathbf{v}, \quad (2.27)$$

where $\hat{\mathbf{t}}$ is a local unit tangent vector, $\hat{\mathbf{n}}$ is a local unit normal vector along the filament and \mathbf{v} is the local velocity along the filament relative to flow.

Gray and Hancock [75] used resistive force theory to the motion of sea-urchin sperm and found appreciable agreement with the experimental observations. They determined the leading order propulsion velocity as

$$V = \frac{b^2 w k}{2} \left(\frac{\xi_{\perp}}{\xi_{\parallel}} - 1 \right) \left(\frac{1}{1 + \frac{R_h}{N \lambda \xi_{\parallel}}} \right), \quad (2.28)$$

where N is the number of wave trains in flagella and R_h is the drag coefficient of the passive head. The speed of the swimmer decreases monotonically as the size of head increases. Let us suppose that the length of the filament tends to infinity. That means the ratio $\frac{\xi_{\perp}}{\xi_{\parallel}} \rightarrow 2$ and also there is no head attached with filament ($R_h = 0$), then the swimming speed reduces to $V \sim \frac{1}{2} w k b^2$ which is identical to that derived by Taylor for a waving sheet. According to the equation 2.28, when drag is isotropic ($\xi_{\perp} = \xi_{\parallel}$), then the speed goes to zero, and that tells the importance of the drag anisotropy.

2.3.3 Theory of the flexible filament

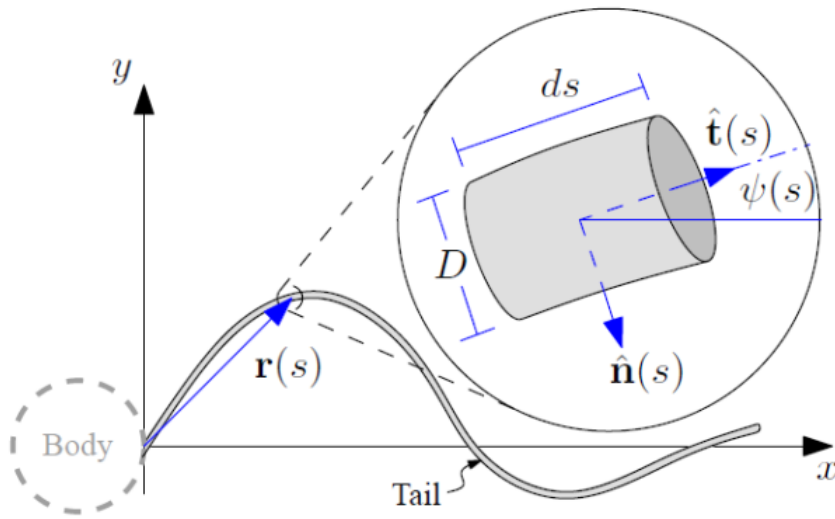


Fig. 2.6 Flexible filament, where base of the filament is situated at the origin. The shape of the filament is given by the position vector $\mathbf{r}(s)$. Inset shows ds length element of the filament and local angle ψ (image source [14]).

Now we will see how flexibility affects the motion in Stokes regime. In figure 2.6, a flexible filament has been shown. The shape of the filament is described by the position vector $\mathbf{r}(s)$, where s is arc length coordinate, $\hat{\mathbf{n}}$ is a local unit normal vector, $\hat{\mathbf{t}}$ is a local unit tangent vector and ψ is a local angle. The elastic forces on the filament can be obtained

from an energy functional which considers the bending energy & the inextensibility constraint

$$\varepsilon = \int_0^L \left(\frac{A}{2} \kappa^2 + \frac{\sigma}{2} \mathbf{r}_s^2 \right) ds, \quad (2.29)$$

here the subscript s notifies a derivative (e.g. $\mathbf{r}_s = \frac{\partial \mathbf{r}}{\partial s}$), $\kappa \equiv \psi_s$ is the curvature of the filament, A is the bending rigidity and σ is the Lagrange multiplier enforcing inextensibility. By taking variational derivative ($\frac{\delta \varepsilon}{\delta \mathbf{r}}$), we can find the elastic force per unit length as [77, 78]

$$\mathbf{f}_\varepsilon = -(A\psi_{sss} - \psi_s \tau) \hat{\mathbf{n}} + (A\psi_{ss} \psi_s - \tau_s) \hat{\mathbf{t}}, \quad (2.30)$$

where $\tau = -\sigma + A\kappa^2$ is local tension in the filament, $\mathbf{r}_s = \hat{\mathbf{t}}$, $\hat{\mathbf{n}}_s = -\kappa \hat{\mathbf{t}}$ and $\hat{\mathbf{t}}_s = \kappa \hat{\mathbf{n}} = \mathbf{r}_{ss}$.

Since we are working at a regime where inertial forces are negligible. So the local viscous forces per unit length \mathbf{f}_v (equation 2.27) balance the local elastic forces per unit length \mathbf{f}_ε (equation 2.30),

$$\mathbf{f}_v + \mathbf{f}_\varepsilon = 0. \quad (2.31)$$

By substituting the equation 2.27 & 2.30 in above, we get

$$\psi_t = -\frac{1}{\xi_\perp} (A\psi_{ssss} - \tau\psi_{ss} - \tau_s\psi_s) + \frac{1}{\xi_\parallel} (A\psi_s^2\psi_{ss} + \tau_s\psi_s), \quad (2.32a)$$

$$\tau_{ss} - B\tau\psi_s^2 = -A(1+B)(\psi_s\psi_{sss}) - A\psi_{ss}^2, \quad (2.32b)$$

where $B = \xi_\parallel/\xi_\perp$. We can simplify the above equation if we consider that the slope of the filament is small ($\psi \approx y_x \ll 1$). Wiggins & Goldstein [79] have shown that, this consideration gives a linear hyperdiffusion equation

$$y_t \approx -\frac{A}{\xi_\perp} y_{xxxx} \quad (2.33)$$

We now non-dimensionalize the equation 2.33 to get the relevant dimensionless parameters. In case of harmonic angular actuation, we use $\psi = a \sin(\omega t)$ boundary condition at the base. We substitute $x = L\tilde{x}$, $y = aL\tilde{y}$, $t = \tilde{t}/\omega$ in the equation 2.33 as

$$\begin{aligned}\tilde{y}_t &= -\frac{A}{w\xi_\perp} \frac{1}{L^4} \tilde{y}_{\tilde{x}\tilde{x}\tilde{x}\tilde{x}} \\ &= -\left(\frac{\ell_w}{L}\right)^4 \tilde{y}_{\tilde{x}\tilde{x}\tilde{x}\tilde{x}}.\end{aligned}$$

Where $\ell_w = \left(\frac{A}{w\xi_\perp}\right)^4$ is the elasto-hydrodynamic penetration length. The shape of the filament is a function of the angular amplitude a and the dimensionless number known as Sperm number,

$$S_p = \frac{L}{\ell_w} = L \left(\frac{w\xi_\perp}{A}\right)^{\frac{1}{4}}. \quad (2.34)$$

This dimensionless Sperm number is the key parameter which tells the flexibility of the filament as well as the efficiency of the swimmer. The optimum flexibility of the filament allows the propagation of waves through filament which breaks the kinematic reversibility and therefore allows it to move in low Reynolds number regime [14, 19, 79–81]. This theory predicts the optimum values of parameters, which results the maximum propulsive forces to the swimmer. The large value of Sperm number represents the dominance of elastic forces, which provides stiff filament that obey Scallop theorem, and very small value of S_p predicts dominance of viscous forces. Wiggins & Goldstein [79] provided the shape prediction using the Sperm number in their studies, which was comparable with experimental studies [82]. The figure 2.7 shows how the shape of the filament changes with Sperm number. The elasto-hydrodynamic theory considers small amplitude approximations. Still it works fine for comparatively large amplitudes. C. P. Lowe et al. used simulation approach for the analysis of single filament or one-arm swimmer, where they confirmed the theoretical prediction and showed that small amplitude approximation also works for large amplitudes as well [83, 84].

2.4 A brief literature review

From past few decades people have shown immense interest in the locomotion of flexible filaments [77–80, 83–87] and by exploiting flexibility they have proposed many theoretical swimmers [19, 68, 67] as well as have realized it experimentally [14, 15, 17, 53, 55]. In 2005 Dreyfus et al. constructed the first man made artificial micro swimmer, where

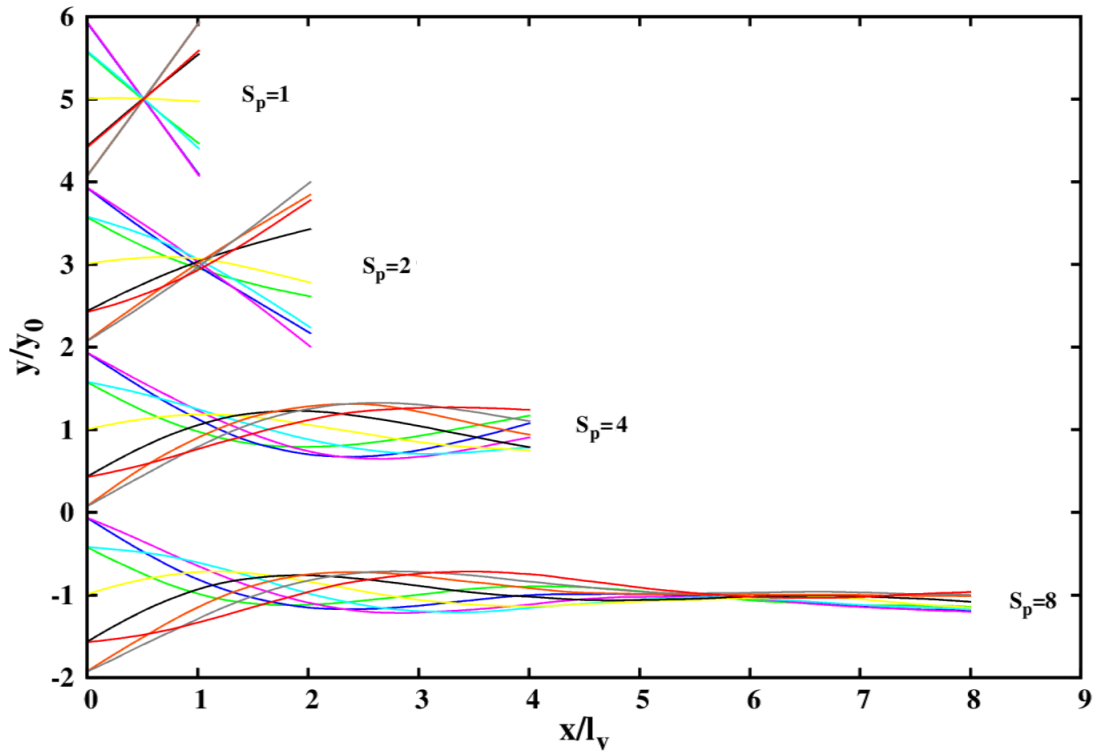


Fig. 2.7 Deformation of a single filament as the value of Sperm number changes, obtained from our simulations.

they considered a chain of para-magnetic colloidal particles linked by DNA as shown in figure 2.8. In their experiment they had shown that an applied magnetic field induces beating pattern in the flexible filament and the swimmer is able to exhibit non-reciprocal motion. This magnetic flexible chain is connected to a red blood cell, in the absence of the red blood cell as a head swimmer is not able to perform non-reciprocal motion. The induced bending wave travels from tip to head and as a result swimmer propel from head to tip. They expressed the maximum scaled velocity as a function of the dimensionless sperm number S_p , as predicted in the case of model elastic filaments [79]. However, they showed that the optimum combination of parameters also depends upon a distinct parameter named as magnetoelastic number, which involves the magnetic field strength. The velocity and the direction of motion of the swimmer can be controlled by adjusting the magnetic field. Based on this artificial swimmer further experimental [14, 88, 89], theoretical [19] and computational [11] studies have been done. In 2010, Wei Gao et al. achieved a magnetically actuated nanowire swimmer with a gold head and nickel tail jointed by a flexible silver bridge [16], schematic is shown in figure 2.9. The flexible silver bridge allows the cyclic deformation under an external rotating magnetic field. Under

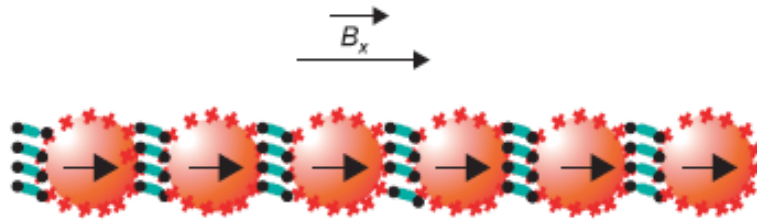


Fig. 2.8 Schematic representation of a flexible magnetic filament, proposed by Dreyfus et al [15].

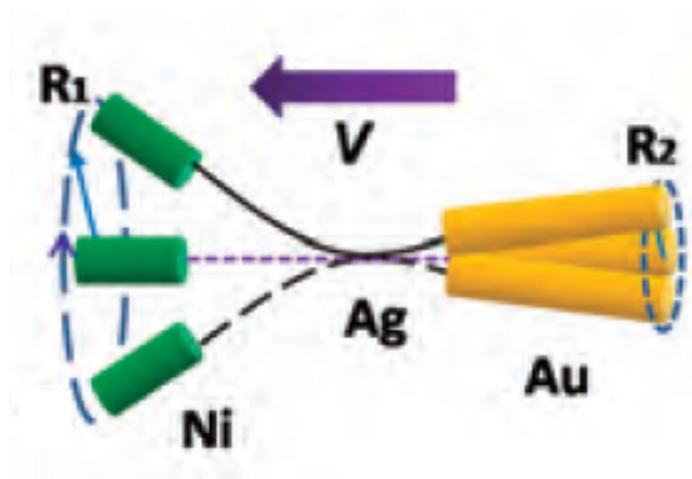


Fig. 2.9 Schematic of the nano-wire magnetic swimmer, proposed by Wei Gao et al [16].

rotating magnetic field the nickel tail starts to rotate, which results the rotation of the gold head segment at a different amplitude, hence breaks the system symmetry and induces the propulsion. The forward and backward propulsion are achieved by tailoring the length of the nickel and gold segments. A precise On/Off motion control is achieved by modulating the magnetic field. The flexible nanowire swimmer shows defined locomotion over a long path, parallel to the magnetic field axis. The length and the speed of this swimmer are around $6\mu m$ and $3\mu m/s$ respectively, that means it moves approximately 0.5 body length per second. Very recently Tianlong Li et al. have created a magnetically driven fish-like nano-swimmer which exhibit a very efficient swimming. The nano fish contains 2 nickel segments as a body, 1 gold segment as a head and 1 gold segment as the caudal fin, with three flexible silver hinges linking each segment. Due to an oscillating magnetic field, the nickel segments bend the body and caudal fin periodically generate travelling-wave motion. This nano fish has a diameter 200 nm , length $4.8\ \mu m$ and it swims at a speed $30\ \mu m s^{-1}$.

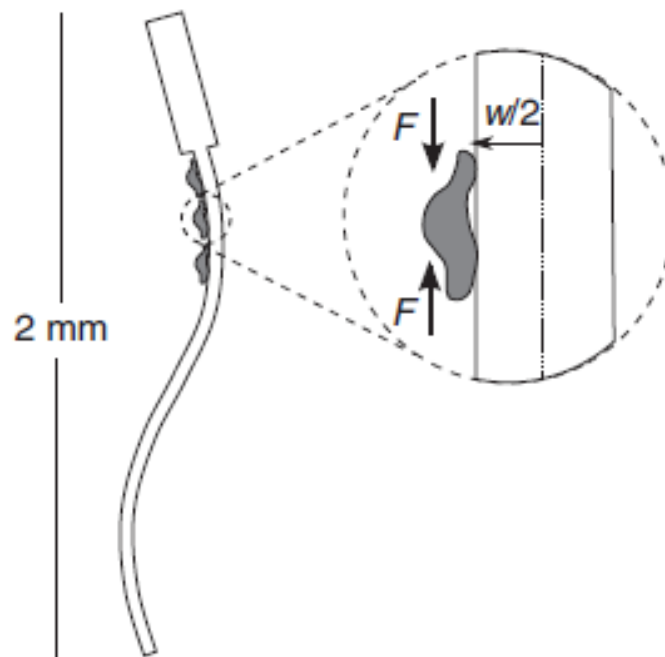


Fig. 2.10 Schematic of a biohybrid swimmer actuated by heart muscles, proposed by B. J. Williams et al [17].

Most of these proposed artificial swimmers that work on the concept of flexible oar motion are driven by external magnetic field and contain a head and a single tail. Now a days people have been working on different ideas to construct and operate these structures. Some of the interesting ideas are employing heart muscles to actuate the structure [17] and also use of remote light signals to control the swimmer [18]. B. J. Williams et al. proposed a bio-hybrid synthetic swimmer actuated by the heart muscles as depicted in figure 2.10 [17]. The swimmer made up of a polydimethylsiloxane filament with a short rigid head and a long slender flexible tail. They selectively seeded the heart muscles at the joint area of the head & tail. The contraction-relaxation of heart muscles deform the filament, which breaks the time inversion symmetry and swimmer propels.

In 2015, C. Haug et al. have shown that they are able to create soft robotic swimmer using light actuated materials [18]. The light-driven liquid-crystal (LDLC) material [90] containing azobenzene chromophore, sensitive to ultra-violet light, can convert light into the mechanical energy with quick response and large deformation. The irradiation of UV light bends the film that can be recover by visible light. Azobenzene chromophore has very rapid phase transition, so the deformations of the LDLC film are very spontaneous

with light irradiation, so can be controlled by the light. To build the device with the help of LDLC material, Haug et al. used LDLC film attached with a rigid head and make an arrangement of UV and visible light as shown in figure 2.11. Where synchronous irradiation of UV light at the selective portion of the film make the film bend and irradiation of visible light make the film straight again. The periodic irradiation of UV and visible light provides a periodic deformation to the LDLC filament which results the locomotion.

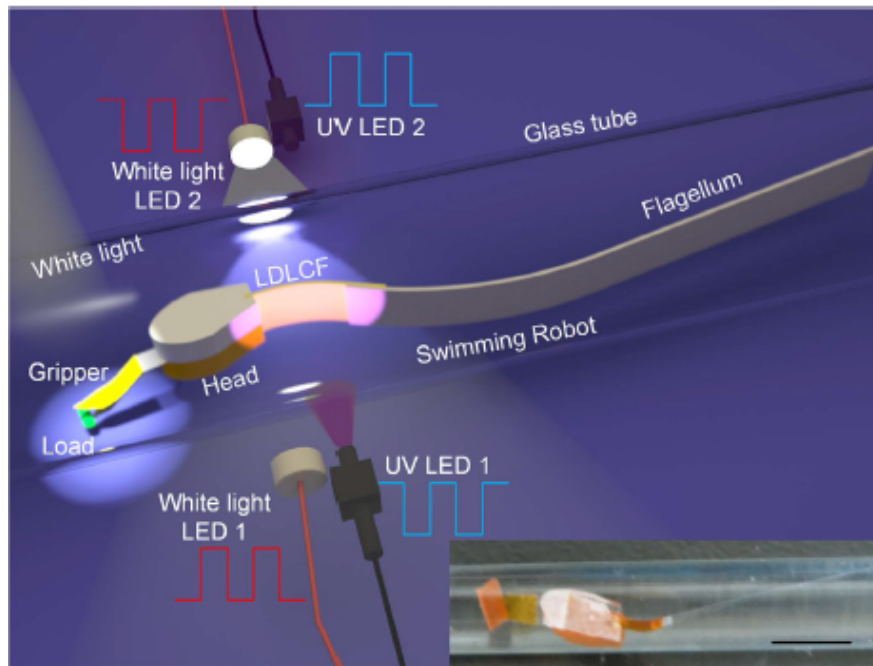


Fig. 2.11 Schematic of soft robotic light sensitive micro swimmer and light irradiation system, proposed by C. Haug et al [18].

But again all these studies are focused on a single arm or single filament swimmer. E. Lauga proposed multiple flexible filaments swimmer as shown in figure 2.12. He provided an analytical treatment of the locomotion of the flexible swimmer within the limit of small amplitude approximation. He showed that the proposed multi-filament swimmers follow straight swimming trajectories [19]. He argued that this is the simplest swimmer which takes benefit of the coupling between drag and bending forces for locomotion. Additionally, B. J. Williams et al. have also given the experimental evidence that a bio-hybrid two-tailed swimmer, actuated by heart muscles can achieve much higher speeds as compared to simple one-head and one-tail swimmer [17]. The one-tail bio-hybrid swimmer swims at a speed $5\text{--}10 \mu\text{m}/\text{s}$, while two-tail swimmer is able to attain a

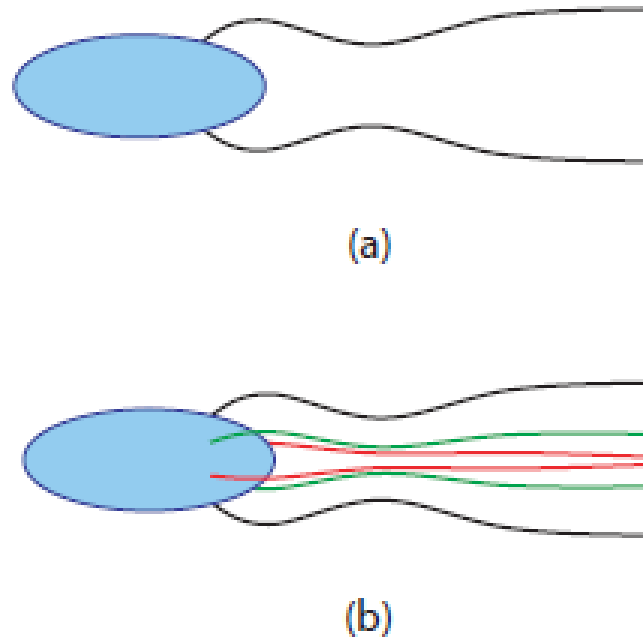


Fig. 2.12 Schematic of multi-filament swimmer. (a) Swimming with two symmetric filaments, in planer motion. (b) Swimming with six filaments in planer motion, proposed by E. Lauga [19].

swimming speed $81 \mu\text{m}/\text{s}$. In the present work we have proposed a very simple artificial swimmer known as one-hinge swimmer, it contains two arms. The idea to make this swimmer is originated from a Scallop theorem itself. As Scallop theorem states that a swimmer with one-hinge can not propel in a viscous fluid itself because it has only one degree of freedom. We consider a swimmer with one-hinge, identical to a scallop, which has two flexible arms, as we know that flexibility can break the Scallop theorem. The two filament swimmer proposed by Lauga did not consider hydrodynamic interactions between the filament and the swimmer body, which should be included. In our one-hinge swimmer, we consider hydrodynamic interaction between two arms and our swimmer does not contain a head.

Chapter 3

Modelling and simulation techniques

There are three approaches to study the dynamics of an artificial micro-swimmer surrounded by a fluid, *i*) analytical *ii*) experimental and *iii*) computational. For simple geometries, one can use analytical approach. But for complex geometries it becomes an arduous task to solve flow field equations analytically and experiments have their own limitations. But nowadays, thanks to modern computers comprising of high speed computing processors and reducing computation costs have made computational approach as an alternative to the analytical approach. In this work we have also opted the computational approach. The problems that are herculean or almost impossible to solve analytically, like the calculation of countless interactions between molecules and collective behavior that contain many degrees of freedom. These problems can be tackled quickly through computer simulations, which can be referred as in-silico studies. In-silico studies have full hold over the simulation parameters, measurements, interactions, etc. and these allow us to determine which factors play important role. This approach can direct us to a better fundamental understanding of the problems. In the present work, we deal with coarse grained fluid medium which makes the simulation computationally very efficient. So particularly we need a mesoscopic method that can efficiently solve the Navier-Stokes equations with thermal fluctuations. In this work mainly the Multi-Particle Collision Dynamics (MPC) simulation technique is employed. The benefit of MPC is that it solves the Navier-Stokes equation and also has inherent thermal fluctuations [91, 92], which resembles real fluids. Using this technique, a variety of hydrodynamic problems in low Reynolds number have been solved. For example, swimming of the sperm cells [93], squirmer [94, 95], African trypanosome [96], E. Coli [97], Taylor line [98], spheroidal

micro-swimmer [99] etc. Previous studies show that this method is computationally efficient for low Reynolds number hydrodynamics. The micro-swimmers that move by deforming their surface can be simulated by coupling them to the surrounding fluid at low Reynolds numbers using MPC [93, 96, 98, 100]. We have chosen this method as it is very easy to implement and is also one of the most efficient methods in the Stokes limit [101, 102]. We have utilized the technique with Anderson thermostat, where both linear and angular momentum are conserved [102]. The continuous beating pattern of the swimmer keeps imparting the energy into the fluid which increases the temperature of the system. The Anderson's thermostat which is inbuilt in the simulation method, keeps the temperature of the system stable.

3.1 Multi-Particle Collision Dynamics

Multi-particle collision dynamics is a particle based coarse-grained simulation technique for fluid flow which was proposed by Malevanets and Kapral in 1999 [91, 92]. MPC conserves mass and momentum globally as well as locally and includes hydrodynamic interactions with thermal fluctuations. MPC is a particle based method, where we use fictitious point particles of mass m_0 to mimic the fluid medium. MPC consists of two steps, one is called the streaming step and another one is called the collision step.

3.1.1 Streaming step

In streaming step, each fluid particle moves ballistically within a discrete time interval δt . We update the position $\mathbf{r}_i(t)$ of all the fluid particles at time t according to

$$\mathbf{r}_i(t + \delta t) = \mathbf{r}_i(t) + \delta t \mathbf{v}_i(t). \quad (3.1)$$

Where $\mathbf{v}_i(t)$ is the velocity of i_{th} particle at time t and δt is the MPC time step.

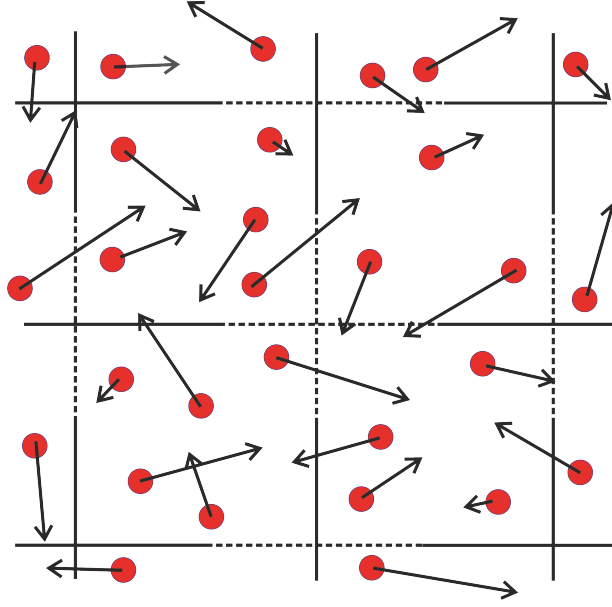


Fig. 3.1 The streaming step (algorithm 3.1)

3.1.2 Collision step

In collision step, momentum transfer takes place between fluid particles. To perform collision step, the simulation box is divided into square collision cells of size a_0 . The collision step keeps mass and momentum conserved on a cell level. In collision step, the velocity of each particle $\mathbf{v}_i(t)$ is updated according to

$$\mathbf{v}_i(t + \delta t) = \mathbf{u}(t) + \mathbf{v}_i^{ran} - \sum_{cell} \mathbf{v}_i^{ran} / N_c(t). \quad (3.2)$$

Where $\mathbf{u}(t) = \sum_{cell} \mathbf{v}_i(t)m_0 / \sum_{cell} m_0$ is the center of mass velocity of j_{th} cell, \mathbf{v}_i^{ran} is a random value for i_{th} particle taken from a Gaussian distribution with variance $k_B T / m_0$ and $N_c(t)$ is the number of particles in j_{th} cell at time t . The number of particles in one cell can vary from another cell, but the average particles per cell or average number density N_a remain unchanged. Basically, in collision step a new randomly picked velocity is assigned to each fluid particle. The velocity of i_{th} particle in j_{th} cell is the center of mass velocity of the cell $\mathbf{u}(t)$ plus its new random value assigned from a Gaussian distribution minus the mean of all the new random values for j_{th} cell (see figure 3.2). Though the individual velocity of each particle is assigned randomly but the center of mass velocity of the cell does not change as

$$\mathbf{u}(t + \delta t) = \mathbf{u}(t). \quad (3.3)$$

So the momentum remains constant as well.

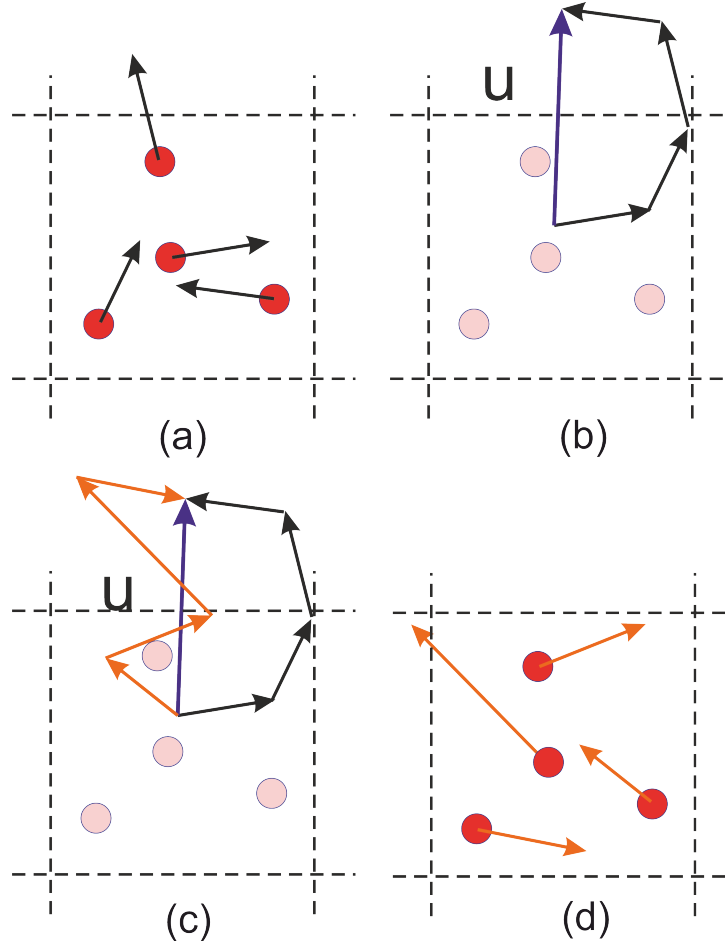


Fig. 3.2 Depiction of MPC-AT collision algorithm. (a) Sort particle into cells, (b) calculate the center of mass velocity \mathbf{u} of the cell, (c) for each particle generate a random velocity such that the center of mass velocity remains \mathbf{u} and (d) apply this new velocity to each particle.

3.1.3 Grid shifting

Due to the discretization of the space into cells, the system no longer remains Galilean invariant. This happens when the mean free path of the fluid particles or MPC time step δt is much smaller than the cell size a_0 . Because in this condition, particles mostly fail to move far enough to leave the cell and due to that they repeatedly exchange momentum with the same set of neighboring particles. The Galilean invariance can be restored by performing a random shift (see figure 3.3) of the simulation box in the interval $[-a_0/2, a_0/2]$ as proposed by Ihle et al. [103, 104]. If δt is comparable or larger than

cell size a_0 , then there is no need to perform the grid shift. In the present work, the MPC is used to simulate a solvent ($\delta t \ll a_0$). However, if δt is too large, MPC behaves as a gas rather than a liquid. In this case fluid becomes quite compressible [105]. In the case of gas, the value of Schmidt number i.e. the ratio of the viscosity to the diffusion coefficient ($Sc = \mu/D$) becomes small, around $Sc \sim 1$. While real liquids often offer Schmidt numbers ranging between $Sc \sim 10^2 - 10^3$. Many particles based simulation methods like molecular dynamics (MD) [106], dissipative particle dynamics (DPD) [107, 108] etc. struggle to achieve appropriately large Schmidt number. The good thing of MPC is that one can obtain large value of $Sc \sim 10^2$. As the value of δt decreases, Sc increases and contrary to this when δt increases, Sc decreases (tending towards gas behavior).

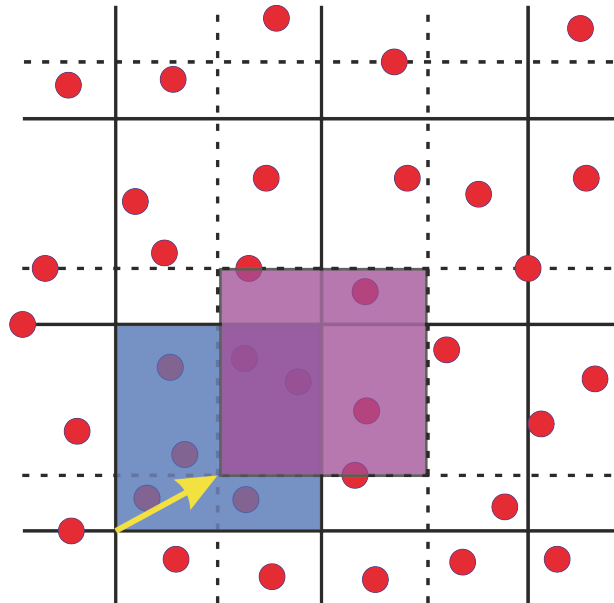


Fig. 3.3 Picture of random shift of the collision cell.

3.1.4 Angular momentum conservation

The MPC-AT (multi-particle collision dynamics with Anderson thermostat) algorithm (equation 3.2) conserves mass, linear momentum but it is unable to conserve angular momentum. However, equation 3.2 can be expanded to (equation 3.4) conserve angular momentum.

$$\mathbf{v}_i(t + \delta t) = \mathbf{u}(t) + \mathbf{v}_i^{ran} - \sum_{cell} \mathbf{v}_i^{ran} / N_c + \left\{ m_0 \mathbf{I}^{-1} \sum_{j \in cell} [\mathbf{r}_{j,c} \times (\mathbf{v}_j - \mathbf{v}_j^{ran})] \times \mathbf{r}_{i,c} \right\}. \quad (3.4)$$

Here $\mathbf{r}_{i,c} = \mathbf{r}_i - \mathbf{R}_c$ is the relative position of i_{th} particle with respect to the center of mass position \mathbf{R}_c of j_{th} cell, \mathbf{I} is the moment of inertia of j_{th} cell about center of mass. To conserve angular momentum of the cell, $\mathbf{r}_{i,c}$ is crucial. The MPC-AT algorithm shown in equation 3.2 generates a small difference $\delta \vec{\mathbf{L}}$ in angular momentum after performing a collision step. This amount of angular momentum can be absolutely removed by providing an appropriate angular velocity $\vec{\boldsymbol{\omega}}$ to the cell. The angular velocity required to cancel the $\delta \vec{\mathbf{L}}$ is $\vec{\boldsymbol{\omega}} = \mathbf{I}^{-1} \delta \vec{\mathbf{L}}$. So an extra term corresponding to the change in linear velocity (resulting from the imposed angular velocity about the center of mass) is required to conserve angular momentum, as can be seen in equation 3.4. We can refer the algorithm 3.2 and 3.4 as MPC-AT-a (MPC-AT without angular momentum conservation) and MPC-AT+a (MPC-AT with angular momentum conservation) respectively.

3.1.5 Expressions for transport coefficients

The advantage of MPC is that we have analytic expressions for viscosity calculation. The total kinematic viscosity μ is the sum of the kinetic viscosity μ^{kin} and collision viscosity μ^{col} . The expressions for MPC-AT-a are [109–111]

$$\mu^{kin} = \frac{k_B T \delta t}{m_0} \left(\frac{N_a}{N_a - 1 + e^{-N_a}} - \frac{1}{2} \right) \quad (3.5a)$$

$$\mu^{col} = \frac{a_0^2}{12 \delta t} \left(\frac{N_a - 1 + e^{-N_a}}{N_a} \right), \quad (3.5b)$$

therein N_a is the average number of particles per cell. The term e^{-N_a} is due to the fluctuation and it becomes crucial for $N_a \leq 3$.

In MPC-AT+a for sufficient number of N_a [112, 111] (in our case we always consider ten particles per cell) the expressions are

$$\mu^{kin} = \frac{k_B T \delta t}{m_0} \left(\frac{N_a}{N_a - (d+2)/4} - \frac{1}{2} \right) \quad (3.6a)$$

$$\mu^{col} = \frac{a_0^2}{24\delta t} \left(\frac{N_a - 7/5}{N_a} \right). \quad (3.6b)$$

By reducing δt we can increase the viscosity but in the cost of the more simulation time.

3.1.6 Boundary Conditions

Periodic boundary Conditions

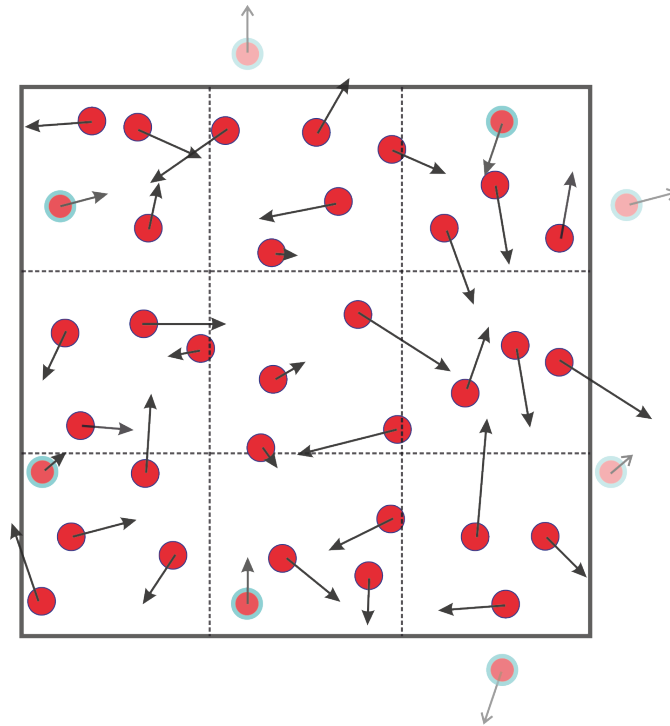


Fig. 3.4 Periodic boundary conditions. The positions of particles that are outside the constrained area are shifted to the opposite end.

The application of periodic boundary conditions (PBC's) is that by using this, one can mimic the bulk unbounded fluid. PBC's wrap the simulated fluid such that the positions of the particles that come outside the controlled volume are shifted to the opposite side as shown in figure 3.4. Imagine we have a 2-dimensional (2-D) square simulation box having side length L_{box} . The co-ordinates of the corners of the simulation

box are $(0, 0)$, $(L_{box}, 0)$, (L_{box}, L_{box}) and $(0, L_{box})$. After performing a streaming step, we implement the conditions i.e. the particles which have been positioned $\mathbf{r}_i(t) > L_{box}$ or $\mathbf{r}_i(t) < 0$ are shifted according to $\mathbf{r}_i(t) - L_{box}$ or $\mathbf{r}_i(t) + L_{box}$ respectively (see figure 3.4). In 2-D this situation is exactly like a paper sheet is folded into a cylindrical shape as depicted in figure 3.5. The MPC involves hydrodynamic interactions, so in the case of PBC's the simulation box has to be chosen appropriately to avoid the box size effect.

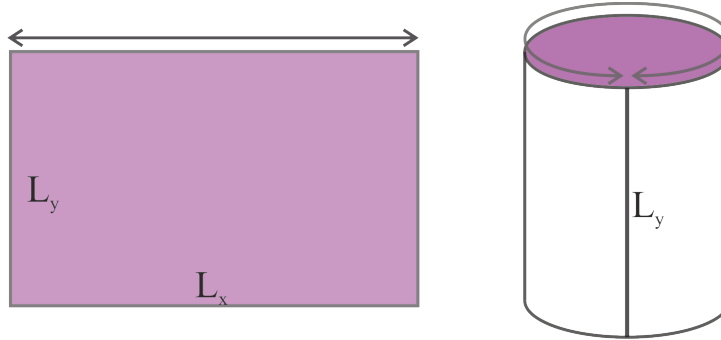


Fig. 3.5 Schematic of a 2-D periodic boundary conditions. PBC's wrap the system.

Solid boundary Conditions

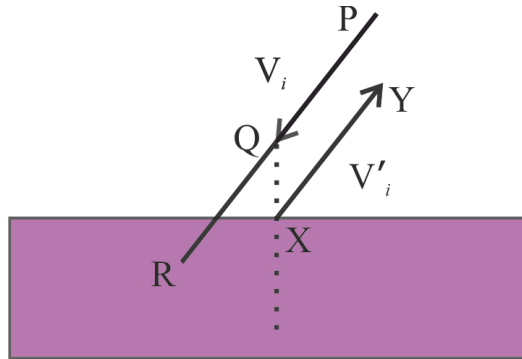


Fig. 3.6 Schematic of solid boundary conditions.

If the fluid is confined between the solid walls, then the fluid flow near the walls comply the no-slip boundary conditions. No-slip BC's refers to any solid and impenetrable boundary that leads to zero velocity (or equals to wall's velocity) of the fluid particles that interact with the wall. To implement the no-slip BC's in the MPC fluid, we allow the effective fluid particles interact with the walls using the bounce-back rules [113], see figure 3.6. In bounce-back rules, when a fluid particle travels into a solid wall to position R after performing a streaming step, we invert the velocity $\mathbf{v}'_i(t) = -\mathbf{v}_i(t)$ and allow the

particle to move ballistically to position Q for half the collision time according to

$$\mathbf{r}_i(t + \delta t/2) = \mathbf{r}_i(t) + \mathbf{v}_i'(t)\delta t/2. \quad (3.7)$$

After this, we shift the particle to the nearest spot on the solid wall at position X and then allow it to stream with the velocity $\mathbf{v}_i'(t)$ for remaining half the collision time (to position Y) [114]. To improve the no-slip BC's, virtual particles are required to distribute inside the solid boundary [113, 115].

Virtual particles

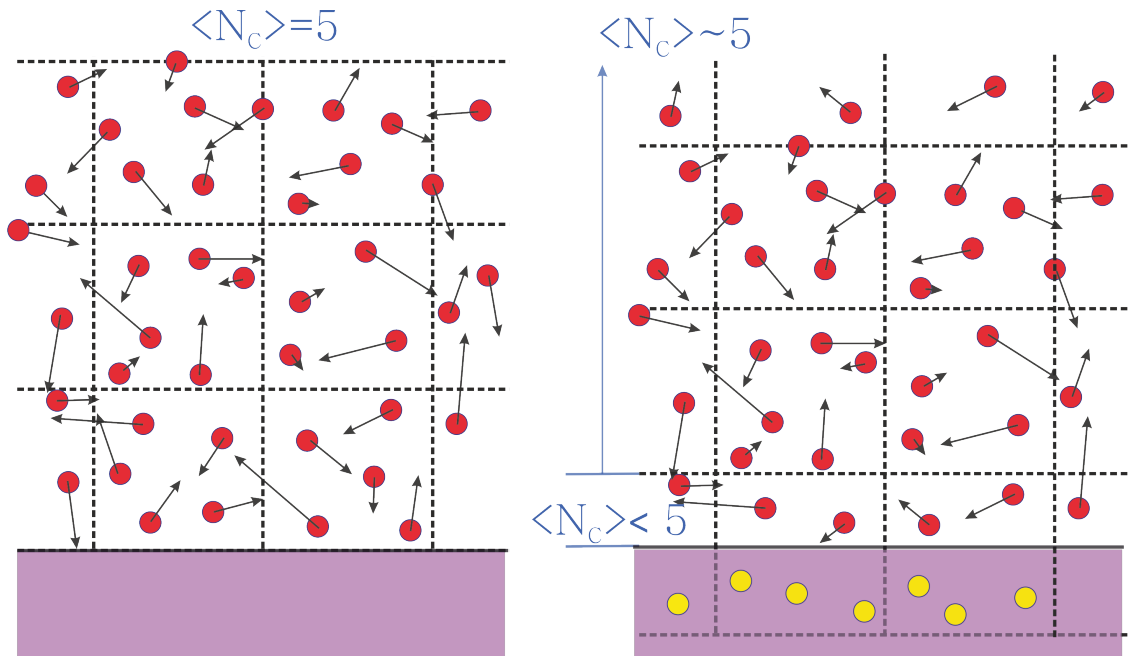


Fig. 3.7 Inclusion of the virtual particles. In case of (a) virtual particles are not required and in (b) virtual particles are needed. In the figure, virtual particles are colored as yellow.

The implementation of the perfect no-slip BC's solicit bounce-back rules with the incorporation of virtual particles. Simple bounce-back rules (without virtual particles) are effective for insuring no-slip only when the wall strictly coincides with the boundaries of neighboring MPC cells. However, generally walls do not coincide with neighboring cells or can be parallel to the neighboring cells. Also, when we perform the random grid-shift to restore Galilean invariance, simple bounce-back BC's collapse to ensure no-slip [116]. This is because the cell overlaps with solid boundary and some part of the cell is not accessible to the solvent particles and so the cell remains partially empty. So

the average particles per cell N_a decreases near the wall and viscosity as well. It was proposed that in this kind of situation, to ensure no-slip BC's, virtual particles should be employed [113, 117]. We uniformly distribute virtual particles ($N_{virtual} = N_a - N_c$) in the region of the collision cells that is cut by the solid boundary as depicted in figure 3.7(b). This makes the density of the fluid near the wall equal to the average density N_a . The velocity components of the virtual particles are taken from a Gaussian distribution with variance $k_B T / m_0$. These virtual particles are incorporated in the collision step. This ensures in-compressible fluid as well as no-slip [113, 118, 119].

3.1.7 Brownian MPC

Often the hydrodynamic interactions (HI's) in complex fluids are crucial. One of the useful features of the MPC is that one can switch-off the HI's. Sometimes it is useful to do a comparative study with and without HI's or turn off hydrodynamic interactions for some parts of the study [120–125]. The methods for turning off HI's in MPC simulations have been shown in Refs. [120, 121]. Basically, a MPC fluid can be constrained to behave as a BD (Brownian dynamics) fluid, with no HI's, by randomly interchanging the velocities of the MPC fluid particles after each collision step (see figure 3.8). In this case momentum on cell level is not conserved.

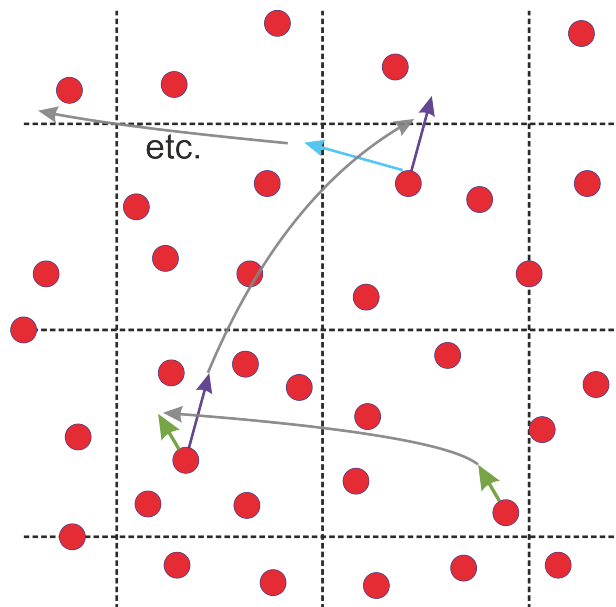


Fig. 3.8 Distortion of hydrodynamic interactions (Brownian fluid) by randomly interchanging the velocity of the solvent particles.

3.2 Modelling of the swimmer

3.2.1 2-D one-hinge or scallop swimmer

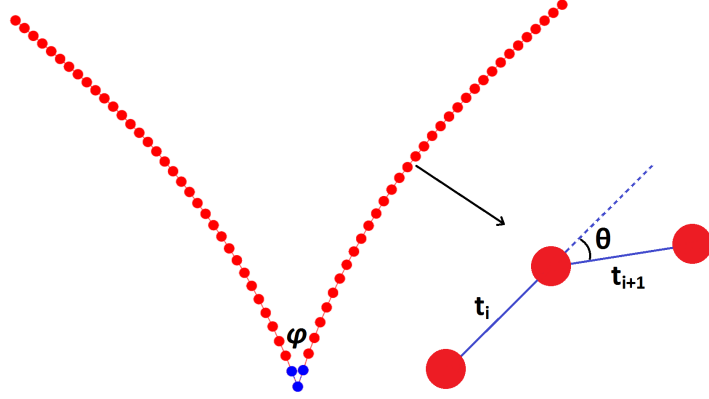


Fig. 3.9 The snapshot of a model one-hinge artificial swimmer with flexible arms. Three mass points are given blue color to show that the bending waves pass through only these three points. We have magnified the bond vectors \mathbf{t}_i and \mathbf{t}_{i+1} , which connect neighboring mass points and make an angle θ . φ is the angle between two arms near the hinge.

To model a one-hinge swimmer, we take a chain of N_b beads connected with springs [126], where each bead has unit mass m_0 and rest length of the spring is $l_0 = 0.5$. The middle bead of the chain acts as a hinge for the swimmer. So we always consider odd number of beads to make the length of the arms equal, as can be seen in figure 3.9. The spring potential between the beads is given by

$$\frac{U_s}{k_B T} = \frac{1}{2} K_s (l - l_0)^2. \quad (3.8)$$

Where K_s is the spring constant and l is the length of the spring at any given time. To make sure that the springs remain relatively stiff during the simulations, we use a high spring constant $K_s = 10^8$ in the case of 2-D one-hinge swimmer. To control the flexibility along the arms of the swimmer, we introduce a three body bending potential

$$\frac{U_b}{k_B T} = K_b (1 - \cos \theta). \quad (3.9)$$

Where K_b is the rigidity constant and θ is an angle between two bond vectors \mathbf{t}_i and \mathbf{t}_{i+1} . We apply the bending potential along both the arms of the swimmer except for the hinge points. By varying the value of K_b , we can change the flexibility of the arms. When

$K_b \rightarrow \infty$, it means swimmer has completely rigid arms and when $K_b \rightarrow 0$, swimmer has completely flexible arms.

To obtain a hinge in the middle of the chain or between the two arms and also to achieve the opening and closing beating pattern of the arms, we introduce a three body bending wave potential along the three blue colored beads (see figure 3.9) given by

$$\frac{U_w}{k_B T} = \frac{1}{2} K_w [\mathbf{t}_{i+1} - \mathbf{R}(l_0 \alpha) \mathbf{t}_i]^2. \quad (3.10)$$

Where K_w is a bending rigidity constant that decides the strength of the potential, \mathbf{R} is the rotation matrix, $\phi = l_0 \alpha$ is the angle between the two bond vectors where this potential is applied, $\alpha = A \sin^2(2\pi \nu t)$ is the spontaneous curvature, ν is the frequency of beating and A is the amplitude of the wave. The matrix \mathbf{R} rotates one bond vector \mathbf{t}_i against the neighboring bond vector \mathbf{t}_{i+1} about a unit vector which is perpendicular to \mathbf{t}_i and \mathbf{t}_{i+1} by an angle ϕ . As the curvature α is function of square of the sine wave, we will have only positive values for curvature. Thus the angle φ between the arms can vary only between $0 - \pi$. When two arms are completely opened (i.e. zero curvature position), the angle φ will be the maximum $\varphi_{max} = \pi$ at that time. The value of $K_w = 4 \times 10^5$ is used in the present work. The total force on the i_{th} bead of the swimmer due to spring and bending potentials is given by

$$\mathbf{F}_i = -\nabla_i (U_s + U_b + U_w). \quad (3.11)$$

Note that the total force and the total torque on the entire swimmer is always zero,

$$\Sigma \mathbf{F}_i = 0, \quad \Sigma \mathbf{T}_i = 0. \quad (3.12)$$

3.2.2 3-D scallop swimmer

In order to build the three dimensional elastic scallop, we again use bead spring model. The schematic of the scallop is as shown in figure 3.10. Here, we consider a sheet of length L and width W , made up of beads [126]. The middle beads act as a hinge and we always take an odd number of beads or mass points in the direction of length so that we can divide the sheet into two equal flaps as shown in figure 3.10. The spring potential between the beads is given by equation 3.8. The equilibrium distance between the beads

is $l_0 = 0.5$. The first nearest and the second nearest (diagonal one) neighboring beads are connected with the potential K_s as illustrated in 3.10(i). To ensure that the springs are really stiff, we have used a high spring constant $K_s = 10^6$.

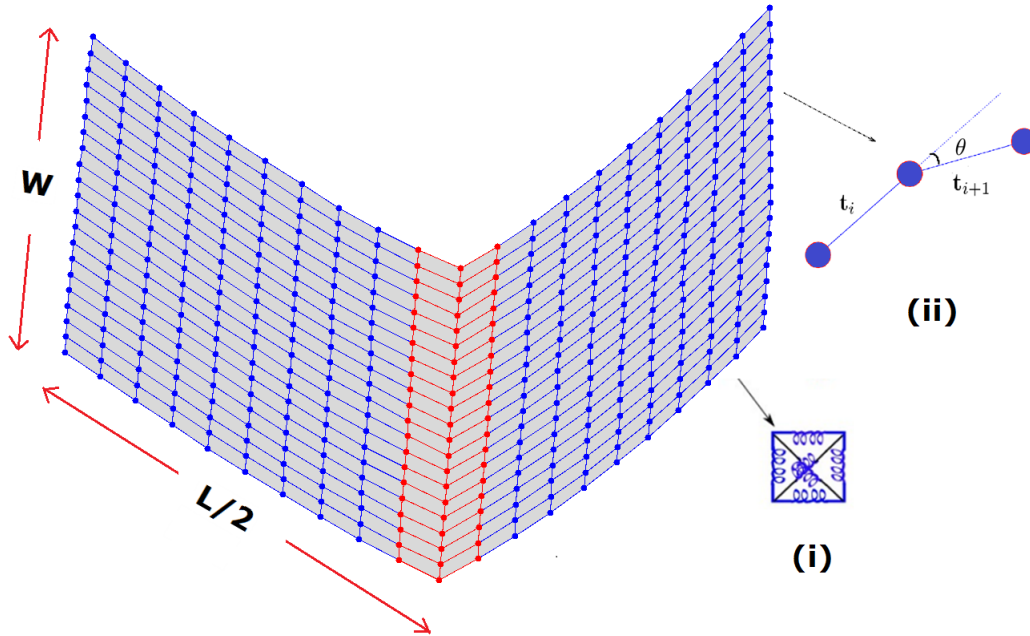


Fig. 3.10 The schematic for 3-D model scallop; here middle beads are given in red color to show that the bending waves pass only through these beads. The blow up (i) illustrates that nearest and next nearest beads are connected with spring potential; blow up (ii) shows the bond vectors \mathbf{t}_i and \mathbf{t}_{i+1} which connect neighboring beads and makes an angle θ .

The flaps of the scallop are made semi-flexible by employing a three body bending potential given in equation 3.9. We have applied the bending potential along both the length and width directions except for the hinge (red) beads. In the direction of length we consider the bending rigidity constant $K_b = K_{b_L}$ and in the direction of width $K_b = K_{b_W}$. The hinge separates the sheet into two equal flaps. When we consider $K_b \rightarrow \infty$, we have completely stiff flaps of the scallop and when $K_b \rightarrow 0$, we have completely flexible flaps.

To provide the actuation or opening and closing to scallop, we introduce a three body bending wave potential K_w along the hinge beads that is given by equation 3.10. We have used curvature $\alpha = A \sin^2(2\pi\nu t)$, so that the flaps of the scallop can make an angle between $0 - \pi$. The angle ϕ can be controlled by the potential K_w and amplitude A . The total force experienced by i_{th} bead of the scallop due to all the potentials is given by equation 3.11.

3.2.3 3-D Taylor sheet

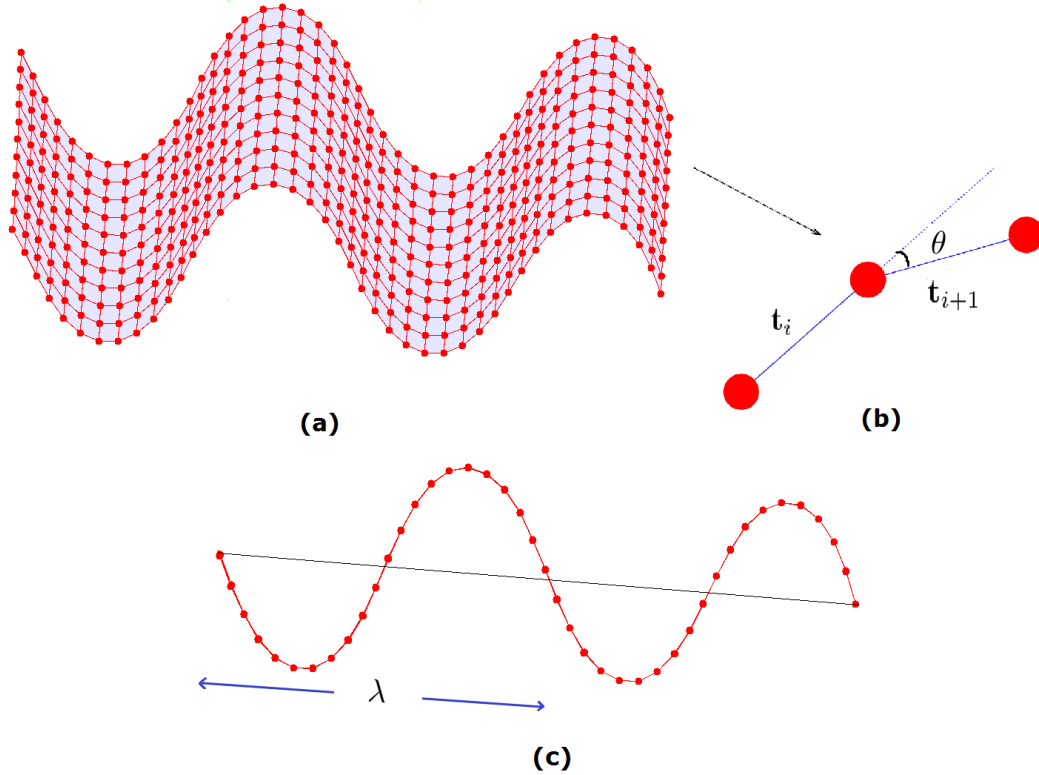


Fig. 3.11 (a) Snapshot of waving sheet swimmer as obtained from the simulation. (b) Magnification of bond vectors between the beads and θ is the angle between the bond vectors along the width. (c) 2-D projection of the sheet that depicts two wave trains each having wavelength λ .

In the present study, we have also modelled a three dimensional sheet using bead spring model as illustrated in figure 3.11. In figure 3.11(a), we have shown the structure of the waving sheet as obtained from simulations. Each bead with a radius $a = l_0/3$ is connected to four other beads with Hookean springs, here l_0 is the center to center distance between two nearest beads in equilibrium [11]. In order to prevent the sheet from in-plane shear, next nearest neighbors are also connected with Hookean springs. The potential energy of Hookean springs is given in equation 3.8. To ensure that the variation of l is always very small as compared to l_0 , we consider relatively stiff springs. In order to restrict the sheet from crumbling, we employ a bending potential along the width of the sheet. The bending potential is given in equation 3.9. In order to make the sheet oscillate, we apply bending wave potential along the length of the sheet [127] as given in equation

3.10. Here $\alpha = A \sin(k_c d - 2\pi\nu t)$ is the curvature which is a function of time t , d is the distance of the bead from one of the edges of the sheet, A is the amplitude of the applied wave, $k_c = 2\pi/\lambda_c$ is the wave number, λ_c is the contour wavelength and \mathbf{t}_i is bond vector that connects the center of two beads. Note that the actual wavelength λ is different from λ_c [98]. We measure λ as end to end distance in the waving sheet divided by the number of wave trains. Here we refer to a wave train for a wave with one complete wavelength, for instance, in figure 3.11(c) sheet contains two wave trains. The total force on the sheet is given by equation 3.11.

Molecular dynamics

In our case, we have employed the Molecular Dynamics simulation to provide movement to the swimmer. MD technique numerically integrates the equation of motion for a number of particles that interact through a set of potentials [106]. The total force on each bead of the swimmer can be calculated from the applied potentials ($\mathbf{F}_i = -\nabla_i U$). The second law of Newton calculates the acceleration of the beads \mathbf{F}_i/m_0 . We update the velocities and positions of the beads using a velocity Verlet algorithm [128–130].

$$\mathbf{r}_i(t + \delta t_{MD}) = \mathbf{r}_i(t) + \delta t_{MD} \mathbf{v}_i(t) + \frac{1}{2} \delta t_{MD}^2 \frac{\mathbf{F}_i(t)}{m_0} \quad (3.13a)$$

$$\mathbf{v}_i(t + \delta t_{MD}) = \mathbf{v}_i(t) + \frac{1}{2} \delta t_{MD} \left\{ \frac{\mathbf{F}_i(t) + \mathbf{F}_i(t + \delta t_{MD})}{m_0} \right\} \quad (3.13b)$$

Therein δt_{MD} is integration or MD time step. In our simulation we choose MD time step very small $\delta t_{MD} = 10^{-4}$ to keep the swimmer stable.

In the case of unbound fluid, if the position of any bead of the swimmer come outside the constraint volume, in that condition we terminate the simulation. In contrast to this, if beads interact with solid wall then bounce-forward BC's are applied. Bounce-forward BC's are pretty alike to the bounce-back BC's employed for the fluid particles. If any bead of the swimmer moves into a wall, we place the particle at the position X (see figure 3.6). But in contrary to the bounce-back BC's, only the velocity component of the bead orthogonal to the wall is reversed. This makes sure that the swimmer can slip along a wall.

3.3 Coupling of the swimmer with the fluid particles

The artificial swimmer in the present work is surrounded by MPC fluid medium. Therefore, the dynamics of the swimmer must be coupled to the fluid medium. In streaming step of MPC, we only consider the fluid particles and during this step we allow the fluid particle to pass through the swimmer as can be seen in figure 3.12. We incorporate beads of the swimmer with the fluid particles in the collision step, thereby beads interact with the fluid particles. So in the collision step, beads exchange momentum with the fluid environment. This ultimately couples the swimmer to the fluid environment and gives the correct hydrodynamics for the swimmer [126, 131, 132]. Note that the beads of the swimmer have same mass as that of fluid particles.

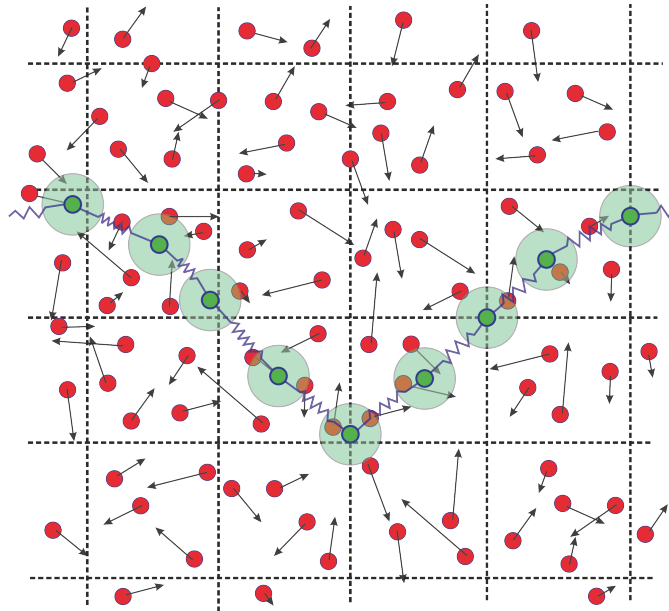


Fig. 3.12 Coupling of the swimmer with fluid particles, where fluid particles can pass through the swimmer body.

3.4 Implementation

In order to perform the simulation, first of all we initialize the parameters. Then we constraint the volume or area of the simulation box and assign the position of the fluid particles from a uniform distribution within the simulation box. The initial velocities of the particles and beads of the swimmer are assigned from a Gaussian distribution with variance $k_B T / m_0 = 1$, which saves the simulation time that consume to achieve equilibrium. Initially the position coordinates of the beads of a 2-D/3-D swimmer are

Basic units	Derived units
$a_0 = \text{length}$	$\tau_0 = a_0 \sqrt{\frac{m_0}{k_B T}} = \text{time}$
$k_B T = \text{energy}$	$D = a_0 \sqrt{\frac{k_B T}{m_0}} = \frac{a_0^2}{\tau_0} = \text{diffusion constant}$
$m_0 = \text{mass}$	$\mu = a_0 \sqrt{\frac{k_B T}{m_0}} = \frac{a_0^2}{\tau_0} = \text{kinematic viscosity}$
	$\eta = a_0 \frac{\sqrt{m_0 k_B T}}{a_0^2} = \frac{m_0^2}{\tau_0 a_0} = \text{dynamic viscosity}$

Table 3.1 Units associated with MPC algorithm.

considered in a straight line/sheet, having a gap of l_0 , in the middle of the simulation box. Once we have the position of the beads we can calculate the force on each bead using equations 3.8-3.11. Then we perform $\delta t / \delta t_{MD}$ number of MD steps before a MPC step. Where, we update the position and velocity of the beads according to the equation 3.13. Note that after every MD step we check the BC's for the beads. After this, we execute MPC step, where first we perform streaming step (equation 3.1) for the fluid particles with BC's. Then perform a grid shift to achieve Galilean invariance and again checked for BC's. After this, we perform a collision step (equation 3.4) for the fluid particles (plus virtual particles if needed) and beads of the swimmer. After the collision step, we shift the collision cells back. Then repeat the process (after initialization) till the desired simulation time.

In the present work, we have measured quantities in MPC units where length is normalized with a_0 , mass with m_0 , energy with $k_B T$ and time with $\tau_0 = a_0 \sqrt{m_0 / k_B T}$ [133]. We have used $a_0 = 1$, $m_0 = 1$ and $k_B T = 1$ which makes the time unit equals to unity. On the basis of these basic units, we can derive the other units as shown in table 3.1 [133]. Also, we can compare the MPC units with the physical units. For example, the length of the considered swimmer is $L = 40 \mu m$ in physical units and in MPC units it is $L = 40 a_0$. That means $a_0 = 1 \mu m$. Lets say the density of the fluid is equal to the density of the water i. e. $\rho_W = \rho m_0 / a_0^3 = 1000 \text{ kg m}^{-3}$. If $\rho = 10$ in our simulation then the mass of the fluid particles in physical units will be $m_0 = 3 \times 10^{-16} \text{ kg}$. Let us consider, we are working at room temperature $T \approx 300 \text{ K}$. Once we know all the basic parameters in terms of the physical units, then we can calculate other parameters. For

instance, time in the physical units will be $\tau_0 = a_0\sqrt{m_0/k_B T} = 3 \times 10^{-4} s$. Similarly we can calculate other parameters using table 3.1.

Chapter 4

Locomotion of a flexible one-hinge swimmer in Stokes regime

E. M. Purcell showed that a body has to perform non-reciprocal motion in order to propel itself in a highly viscous environment. The swimmer with one degree of freedom is bound to do reciprocal motion, whereby the center of mass of the swimmer will not be able to propel itself due to the Scallop theorem. In the present study, we are proposing a new artificial swimmer called the one-hinge swimmer. Here we will show that flexibility plays a crucial role in the breakdown of Scallop theorem in the case of one-hinge swimmer or two-dimensional scallop at low Reynolds number. To model a one-hinge artificial swimmer, we use bead spring model for two arms joined by a hinge with bending potential for the arms in order to make them semi-flexible. The fluid is simulated using a particle based mesoscopic simulation method called the multi-particle collision dynamics with Anderson thermostat. Here, we show that when our swimmer has rigid arms, the center of mass of the swimmer is not able to propel itself as expected from the Scallop theorem. When we introduce flexibility in the arms, the time reversal symmetry breaks in the case of the one-hinged swimmer without the presence of a head contrary to the one-armed super paramagnetic swimmer which required a passive head in order to swim. The reduced velocity of the swimmer is studied using a range of parameters like flexibility, beating frequency and the amplitude of the beat, where we obtain similar scaling as that

of the one-armed swimmer. We also calculate the dimensionless Sperm number for the swimmer and we get the maximum velocity when the Sperm number is around ~ 1.8 .

4.1 Introduction

Microorganisms have adapted their locomotion to the harsh environment of low Reynolds number regime by invoking different swimming strategy [56]. For example, the E. Coli moves by rotating its helical flagellum [25, 26], Chlamydomonas flagella have a breast stroke kind of motion [51], African Trypanosome has a helical flagellum attached to the cell body with a planar wave passing through it [96, 134], etc. Swimming of these kind of natural swimmers has been investigated for the last half-century [24–26, 51, 56, 75, 96, 134, 135]. As a result of these studies, artificial swimmers have also been proposed like Taylor sheet [63], Purcell’s two-hinge swimmer [10, 136], three-linked spheres swimmer [64], Elastic two-sphere swimmer [68] and Three-sphere with a passive elastic arm [67] etc, which have further enhanced our understanding about low Reynolds number swimmers. One of the challenges in proposing an artificial swimmer lies in the fact that the proposed movement stroke should not be reciprocal otherwise it cannot propel itself due to the Scallop theorem. In Scallop theorem, Purcell had argued that a swimmer with one-hinge or one degree of freedom is bound to perform reciprocal motion and thus will not be able to swim in the Stokes regime [10, 56].

Purcell proposed two possible ways to elude from Scallop theorem, one is “corkscrew” [25, 137] motion and second is “flexible oar” [79, 83] motion. Using the concept of flexible oar, Dreyfus et al. [15] reported a micro swimmer that exploits elastic property of a slender filament made up of paramagnetic beads. To break the time inversion symmetry, a passive head was attached to the flexible arm. The passive head reduces the velocity of the flexible swimmer. Bigger the head, higher is the drag force experienced by the swimmer. The head is essential for swimming because without it the tail performs a reciprocal motion and the velocity of the swimmer reduces to zero [19].

In the present study, we design and simulate a two-dimensional swimmer having two symmetric arms joined by a single hinge that looks like a two-dimensional scallop. The arms of the swimmer are semi-flexible and thus behaves as an elastic scallop. To

design an elastic scallop swimmer, we use bead spring model [126] for the two arms joined by a common bead which acts as a hinge, and to introduce flexibility to the two symmetric arms of the swimmer we use bending potential [128]. The actuation happens only at the hinge and the rest of the arm relaxes depending on the strength of the actuation similar to the one-armed flexible swimmer [79]. In case of the elastic scallop, the time inversion symmetry is broken because through the viscous drag term time enters into the equation of the filament shape similar to the one-armed swimmer. Hydrodynamic interactions between the arms of the swimmer are implemented using the particles based simulation method for the fluid called as multi-particle collision dynamics (MPC) [102]. The advantage of MPC is that it solves the Navier-Stokes equation and also has inherent thermal fluctuations [91, 92] resembling real fluids. By this method a variety of hydrodynamic problems have been solved, for example, swimming of sperm cells [93], African Trypanosome [96], E. coli [97], Taylor line [98], Spheroidal micro-swimmer [99], Squirmer [94, 95] etc. This is the method of our choice as it is very easy to implement and is also one of the most efficient methods in the Stokes limit [102].

We know that the dynamics of the one-armed swimmer is described by the non-dimensional hyper diffusion equation given by Wiggins et al. [79, 80]. They have already shown that a flexible slender filament is propelled by periodic actuation which is characterized by a dimensionless number called the Sperm number S_p [79]. Sperm number is the ratio of the length of the swimmer to its hydrodynamic penetration length. When $S_p \ll 1$, the penetration length is larger than the length of the swimmer, which means that the arms of the swimmer are stiff and perform nearly reciprocal motion and that's why we get very small velocity. When $S_p \gg 1$, we have the length of the swimmer to be very large compared to the penetration length, and hence the drag forces acting on the swimmer increase. Thus the velocity of the swimmer again reduces. The interplay between these two effects leads to a maxima in the velocity at a point when the hydrodynamics penetration length is approximately equal to the length of the swimmer as shown by Wiggins et al. [80, 79].

In section 3.2.1, we have described the model of our two-dimensional swimmer using bead spring and bending potentials. In section 3.1, we have also described the particle based simulation technique MPC and also explained how we couple the swimmer

with the solvent particles to properly resolve hydrodynamic interactions. In section 4.2, we discuss how our one-hinge swimmer breaks time inversion symmetry with flexible arms. Then we analyze the flow field created by a flexible one-hinge swimmer. We also study the velocity of the swimmer as a function of bending potential, frequency of actuation and amplitude of the actuating wave. We are able to define the dimensionless Sperm number for this swimmer and also discuss how our dimensionless velocity vary with respect to S_p . In section 4.3, we discuss how this artificial swimmer can be realized experimentally, followed by the conclusions in section 4.4.

4.2 Results

4.2.1 Breakdown of the time inversion symmetry

From the Scallop theorem we know that the movement undergoing time reversal symmetry will not be able to propel in a low Reynolds number fluid. In the present work we simulate a two-dimensional one-hinge swimmer similar to a two-dimensional scallop. Figure 4.1(a) shows the shape conformation when we have flexible arms and figure 4.1(b) is when we have the rigid arms, for one complete cycle. The curvature of the hinge undergoes a change as $\sin^2(2\pi\nu t)$ which means we have only positive cycles. In figure 4.1(a), when we look from right to left, first half of the figure, (till the solid black line), $\sin^2(2\pi\nu t)$ changes from 0 – 1, shows the closing of the arms and the second half shows the opening of the arms with $\sin^2(2\pi\nu t)$ changing from 1 – 0. The curvature of the hinge changes as a function of time ($\alpha = A \sin^2(2\pi\nu t)$) as given in the equation 3.10. When $t = 0$ we have zero curvature, that means arms of the swimmer is open to maximum possible extent or we start from a straight line. As time progresses, α increases and the arms of the swimmer start to close from the center of the swimmer, similar to a two-dimensional scallop. When the arms start to close, the center of mass of the swimmer moves in the backward direction. The rest of the arms follow the actuation of the hinge points. As the actuation only happens on the hinge, there will be a delay for the actuation to reach the end of the arms. This will cause the points near to the hinge of the swimmer to close faster as compared to the points farther away. So as the arms close, the ends bend in an outward direction and resembles V shaped conformation. When it reaches $\sin^2(2\pi\nu t) = 1$, we get a maximum value of curvature equal to the amplitude A . After

that the curvature at the hinge starts decreasing and the arms of the swimmer start to open up. Again the point away from the hinge will be moving in the closing direction, due to the delay in the propagation of the actuation. By that time the points close to the hinge would have already started to move in the opening direction. Due to this the ends of the swimmer now bend inward as can be observed in the latter half of the figure 4.1(a). The center of mass of the swimmer also starts moving in the forward direction and the ends of the arms start to retract now in a U shape conformation. At a later time, when the arms reach $\sin^2(2\pi\nu t) = 0$ or $\alpha = 0$, the arms of the swimmer open to maximum possible extent. As the swimmer has a V shape conformation during closing of the arms, while in case of opening it has a U shaped conformation, thus breaking the time inversion symmetry and the one-hinge swimmer move ballistically from right to left as shown by the black arrow in figure 4.1, which was also predicted by E. Lauga [19].

In our simulation when we keep the bending stiffness $K_b = 10^7$, we obtain rigid arms for one-hinge swimmer. In the case of rigid arms, the oscillations at the hinge are followed by every point of the arms and thus the swimmer performs reciprocal motion. There is no difference in the opening and closing conformation as can be observed in figure 4.1(b). As a consequence the center of the mass of the swimmer does not undergo ballistic motion.

4.2.2 Mean square displacement

Finite size effect

In problems involving hydrodynamics effect, the simulation box has to be chosen appropriately to avoid finite size effect [93, 138]. To verify the effect of finite box size we have calculated the mean square displacement of the center of mass (MSD) of the rigid arm swimmer

$$\langle \mathbf{R}^2 \rangle = \langle (\mathbf{r}_{cm}(t) - \mathbf{r}_{cm}(t_0))^2 \rangle. \quad (4.1)$$

Where $\mathbf{r}_{cm}(t_0)$ and $\mathbf{r}_{cm}(t)$ are the position of the center of mass of the swimmer at beginning of the simulation $t = 0$ and at time t respectively. In figure 4.2, we have plotted the MSD as a function of time t for a swimmer with length of one arm $L = 15$ for 4 different box sizes. The rigid arms scallop will not be able to break time inversion

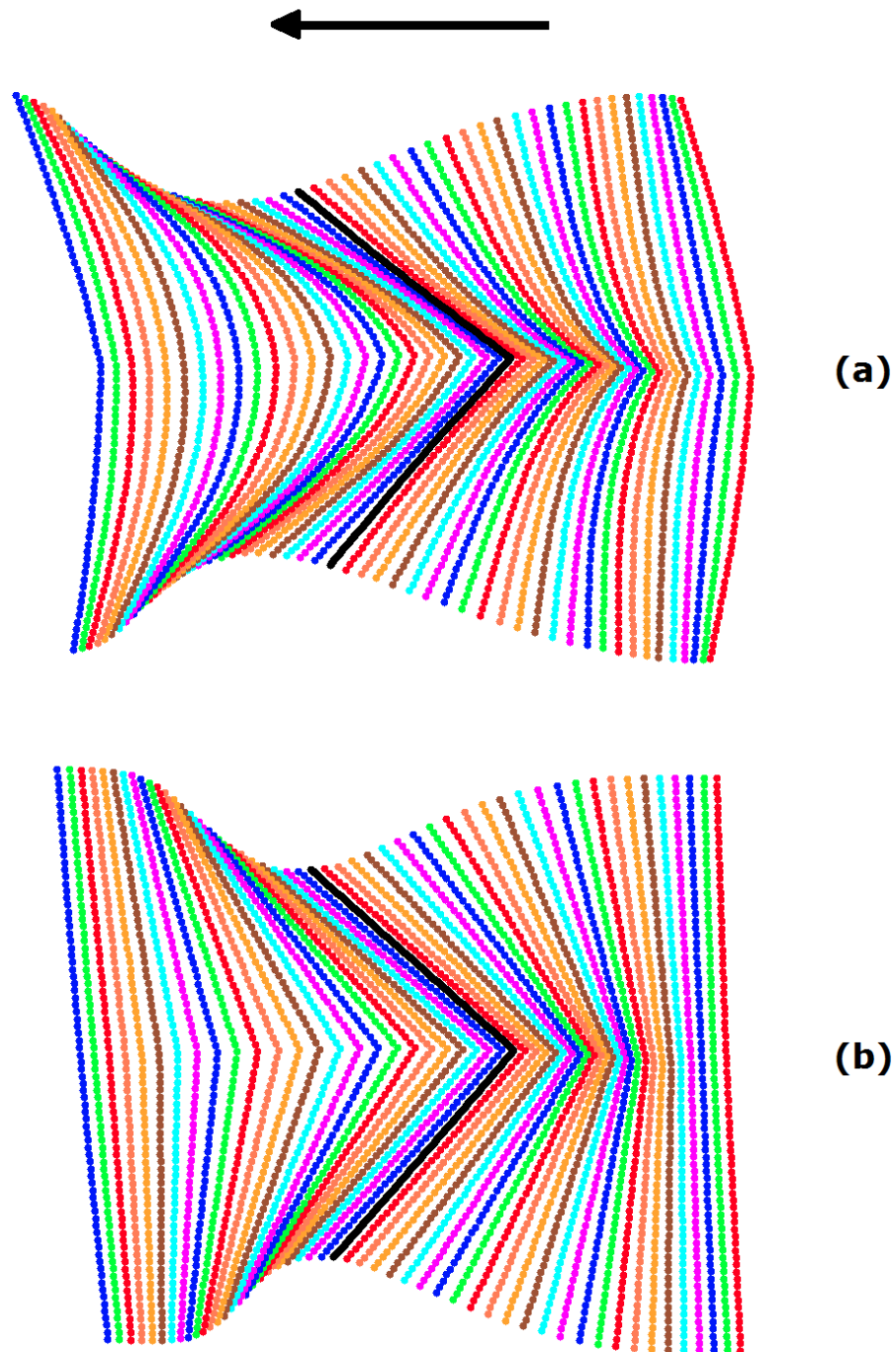


Fig. 4.1 Sequence of conformation of the arms (here different colors are used just for the better visualization) of the one-hinged swimmer over one complete beat cycle, (a) represents the case for a flexible arms and (b) for the case of rigid arms. From right to left, we observe the sequence of closing, from the center bold conformation shows the opening of the arms of the swimmer. The black arrow at the top shows the direction of swimming for the flexible swimmer.

symmetry. So it only diffuses and we expect slope of 1 of MSD due to the inherent thermal fluctuation of the MPC fluid. In figure 4.2, we can see that in all the cases till $t \approx 10$ the swimmer hardly moves because bending waves take some time to propagate from hinge to the end of the arms. As we have discussed in the previous section, initially a swimmer has open arms and with time it starts to close the arms and due to that the center of mass displaces and we get an upswing in MSD. Once the curvature reaches the maximum, arms starts to open again and center of the mass tries to come back to the previous position and due to that we get a down swing in MSD. So the MSD of the swimmer always oscillates depending on the frequency of oscillation. Here, we consider the beating frequency $\nu = 0.01$ and as we are using a curvature $\alpha = A \sin^2(2\pi\nu t)$, so at $t = 1/\nu = 100$ we get two positive cycles that means swimmer completes two cycles of oscillation by closing and opening the arms. This we can observe in figure 4.2. The center of mass oscillates two times till $t = 100$. We observe that when the box size is 60 or 4 times the length of the arm L , after 1 – 2 cycles of oscillation MSD attains slope of 1. When the MSD reaches a time of $t > 300$, we observe a deviation from the slope of 1. When the size of the box was increased to 90 or 6 times of L , we observe that the deviation of MSD from slope of 1 happens at a later time $t > 10^3$ indicating that the finite size effect happens at a much later time. When we further increased the size to 8 and 10 times the length of the arm of the swimmer, we did not observe a deviation from a slope of 1 upto the time of our observation. So in the present work we have always kept the size of the simulation box 10 times the length of the arm of the swimmer to avoid finite size effect.

Ballistic motion

In order to observe the difference between a flexible and a rigid scallop we have calculated the MSD as a function of time for both the cases as shown in figure 4.3. As mentioned before, for the rigid arms the center of mass of the swimmer undergoes diffusive motion characterized by $\langle \mathbf{R}^2 \rangle \propto \mathbf{t}$. In case of flexible arms, we observe that after 3 – 4 cycles of oscillation, the swimmer starts to undergo ballistic motion characterized by $\langle \mathbf{R}^2 \rangle \propto \mathbf{t}^2$ as expected because in this case the time inversion symmetry is broken. The flexible swimmer moves toward the left as indicated by the arrow in the figure 4.1(a) which is also predicted by Lauga et. al [19]. Here for both the cases we have used the

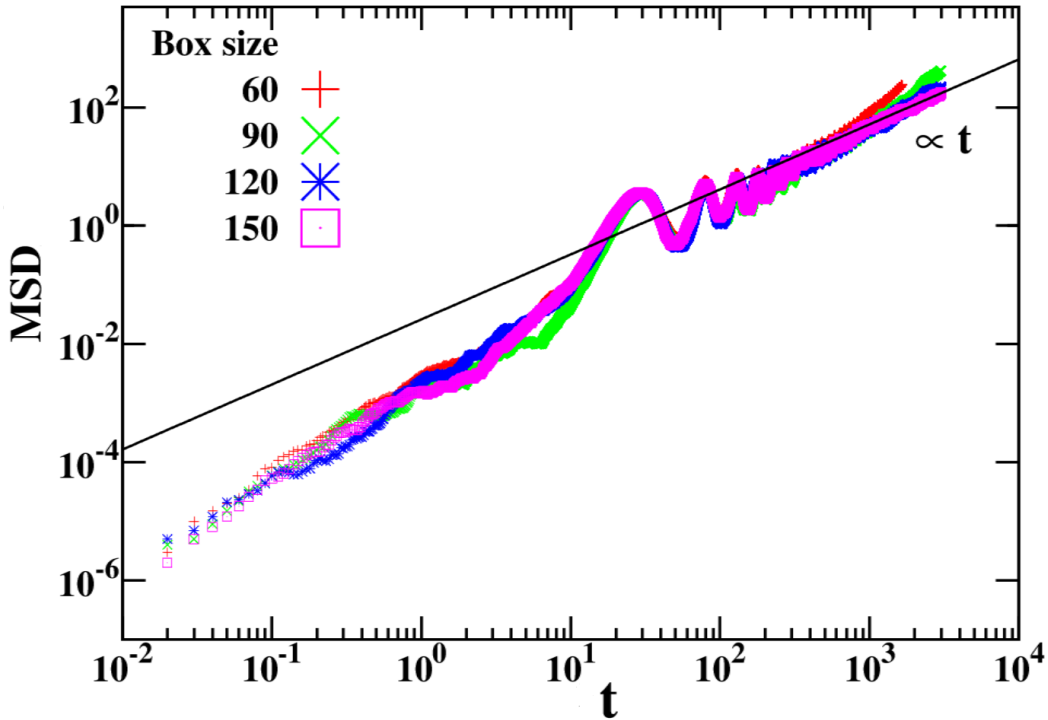


Fig. 4.2 MSD of a rigid scallop of arm length $L = 15$ in four different boxes (box sizes are mentioned in figure). Here solid black line has slope one.

same beating frequency $\nu = 0.01$ and due to that MSD oscillates twice as time reaches $t = 100$.

4.2.3 Flow field

To check that what kind of flow field a flexible swimmer creates in the surrounding fluid, we calculate the average velocity vectors in the vicinity of the swimmer. In figure 4.4, we depict the velocity vectors or flow field around the swimmer. The scale bar shows the strength of the velocity vector where the orange color denotes the smallest magnitude velocity vector and blue color denotes the highest magnitude velocity vector. In the flow profile we can see two curls. When a flexible swimmer opens and closes its arms it creates these two curls. Thus the left arm of the swimmer creates an anticlockwise flow curl and the right arm creates a clockwise flow curl. In the figure, we can see that for both the arms the velocity vectors that have the maximum strength are in the upward direction. So the flow curls push the swimmer in the upward direction as expected from the previous observations. The depicted flow field of the one-hinge swimmer is somewhat similar to

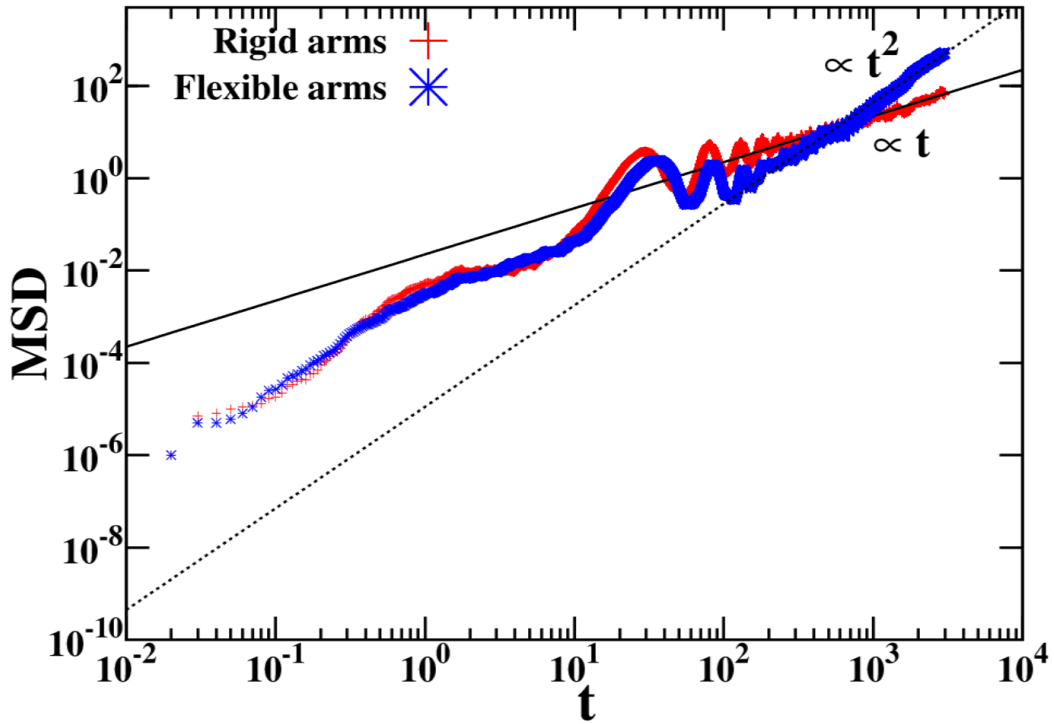


Fig. 4.3 Mean square displacement of the center of mass position of the swimmer is plotted as a function of time t for the flexible arms (blue) and rigid arms (red). The solid line has slope of 1 indicating diffusive motion and dotted line has slope of 2 representing directed motion of the swimmer.

the average flow field of the *Chlamydomonas reinhardtii* and also it follows the same direction of motion [139].

4.2.4 Effect of Flexibility

From the previous sections, we know in the present work flexibility plays a major role in the swimming of the two arms swimmer. To study the effect of flexibility we measure the reduced velocity after the swimmer has attained ballistic motion which is defined as $V_{cm}/L\nu$, where $V_{cm} = \sqrt{\langle R^2 \rangle}/t$. The Reynolds number is defined $Re = V_{max}L/\mu$ [10, 93, 133]. We use $\mu = 3.6$ and the maximum velocity we have studied for the scallop is $V_{max} \approx 0.03$, the length of the arm of the scallop is $L = 20$, so the Reynolds number of our system $Re < 0.16$ is consistent with the previous studies of low Reynolds number regime using MPC simulations [93, 98, 140]. The Peclet number is defined as $Pe = V_{cm}L/D$, where D is the diffusion coefficient of the rigid swimmer [133] and in our case the range of $Pe = 16-80$, which means the thermal fluctuations do not play a significant role in our simulations [141]. In MPC simulation the Mach number of the

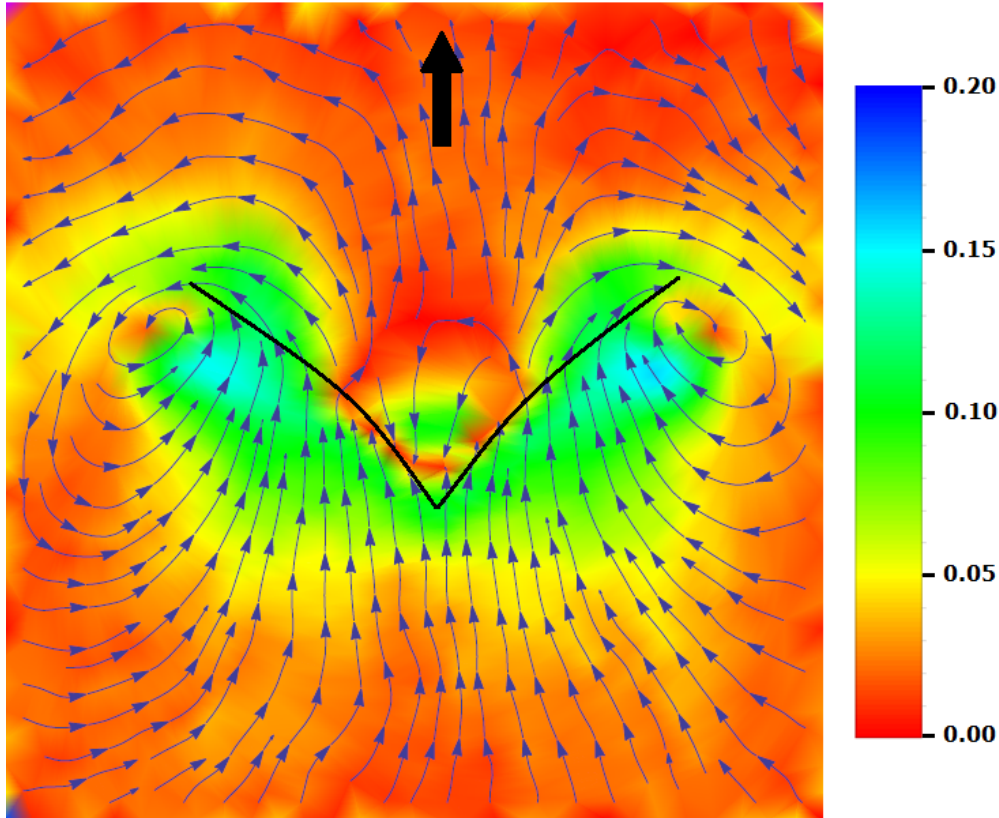


Fig. 4.4 Flow field created by a flexible one-hinge swimmer (thin black line). Here, solid black arrow shows the direction of the swimming.

fluid should be very small in order for the fluid to be incompressible. The Mach number is defined as $Ma = V_{max}/V_{sound}$, here $V_{sound} = \sqrt{2}$ is the speed of sound in 2 dimension for MPC fluid. In our case, for maximum frequency we have used $V_{max} \approx 0.03$ and so $Ma \approx 0.021$ [138], which is within the incompressible limit of MPC. In order to verify that MPC fluid is in the incompressible limit at all length scales in our simulation, we calculated the mach number for the tip of the swimmer which moves with the maximum velocity ≈ 0.42 . The mach number for the tip of the arm turns out to be $Ma \approx 0.30$, which is again within the accepted MPC limit for having an incompressible fluid [113, 133, 142]. In figure 4.5, we have plotted the reduced velocity as a function of bending rigidity K_b of the arms of the swimmer. When $K_b = 0$ and $K_w = 0$ our swimmer becomes passive and behaves as a Gaussian polymer chain. When we increase K_b from 10^5 onward, keeping $K_w = 4 \times 10^5$, we observe a nominal increment in speed. The reason being that here the arms of the swimmer are very flexible and the wave which passes from the hinge is damped before reaching the end point. Here the configurations of the swimmer do not change appreciably during the entire beat cycle. The arms of the swimmer become

progressively rigid by increasing K_b and the speed increases as shown in figure 4.5. Here we have a competition between the elastic forces of the swimmer and viscous drag because of the fluid particles. The speed starts to increase till it reaches a maximum when the elastic forces cancel the frictional forces, for intermediate bending stiffness $K_b = 3.25 \times 10^5$. On further increasing the rigidity of the arms, the velocity goes down. Near $K_b = 10^7$ it starts behaving as a conventional scallop and eventually the speed of the scallop goes towards zero as we keep on increasing the rigidity of the arms.

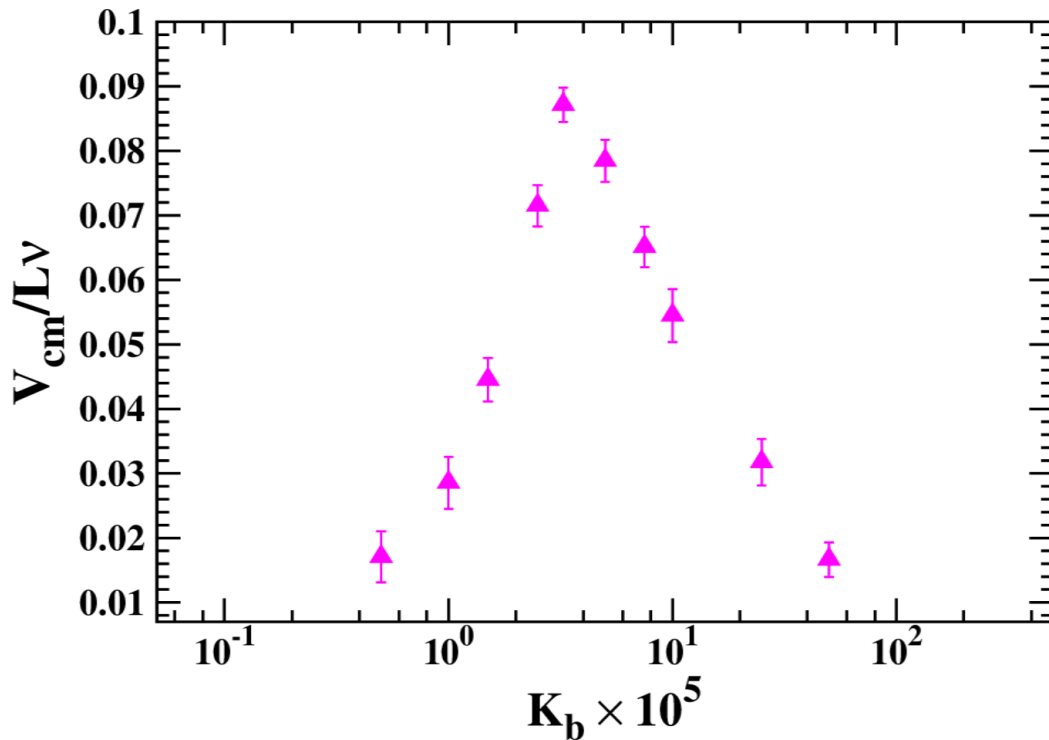


Fig. 4.5 The reduced velocity of the swimmer is plotted as a function of bending rigidity of the arms of the swimmer.

4.2.5 Beating frequency

In figure 4.6, we have plotted the reduced velocity of the swimmer with respect to the beating frequency ν imparted on the hinge. Here the minimum frequency we have used is $\nu = 0.008$ and maximum frequency is $\nu = 0.0175$, so that the swimmer completes 48 and 105 cycles respectively for a time $t = 3000$. In the present study of the one hinge swimmer, we are considering only large amplitudes, and the reduced velocity scales linearly with ν as shown by the straight dashed line in the figure 4.6 which has slope of 1. For a single-armed swimmer Wiggins et al. had derived the equation for velocity

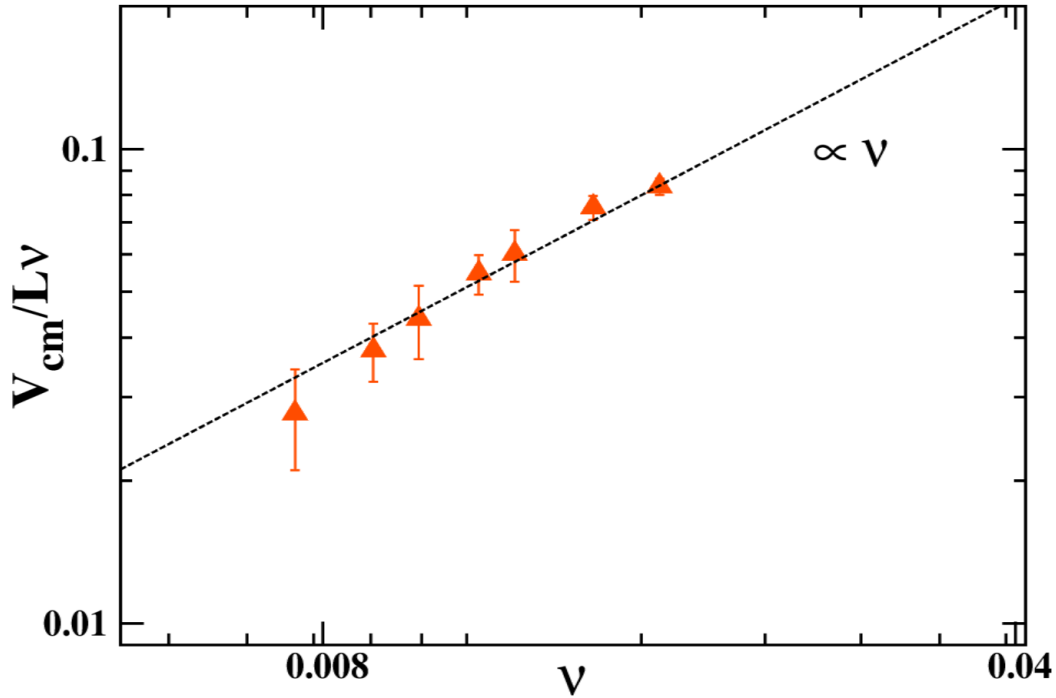


Fig. 4.6 The reduced velocity is plotted as a function of frequency of the actuation. The solid line has slope of one as predicted for the small amplitude approximation.

using small amplitude approximation, where it was shown that the reduced velocity scales linearly with ν . In our case, the amplitude we have considered $A = 4.25$ is large. Still we observe that the scaling is in agreement with that of Wiggins et al. [79].

4.2.6 Amplitude of the actuation

For closing and opening of the arms of the swimmer, the parameter that we are changing is the amplitude A of the bending wave given in the equation 3.10. The amplitude is chosen in such a way whereby we make sure that the mass points of the swimmer close to the hinge will never overlap. As we change the amplitude of the beating, the angle φ created between the arms of the swimmer changes as well, see figure 3.9. The maximum angle between the arms in the simulation nearly stays around $\varphi_{max} = \pi$, while the minimum angle varies between $\varphi_{min} = \pi/3 - 2\pi/3$. In the present study the amplitude is related to the difference in the minimum and maximum angle made by the arms of the swimmer. In figure 4.7, we plot the amplitude A as a function of $\Delta\varphi = \varphi_{max} - \varphi_{min}$, which is the difference between the minimum and maximum angle during the opening and closing of the arms of the swimmer.

When $\Delta\varphi = \pi$, then the maximum angle will be π and the minimum angle will be 0 between the arms of the swimmer, which means the arms of the swimmer is going to overlap at the minimum angle. For measuring φ , we calculate a unit vector between the hinge and the fourth bead from the hinge for the left arm \hat{p}_l and the right arms \hat{p}_r respectively. Then the angle $\varphi = \cos^{-1}(\hat{p}_l \cdot \hat{p}_r)$. Also note that for the beating of the arms we are changing the spontaneous curvature of the beads close to the hinge by $\sin^2(2\pi\nu t)$, which means the angle between the arms will not go beyond π . The dashed line in figure 4.7 is drawn from straight line equation which shows that $A \propto \Delta\varphi$. In the present work we have kept $K_w \approx 10^5$ and found that arms can open and close in such a way $\Delta\varphi > \pi/3$.

In figure 4.8, we plot the reduced velocity as a function of the $\Delta\varphi$. Here we observe that as the difference in the angle between the arms increases, the speed of the swimmer also increases. We observe that the reduced velocity scales as the square of $\Delta\varphi$, the dashed line in the inset of figure 4.8 has slope of two. The equation for the velocity has been deduced from the small amplitude approximation for the single-armed swimmer [79] as well as for the one-hinge swimmer [19]. In these works they had shown that the reduced velocity scales with the square of the amplitude of the actuation. Even though our amplitudes are larger than that were considered in these work, we observe that the reduced velocities have similar kind of scaling as that of small amplitude approximation. We were not able to further increase the amplitude of the actuation as it will lead to overlap of the arms of the swimmer, which is not a physical scenario for an artificial swimmer.

4.2.7 Sperm number

Wiggins et al. had shown that if a flexible rod is perturbed at one end by $y_0 \cos \omega t$, for small amplitudes, the dynamics of the one arm follows the dimensionless hyper diffusion equation $\frac{dy}{dt} = S_p^4 \frac{d^4 y}{dx^4}$, where S_p is a dimensionless number called Sperm number. The Sperm number is given by

$$S_p = L \left(\frac{\xi_{\perp} 2\pi\nu}{k} \right)^{\frac{1}{4}}. \quad (4.2)$$

Where L is the length of the arms of the swimmer, $k = K_b l_0$ is stiffness of the arms of the swimmer, ν is the frequency and ξ_{\perp} is the frictional coefficient per unit length in perpendicular direction of motion defined to be consistent with the one-armed swimmer.

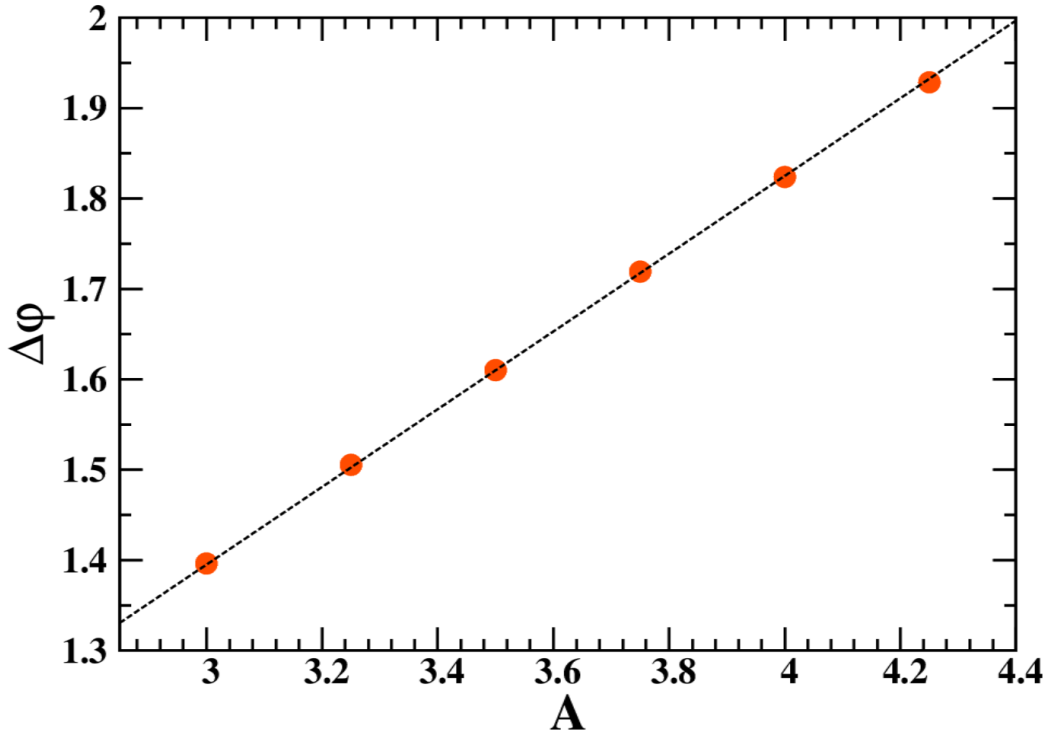


Fig. 4.7 $\Delta\phi$ (in radian) is plotted as a function of the amplitude of actuation. The dashed line shows the linear fit given by $(0.43A/a_0 + 0.1)$.

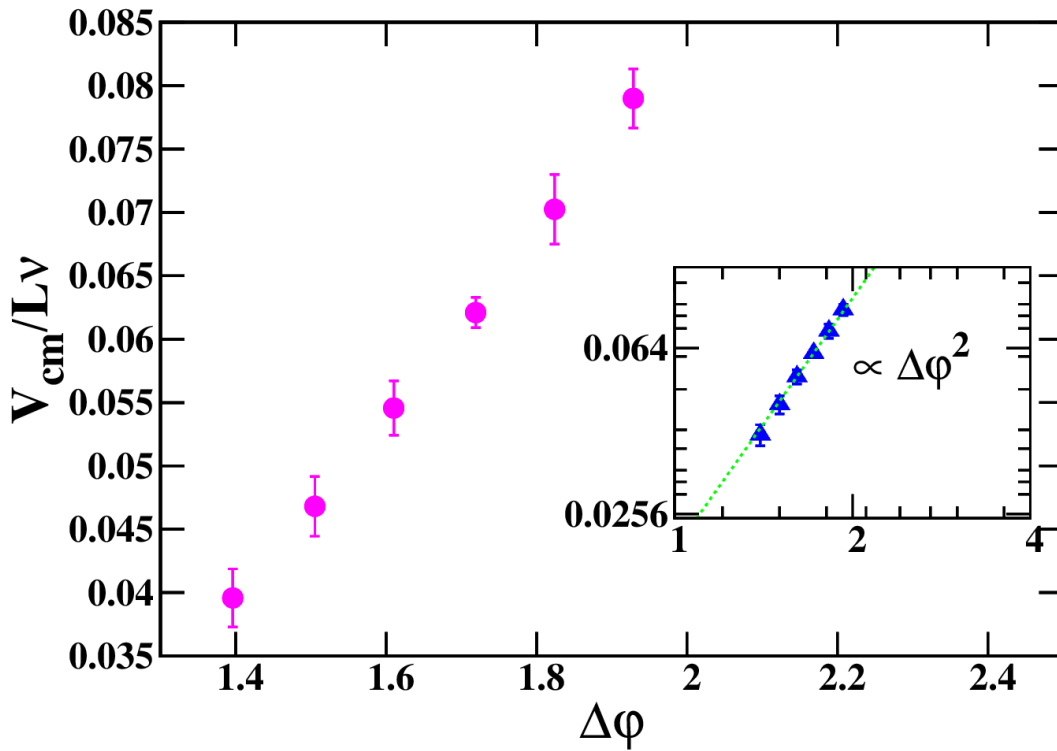


Fig. 4.8 Reduced velocity of the swimmer is plotted as a function of $\Delta\phi$ (in radian), the dashed line (inset) has slope of two as predicted for small amplitude approximation.

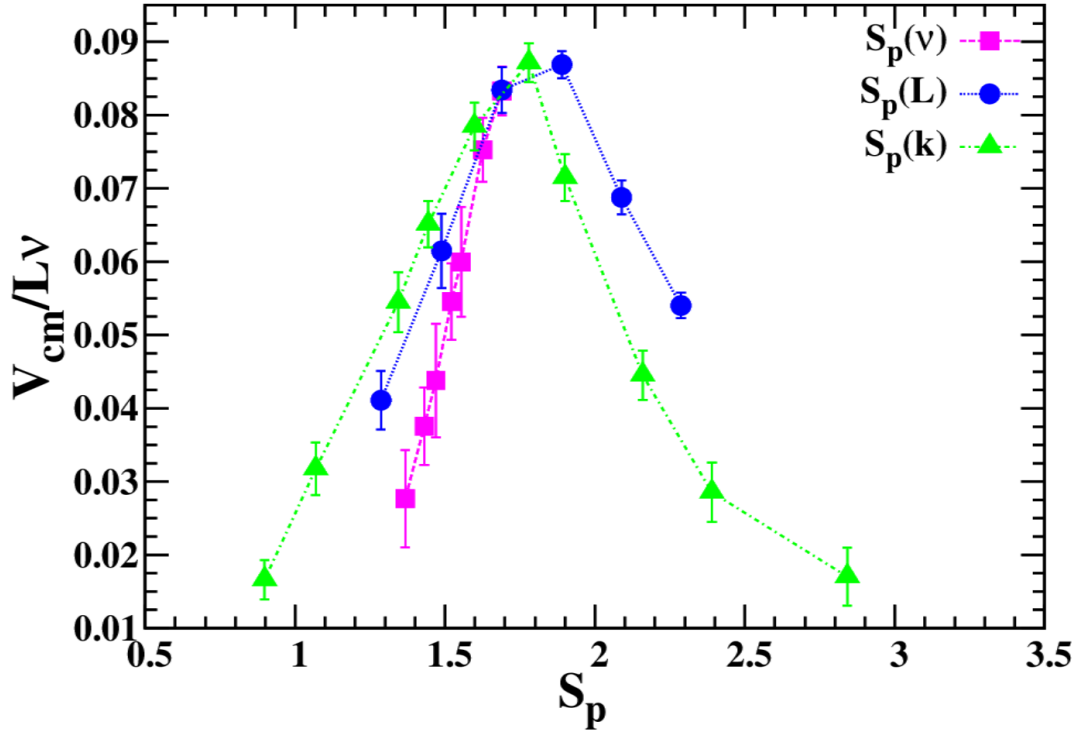


Fig. 4.9 The reduced velocity of the swimmer is plotted as a function of Sperm number. The value of S_p was varied by changing ν (square), L (circle) and k (triangle), keeping all other parameters same.

In the present study, we calculate the perpendicular friction coefficient using $\xi_{\perp} = 4\pi\eta/[\ln(L/r) + 1/2]$ [13], where η is the viscosity of the fluid and r is the radius of the arm. In the present work, the spring that connects two beads behaves as a rigid rod of length $l_0 = 0.5$, as a result we have considered the radius of the rod to be $r = 0.25$. In figure 4.9, we show the reduced velocity of the swimmer as a function of the Sperm number. For the small value of the S_p we observe that the elastic forces dominate and we get a small velocity, while in the high Sperm number region the drag forces acting on the arms of the swimmer dominate and again the velocity goes down. As there is a competition between the viscous and elastic forces in the arms of the swimmer, there should be one particular S_p value where we should observe a maximum for the velocity, which is around ~ 1.8 in our case.

For the one-armed swimmer with small amplitude approximation, it was shown that the maximum velocity is when $S_p \approx 4$, while Lagomarsino et al. have demonstrated using simulations that for the same one-armed swimmer with large amplitude, the maximum velocity happens when $S_p \approx 2$ [83, 84]. This is similar to our present work, where we

consider the amplitude larger than the small amplitude approximation. In figure 4.9, S_p is varied by changing the length of the arms, the frequency of actuation and the stiffness K_b of the arms of the swimmer, keeping rest of the parameters constant of the equation 4.2. Here we can see that the peak positions of the reduced velocities remain almost same. For small values of the Sperm number till $S_p < 1.6$, we find continuous increment in scaled velocity with S_p as expected. After the maximum, we observe that the scaled velocity continuously decreases as we increases the S_p and after $S_p > 2$ we observe a slow drop in scaled velocity. For small amplitude approximation Wiggins et al. had shown that the scaled velocity attains a plateau for higher S_p value. Our results are similar to the results obtained by Lagomarsino et al. [83], where they showed that for large values of S_p , when large amplitudes are considered, the velocity does not stay constant, it slowly decreases with S_p .

4.3 Discussion

It was shown that the one-armed flexible swimmer [11, 15] will undergo ballistic motion only if a passive head is attached to the arm. The two-armed swimmer with a head was initially considered by Lauga [19]. For simplification of the calculation he ignored the hydrodynamic interactions between the arms of the swimmer and also the velocity of the swimmer was derived under the infinitely small amplitude approximation. Lauga has also shown analytically that if two arms are actuated similar to a one-armed swimmer, a passive head is not required to break the time inversion symmetry. In the present work, we are able to show that if two filaments are joined by a hinge and actuated only at the hinge, the artificial swimmer starts to behave as a self propelled object. We obtain the direction of the swimmer as predicted by Lauga [19], but the magnitude of velocity is not in agreement with our work. This may be because in the present work there are hydrodynamic interactions between the arms of the swimmer as well as the amplitude of the actuation in the present work is higher than that considered for the small amplitude approximation. E. Lauga et al. neglected the long range hydrodynamic interactions between the two arms of the swimmer [19], while MPC includes the long range hydrodynamic interactions. The biflagellate algae *Chlamydomonas* is one biological model which is similar to our model. The two flagella show precise phase synchrony

in the breaststroke beating [143]. Similarly in our model, the long range hydrodynamic interaction provides the synchronized behavior between two filaments. Because in our case both the filaments undulate with the same frequency and provide phase locking between two filaments which reduces rotational motion of the swimmer. Hence it ensures straight swimming trajectory. In our simulation, due to the long range hydrodynamics, we have found that swimmer always has a nearly straight swimming trajectory. Due to the absence of a passive, head we believe that the scallop swimmer will be more efficient than the single arm swimmer.

Also recently Tian Quie et al. [144] demonstrated that a micro scallop can swim in a non-Newtonian fluid. In this work they have used a rigid arm scallop in a non-Newtonian fluid, while in the present work our scallop or one-hinge swimmer have flexible arms thereby performing the ballistic motion even in Newtonian fluid. It is known that swimmer African Trypanosome velocity is increased approximately 8 times when it swims in a fluid (non-Newtonian) having obstacles of size and spacing of RBC in blood [145] and it will be interesting to study the swimming of the one hinge swimmer in these environments.

Recently Haug et al. have shown that they can create soft robotic materials using light actuated materials [18]. The light-driven liquid-crystal (LDLC) material [90], which are sensitive to ultra-violet light, can convert light into mechanical energy with quick response and large deformation. When we shine UV light the LDLC undergoes a phase transition by which it gets converted into a shorter molecule, while shining visible light it recovers its original conformation. We believe using these materials experimental realization of the one-hinge swimmer is possible. They have already demonstrated using these materials that they are able to recover the shape conformation for a one-armed swimmer and to extend it to a one-hinge swimmer should not be too challenging.

4.4 Conclusions

In this chapter, we have modeled a two-dimensional scallop or a one-hinge swimmer. We have shown that the hydrodynamic interactions between the mass points of the swimmer and the fluid particles can be simulated using multi-particle collision dynamics (MPC). We have also demonstrated that if the arms of swimmer are very rigid, it follows

the Scallop theorem and the swimmer is not able to propel itself through the viscous fluid. But when the arms are made flexible, the time inversion symmetry is broken and swimmer performs ballistic motion. For a flexible swimmer, we have shown the velocity flow profile. We have also shown that the velocity of the swimmer has a maximum for intermediate bending rigidity along the arms of the swimmer. For small bending rigidity, the arms are very flexible and the actuation is not able to produce the desired shape conformations, while for stiff arms we are closer to the Scallop theorem and the velocity approaches to zero. The reduced velocity is also studied as a function of frequency as well as the amplitude of actuation and we have shown a similar scaling relation as predicted by elastohydrodynamic within the small amplitude approximation, even though we have considered large amplitude in the present work. We were also able to define Sperm number for the swimmer and have also shown that the reduced velocity had a maximum at $S_p \sim 1.8$ which is consistent with what is expected for large amplitude actuation.

Chapter 5

An exploration of one-hinge self-propelled swimmer in stokes flow

In the present study, we are exploring the two dimensional one-hinge swimmer in a Newtonian fluid. Here we will show that the arrangements of the bending rigidity along the arms of the swimmer change the properties or the dynamics of the swimmer. To model the one-hinge swimmer, we have use bead-spring model and the fluid is simulated using a technique known as multi-particle collision dynamics with Anderson thermostat. Here, we show that when our swimmer has asymmetric arms, then instead of straight path, it follows the circular path. The direction of the circular pattern depends upon the combination of the bending rigidity of both the arms. Here we obtain the swimming trajectories, rotation rate for a few combinations of bending rigidity. When one of the arms is pretty rigid and second has moderate rigidity, then this combination creates maximum rotation rate and the swimming trajectory has larger curvature. As we increase the amplitude of actuation the rate of rotation also increases. Here, we also consider a non-uniform distribution of the bending rigidity K_b along the arms, where we have progressively changed the K_b in a geometric sequence and show that this arrangement can enhance the swimming speed.

5.1 Introduction

Locomotion at the micron-scale encounters entirely different kind of challenges as compared to macro-scale swimming. Micron-scale swimmers experience viscous drag much stronger as compared to the inertial forces. In order to get a single external force free low Reynolds number swimmer motile in an infinite Newtonian fluid, swimmer must follow the non-reciprocal movements as stated in Purcell's famous Scallop theorem [10, 81]. Natural biological micro-swimmers generally break the Scallop theorem by waving their flagella [51], oaring flexible cilia [146] and by rotating helical flagellum [25, 26]. Inspired by natural swimmers, many artificial small scale swimmers have been constructed to exploit identical swimming strategies. For example, para-magnetic flexible micro-swimmer attached with red blood cell, [15], light sensitive soft robotic swimmer [18], cardiomyocytes cultured polydimethylsiloxane film swimmer [17], magnetic multilink nanoswimmers [54], fish-like nanoswimmers [55] and magnetically driven helical shaped micro-robots [147, 148]. Other than this, many theoretical artificial models have also been proposed like Taylor sheet [63], three-spheres swimmer with a passive elastic arm [67], elastic two-sphere swimmer [68] and one-hinge flexible swimmer [149] etc. These further assist us to design more controlled artificial swimmers and also help us in more precise fabrication as well as to improve the performance of previously built swimmers.

In theoretical flexible models, the prototypical example is a single flexible filament swimmer [19, 79, 83, 84]. Later E. Lauga has shown that swimming using multiple flexible filaments provides straight swimming trajectories, which is the advantage over single filament swimmer and head is also not required to break the time-inversion symmetry [19]. Additionally, B. J. Williams et al. have also given the experimental evidence that a bio-hybrid two tailed swimmer can achieve much higher speed as compared to simple one head and one tail swimmer [17]. In chapter 4 of this thesis, we have demonstrated a computational model of one-hinge swimmer, where we have optimized the parameters that results maximum velocity using dimensionless Sperm number [79]. To obtain the diverse functionality of one-hinge flexible swimmer, we carry this study to the next step. In the present chapter, we consider a bit sophisticated arrangement of bending rigidity of the arms of the one-hinge swimmer which provide us an enhanced swimming speed and also give us control over the direction of the swimmer. Similar to previous work, to design

the one-hinge flexible swimmer we have used bead-spring model (see section 3.2.1) and to simulate the solvent we have used the particles based simulation method known as multi-particle collision dynamics (MPC) [102] (see section 3.1). The benefits of MPC are that it provides the solution of the Navier-Stokes equation and also has inherent thermal fluctuations [91, 92] similar to the real fluids.

The chapter is arranged as follows. In section 5.2, we have discussed the results where we have demonstrated how the dynamics of the swimmer changes by adding a disparity in the bending rigidity of the arms. Also we have compared our results with similar experimental observation. In section 5.3 we have concluded our results.

5.2 Results and discussion

A one-hinge swimmer can perfectly swim in a viscous fluid if it has flexible arms as shown in chapter 4, where we have considered a one-hinge swimmer with symmetric arms and uniform bending rigidity along the arms as shown in figure 5.1(a). The bending rigidity is the parameter that makes the one-hinge swimmer mobile. To make the swimmer more controlled and efficient, we consider an assorted arrangement of the bending rigidity of the arms.

5.2.1 Constant but asymmetric rigidity

Initially we consider a swimmer which has asymmetric arms. By asymmetry we mean that both the arms have different bending rigidity. As discussed in section 3.2.1, we can control bending rigidity by changing the value of K_b . In the case of asymmetric swimmer, we label the arms as arm_l (left arm) & arm_r (right arm), and their bending rigidity as $K_b = K_{b_l}$ & $K_b = K_{b_r}$ respectively as shown in figure 5.1(b).

There are many possible combinations that we can choose. For example, arm_l is pretty flexible & arm_r is moderately flexible, or arm_l is pretty rigid & arm_r is pretty flexible and many more. We know that the slender body swimmers that move by waving their flagellum, propel in the opposite direction to the direction of bending wave propagation [56]. In case of one-hinge swimmer, for every combination of rigidity, the body of the

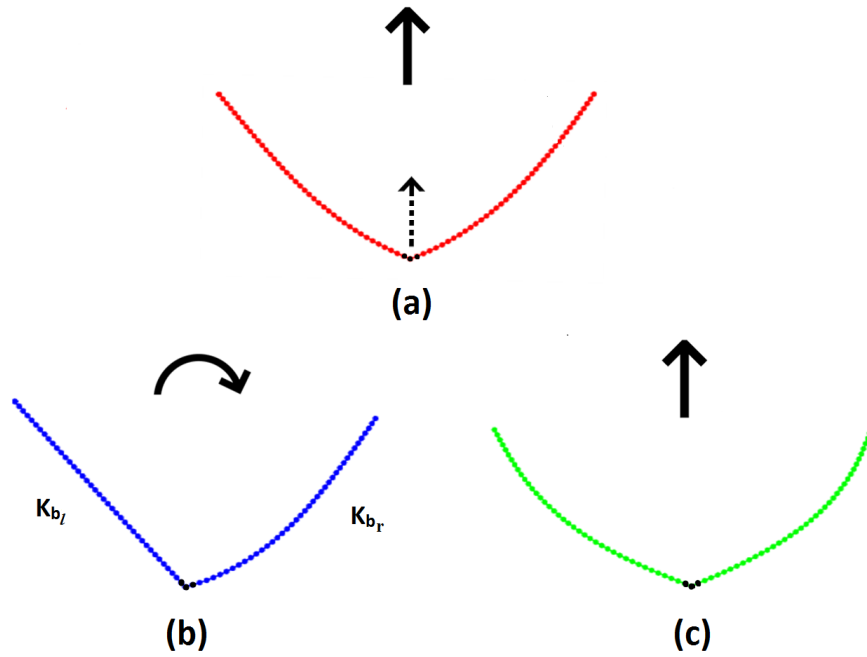


Fig. 5.1 Schematic of one-hinge swimmer. (a) Both the arms of the swimmer are symmetric and have uniform bending rigidity. (b) Arms are not symmetric. Left arm has bending rigidity K_{b_l} and right has K_{b_r} , though the bending rigidity K_{b_l} & K_{b_r} along the arms are uniformly distributed. (c) Arms are symmetric but bending rigidity along the arms is non-uniform. Bending rigidity is arranged in such a way that it reduces from hinge to edge in a geometric sequence. We can see that near the edges, arms (green) are pretty flexible as compared to the symmetric uniform arms (red), though in both the cases average bending rigidity is same. Three beads are given black color to show that the bending wave potential U_w is applied only on these three beads. The black solid arrow shows the direction of the motion.

swimmer deforms in a different manner. So swimmer may follow different swimming direction. This is because the direction of bending wave propagation depends upon the pattern or shape that swimmer will follow. We can refer this by comparing two experimentally observed swimmers. R. Dreyfus et al. proposed a magnetic flexible swimmer containing a red blood cell (RBC) as a head and a tail made up of magnetic colloidal particles [15]. An applied magnetic field induces beating pattern that propels the swimmer. The RBC head moves toward the free end of the tail which indicates that a wave is passing from free extremity towards head [15]. B. J. Williams et al. proposed a bio-hybrid synthetic swimmer having a head part and a tail part actuated by the heart muscles [17]. The contraction-relaxation of heart muscles provide a beating pattern and contrary to previous swimmer, it moves towards to the head. This is because they seeded the heart muscles only at the joint area of the head & tail. Due to that the swimmer

deforms in such a way that a wave travels from head to tail. As a consequence swimmer moves from free end of the tail to head. This bio-hybrid swimmer body attains different kind of configurations as compared to the paramagnetic swimmer. Hence it follows the opposite direction of motion [15, 17], though both have one head and one tail.

In the present work, we are employing a bending wave potential which induces the bending wave that propagates through the arms of the swimmer. In the beginning of the simulation, the swimmer is in form of a linear chain of beads and as we apply the bending wave potential (U_w) the arms of the swimmer start to close and open. The curvature $\alpha = A \sin^2(2\pi\nu t)$ ensures that the arms of the swimmer will open & close in only upper half portion, similar to the scallop [149]. Due to the asymmetric arms, we expect that swimmer will also have rotational motion. Because of the rotation, it will be a little bit tricky to observe the direction of bending wave propagation. If somehow we can eliminate the rotation, it will simplify the observation of the direction of linear motion as well as the direction of the wave propagation. So we have used the curvature $\alpha = A \sin(2\pi\nu t)$ instead of the earlier one. This curvature ensures that arms will open & close in the upper half region as well as in the lower half region, which will switch off the rotation. To demonstrate the direction of bending wave propagation, we consider three key bending rigidities which make arm_l; (a) extremely stiff ($K_{b_l} = 10^7$), (b) very flexible ($K_{b_l} = 5 \times 10^4$) and (c) moderate flexible ($K_{b_l} = 3 \times 10^5$), while arm_r always has moderate flexibility. (Note that the values of bending rigidity have been chosen on the basis of the study of the one-hinge symmetric swimmer. In chapter 4, we have shown the values of K_b which makes the arms of the swimmer extremely rigid, extremely flexible and moderate flexible.) In these three cases, we get different directions of motion as can be seen in figure 5.2. When arm_l is extremely rigid, then only arm_r contributes in the motion. In figure 5.2(a), if we see from top to bottom, we find that the swimmer is propelling towards the arm_l. It means a wave is passing from hinge towards arm_r. Next, we keep arm_l pretty flexible. We expect that here also arm_r will provide motion to the swimmer because it has moderate flexibility. But if we carefully watch the figure 5.2(b) then we see that the large flexibility of arm_l damps down the actuation near the hinge, due to that arm_r seems to be rigid and a wave with a smaller amplitude travels from hinge toward arm_l. Hence swimmer moves toward arm_r with a slower speed. Finally when both the arms have a moderate flexibility, swimmer does not move. It just has diffusive

motion as expected, see figure 5.2 (c). Since it is the case of symmetric arms and the thrust generated here by one arm is exactly opposite to the other arm, so there should not be any propulsion. From this demonstration we can observe that in an asymmetric one-hinge swimmer, the propelling wave passes from hinge towards the free end of the arm which is comparatively less rigid and the entire structure propels toward the more rigid arm.

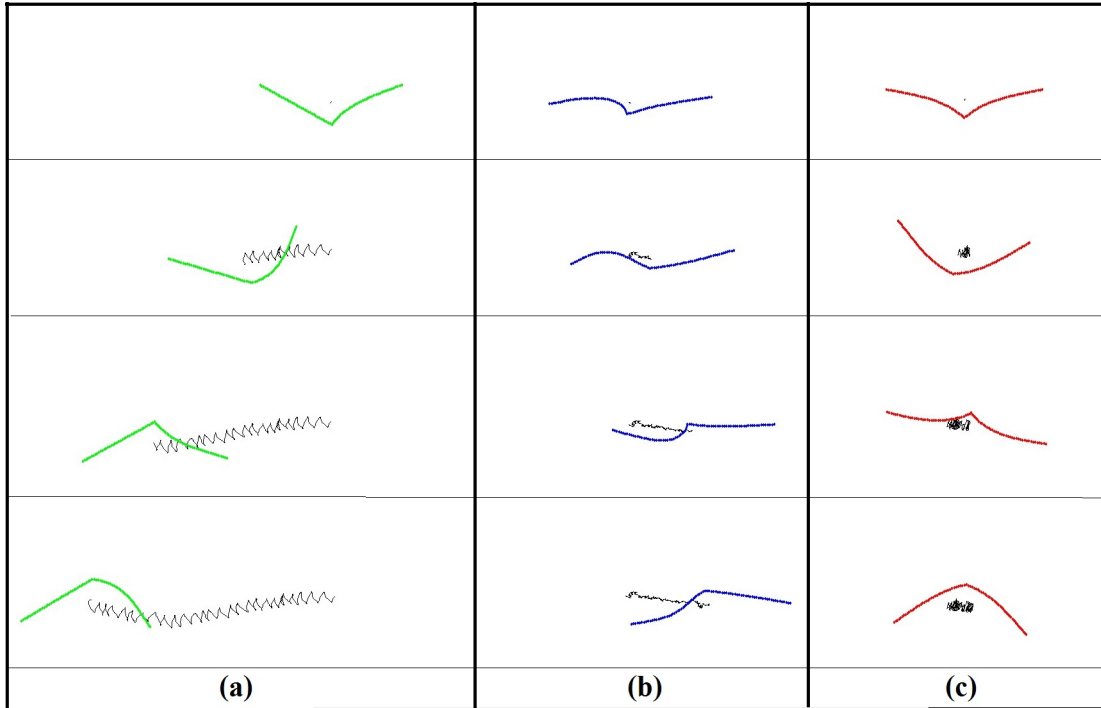


Fig. 5.2 Trajectories of the swimmer for three different cases where the curvature between the arms changes as $\alpha = A \sin(2\pi\nu t)$. (a) $K_{b_l} = 10^7$, $K_{b_r} = 3 \times 10^5$ and swimmer propels toward left arm. (b) $K_{b_l} = 5 \times 10^4$, $K_{b_r} = 3 \times 10^5$ and swimmer propels toward right arm. (c) $K_{b_l} = 3 \times 10^5$, $K_{b_r} = 3 \times 10^5$ and swimmer perform only diffusive motion.

Now let us consider that curvature is $\alpha = A \sin^2(2\pi\nu t)$. That means swimmer performs a scallop kind of movements (arms open & close in only upper half portion). First, we consider that arm_l is rigid and arm_r has moderate flexibility. According to the previous observation, the swimmer should propel towards the arm that is comparatively more rigid and bending wave will travel in the opposite direction. We have considered $K_{b_l} = 10^7$ and $K_{b_r} = 3 \times 10^5$. Since both the arms on an average (average over one complete cycle of opening and closing) make an angle of 120° , so due to the flexibility when the arm_r propel towards hinge, the rigid arm_l tries to resist this motion and in turn

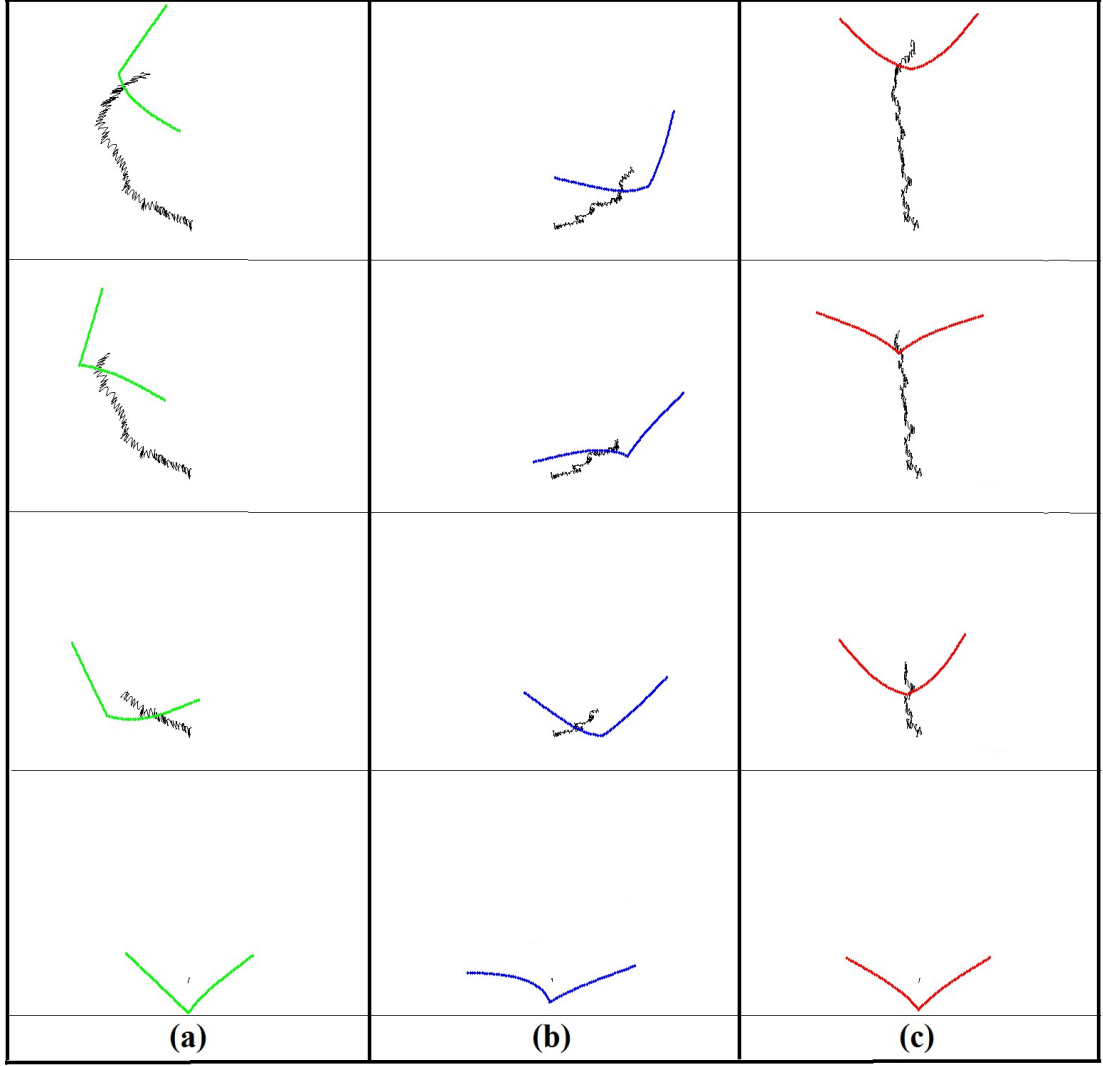


Fig. 5.3 Trajectories of the swimmer for three different cases where the curvature between the arms changes as $\alpha = A \sin^2(2\pi\nu t)$. (a) When $K_{b_l} = 10^7$, $K_{b_r} = 3 \times 10^5$ and swimmer has left hand rotation. (b) When $K_{b_l} = 5 \times 10^4$, $K_{b_r} = 3 \times 10^5$ and swimmer has right hand rotation. (c) When $K_{b_l} = 3 \times 10^5$, $K_{b_r} = 3 \times 10^5$ and swimmer has no rotation, it follow straight swimming trajectory .

the arm_l starts rotating toward arm_r. As the left hand rotation can be observed from figure 5.3(a). To calculate the rate of rotation, we associate a vector \vec{d} with the swimmer as illustrated by the dashed black arrow in figure 5.1(a). For that we introduce two vectors from hinge to both the edges. Let us consider that the vector $\vec{d}_l = -\sum_{n=1}^{(N_b-1)/2} \vec{t}_i$ is associated with arm_l and $\vec{d}_r = \sum_{n=N_b/2}^{N_b-1} \vec{t}_i$ is associated with arm_r, where N_b is the total number of the beads. The normalized vector sum of both these vectors is

$$\vec{d} = \frac{\vec{d}_l + \vec{d}_r}{|\vec{d}_l + \vec{d}_r|}. \quad (5.1)$$

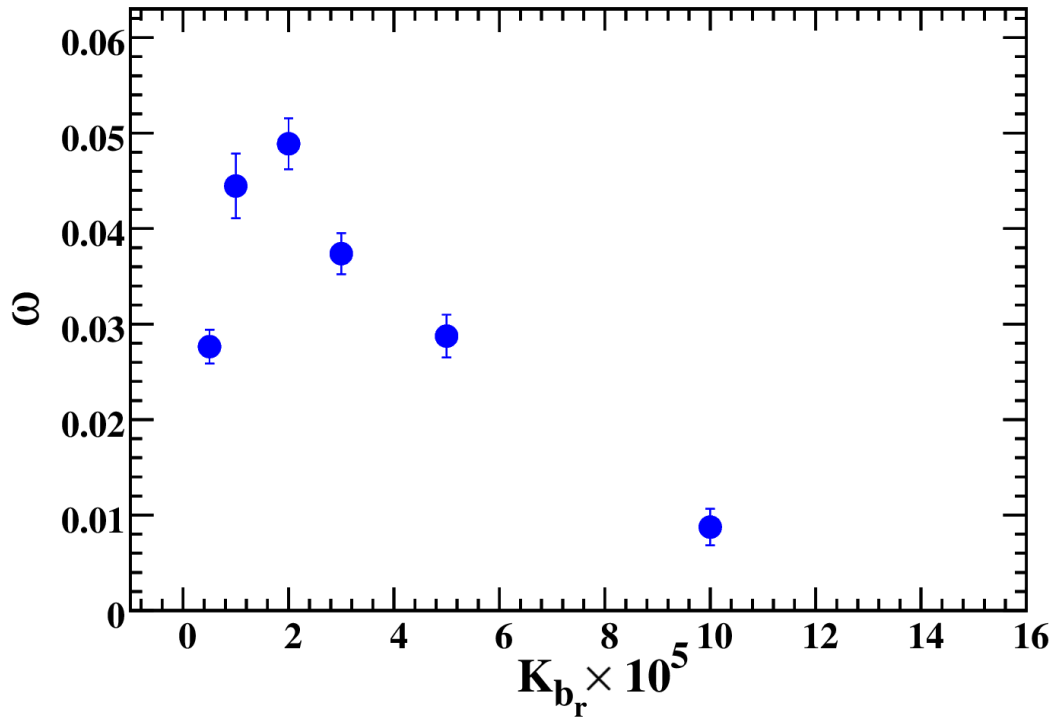


Fig. 5.4 Angular velocity w of an asymmetric swimmer for different values of K_{b_r} , while keeping $K_{b_l} = 10^7$ (extremely stiff). K_{b_l} and K_{b_r} are the bending rigidities of the left arm and right arm respectively.

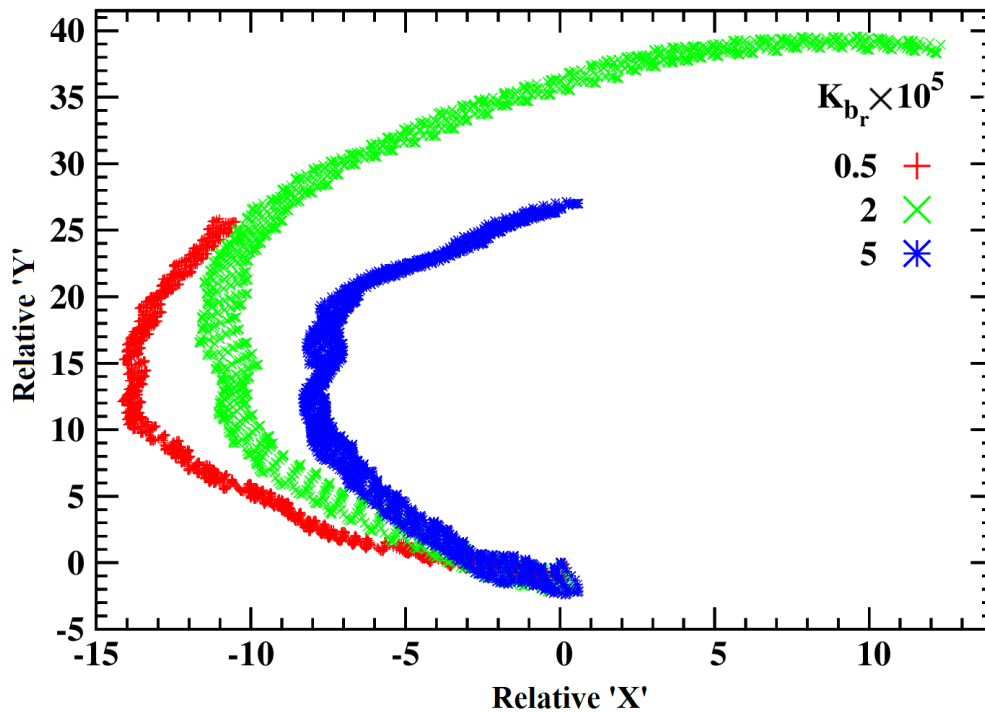


Fig. 5.5 Trajectories of an asymmetric swimmer for three different values of K_{b_r} , while keeping $K_{b_l} = 10^7$. Here K_{b_l} is always greater than K_{b_r} . Due to that swimmer always follows a left circular pattern.

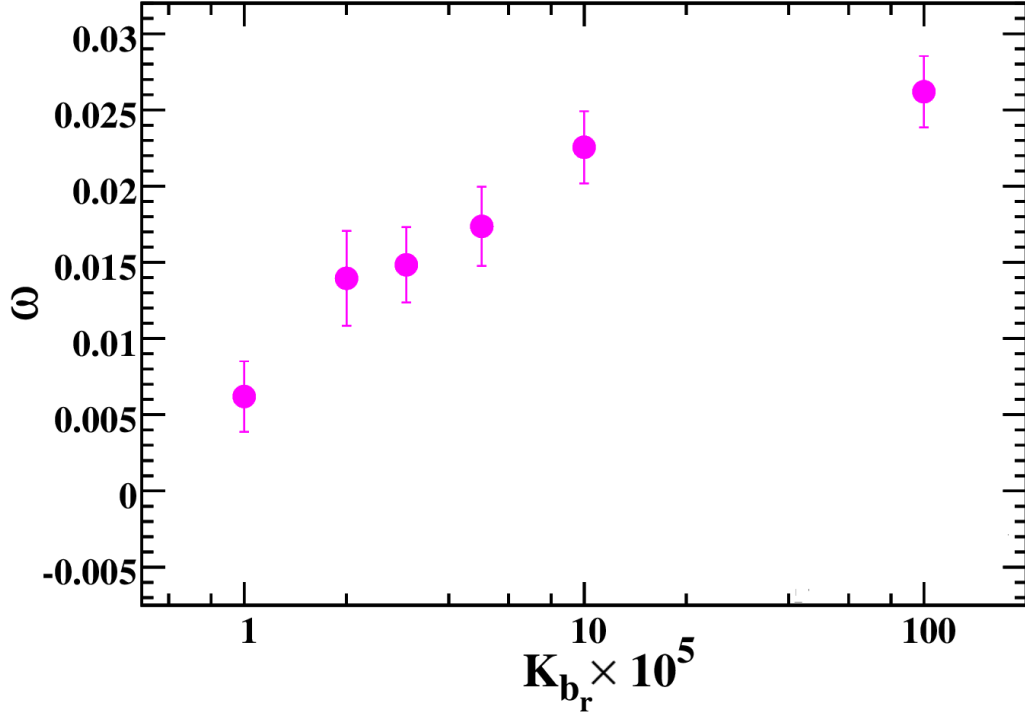


Fig. 5.6 Angular velocity of an asymmetric swimmer for different values of K_{b_r} while keeping $K_{b_l} = 5 \times 10^4$ (very flexible).

If at the beginning of simulation the vector associated with the swimmer is $\vec{d}(t_0)$ and at a later time t it is $\vec{d}(t)$, then the angle of rotation is $\theta_r = \cos^{-1}(\vec{d}(t_0) \cdot \vec{d}(t))$. And when the swimmer attained ballistic motion we measure the angular velocity as $w = \langle \theta_r \rangle / t$.

In the present work, we keep $K_{b_l} = 10^7$ fix and vary the value of K_{b_r} . In figure 5.4, we have plotted the angular velocities w with respect to K_{b_r} . We observe that when K_{b_r} is small, viscous forces dominate and hinge oscillation dies down in the smaller region. Hence we get small value of angular velocity. As we increase K_{b_r} , w also increases and after reaching a maximum value w again starts decreasing. It happens because now arm_r starts becoming rigid and we have already kept arm_l rigid, which means swimmer go towards symmetry, therefore less rotation and hence small angular velocity. If we consider $K_{b_r} = 10^7$, then both the arms will become symmetric and extremely rigid. Hence it will follow the reciprocal motion. So here we do not consider K_{b_r} equal or higher than K_{b_l} .

In figure 5.5, we have plotted the three swimming trajectories for different values of K_{b_r} , where $K_{b_l} = 10^7$. Here $K_{b_l} > K_{b_r}$ which keeps the arm_l always more rigid as

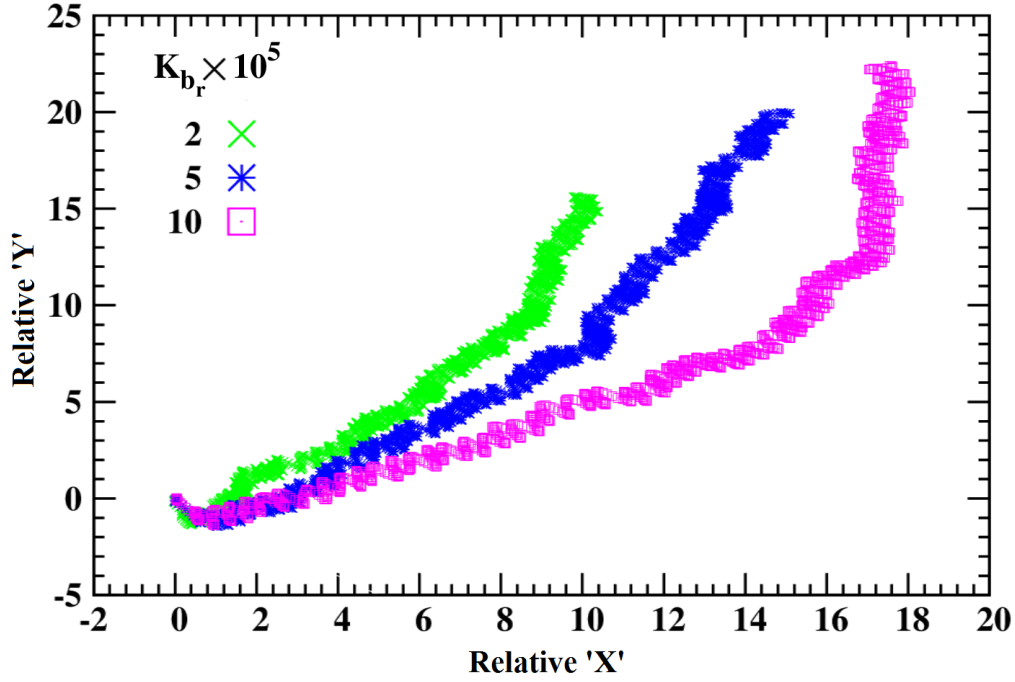


Fig. 5.7 Trajectories of an asymmetric swimmer for different values of K_{b_r} , while keeping $K_{b_l} = 5 \times 10^4$. Here K_{b_r} is always greater than K_{b_l} which results into right circular trajectories.

compared to the arm_r . So swimmer always has left hand rotation as explained before and it can be observed from their trajectories in figure 5.5.

Next we consider arm_l very flexible ($K_{b_l} = 5 \times 10^4$) and vary the rigidity of arm_r , and plot the angular velocity in figure 5.6. It can be observed that as we are increasing K_{b_r} , w is also increasing. This is because we always keep arm_l very flexible and when arm_r is also flexible, swimmer is unable to generate sufficiently large actuation near hinge. Also there is not much difference between the rigidity of both the arms which results in small angular velocity. As we start increasing K_{b_r} , it enhances actuation near the hinge that results into higher angular velocity. In figure 5.7, we have plotted the three swimming trajectories, where value of K_{b_r} is varied and $K_{b_l} = 5 \times 10^4$. Here K_{b_r} is always greater than K_{b_l} . So arm_l propels in the direction of arm_r and arm_r tries to resist this motion and hence the arm_r start rotating toward arm_l . This right hand rotation can be observed from the trajectories in figure 5.7. Note that if we compare the trajectories of the swimmer from figure 5.5 (case (i)) and figure 5.7 (case (ii)), we find that trajectories of case(i) (where $K_{b_l} = 10^7$) have larger curvature as compared to the trajectories of case(ii) (where

$K_{b_l} = 5 \times 10^4$). This is because the average angle between the arms in case(i) & case(ii) are approximately 120° & 135° respectively and larger is the angle lesser is the curvature.

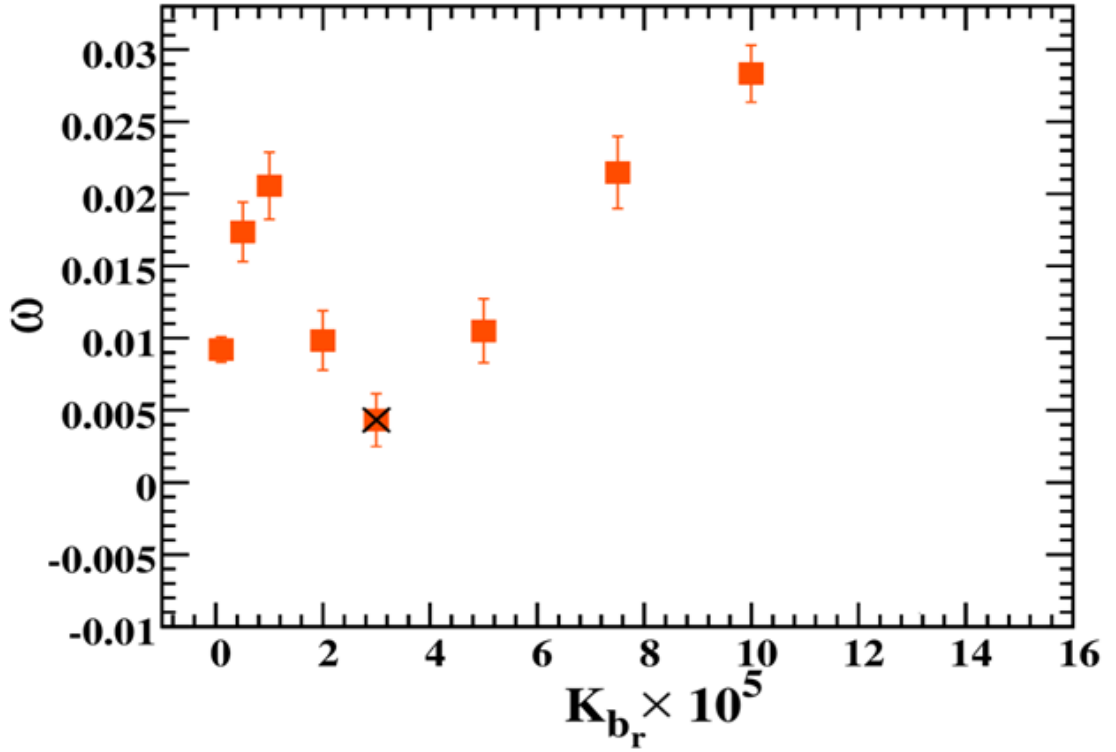


Fig. 5.8 Angular velocity of an asymmetric swimmer for different values of K_{b_r} , while keeping $K_{b_l} = 3 \times 10^5$ (moderate). The black crossed point is used in case of symmetric arms ($K_{b_r} = K_{b_l}$).

Further, we consider arm_l with moderate flexibility $K_{b_l} = 3 \times 10^5$. In figure 5.8, we have drawn the angular velocity with respect to K_{b_r} for the same. We start with a small value of $K_{b_r} = 0.5 \times 10^4$, so swimmer has a smaller angular velocity for that. As we start increasing K_{b_r} , initially angular velocity increases and then it starts decreasing. When $K_{b_r} = K_{b_l} = 3 \times 10^5$, w reaches to its minimum value because due to symmetry there is no rotation. Hence there is very small angular velocity and it is because of thermal fluctuations. If we keep continue increasing K_{b_r} , arm_r becomes more rigid as compared to arm_l and w again starts increasing. Interestingly, here we get a series of maxima and minima. This is because arm_r has moderate flexibility. So we could consider both the possible cases i.e. $K_{b_r} > K_{b_l}$ and $K_{b_r} < K_{b_l}$. Next in figure 5.9, we have shown three swimming trajectories, where we vary the value of K_{b_r} and keep $K_{b_l} = 3 \times 10^5$. When

$K_{b_l} > K_{b_r}$, then swimmer rotates in clockwise direction and when $K_{b_l} < K_{b_r}$, it rotates in anti-clockwise direction as expected. In case of symmetric bending rigidity, we expect no rotation. According to the expectation when $K_{b_l} = K_{b_r}$, we get straight swimming trajectory.

B. J. Williams et al. have experimentally shown that a two-tailed swimmer (some what similar to our swimmer) actuated by the heart muscles creates a curved swimming trajectory [17]. The curved trajectory arises due to a slight asymmetry between two tails, as authors reported that it is due to the right tail which generates more propulsive force as compared to the left tail. In their case, the left tail is slightly rigid as compared to the right. As a result swimmer moves in an anti-clockwise pattern (note that here swimmer is down facing) [17]. Our one-hinge asymmetric swimmer is also showing a similar pattern. The two-tailed swimmer exhibits quite sharp turn. This is due to the large amplitude of the oscillation near the hinge and also there is a disparity in the shape of the tails. Presently, we have studied the three different cases of asymmetry. If we compare the angular velocities of all these three (see figure 5.4, 5.6, 5.8), we find that the swimmer has maximum angular velocity when it has one arm extremely stiff and second arm moderately flexible with Sperm number $S_p \sim 1.8$. Further, for maximum angular velocity configuration, we change the value of amplitude to check whether it affects the angular velocity or not. In figure 5.10, we have plotted the angular velocity with respect to amplitude A of the actuation for the same. In case of a symmetric arm swimmer, linear velocity increases with amplitude A . Similarly in the present case when we increase the value of A , w increases with it as can be seen in the figure 5.10.

5.2.2 Varying but symmetric rigidity

Let us consider initially each arm has N beads (except common bead) and uniform bending rigidity K_b from hinge to edge point. Now we want to progressively change the bending rigidity starting from end point to hinge point of the arm in such a way that the average bending rigidity remains equal to K_b . Also if end point has a bending rigidity K_0 , then hinge point will have bending rigidity equal to $R_{K_b} \times K_0$. Here R_{K_b} is the ratio of bending rigidity at the hinge point to bending rigidity at the edge point

$$R_{K_b} = \frac{(K_b)_{hinge}}{(K_b)_{edge}}. \quad (5.2)$$

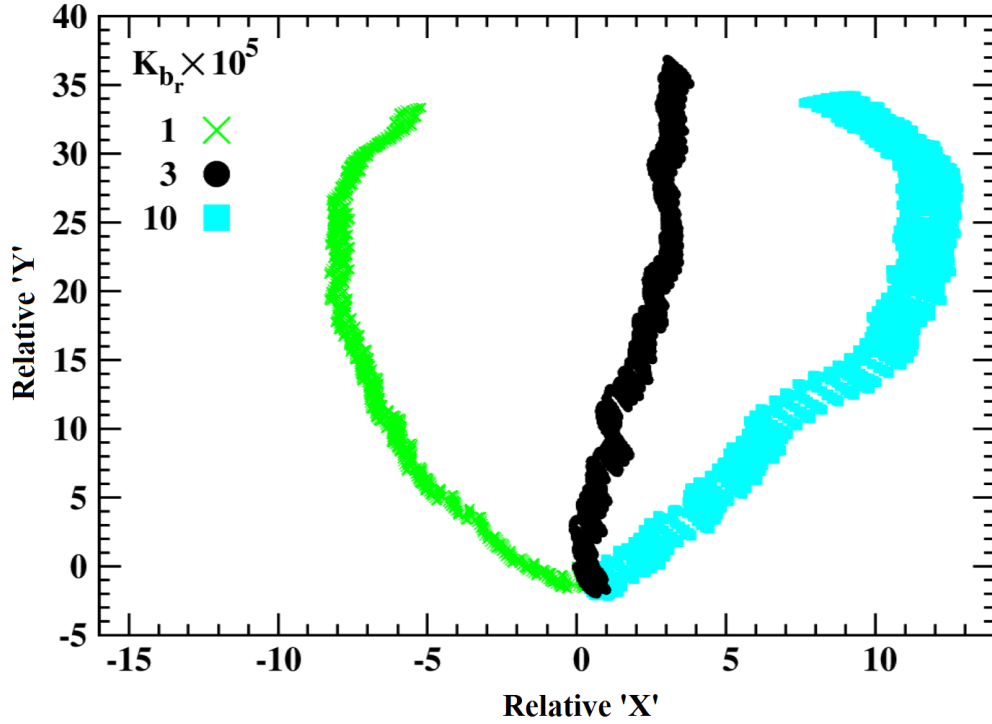


Fig. 5.9 Trajectories of an asymmetric swimmer for different values of K_{br} , while keeping $K_{bl} = 3 \times 10^5$ (moderate). When $K_{bl} > K_{br}$, swimmer follows a left circular pattern and if $K_{br} > K_{bl}$ it moves in a right circular pattern. When $K_{bl} = K_{br}$ (symmetric arms) swimmer goes along a straight path (black).

To progressively change the bending rigidity, we increase the bending rigidity by a factor f in a geometric sequence, f can be considered as common bending rigidity ratio between two consecutive points. The sum of a geometric progression is

$$K_0 \left(\frac{1 - f^N}{1 - f} \right) = NK_b, \quad (5.3)$$

where K_0 is the first term, i.e. the bending rigidity of the edge point. If we fix the value of R_{K_b} then we can calculate f as $f = R_{K_b}^{1/(N-1)}$ and then K_0 as well. So the bending rigidity of the i_{th} bead is $K_0 \times (f)^i$. Here we have taken the different values of R_{K_b} and have analyzed the dynamics of the swimmer. In figure 5.11, we have plotted the scaled velocity $V_{cm}/L\nu$ of the swimmer with respect to R_{K_b} , where V_{cm} is the center of mass velocity of the swimmer. When $R_{K_b} = 1$, it means arms have uniform rigidity. In figure 5.11, if we compare the velocity of the uniform case (indicated by red crossed point) with varying rigidity cases, we can observe that as we increase the ratio R_{K_b} velocity also increases. When we increase R_{K_b} , the arm near the hinge becomes comparatively stiff and as we go towards the edge, arm becomes more and more flexible as can be seen in

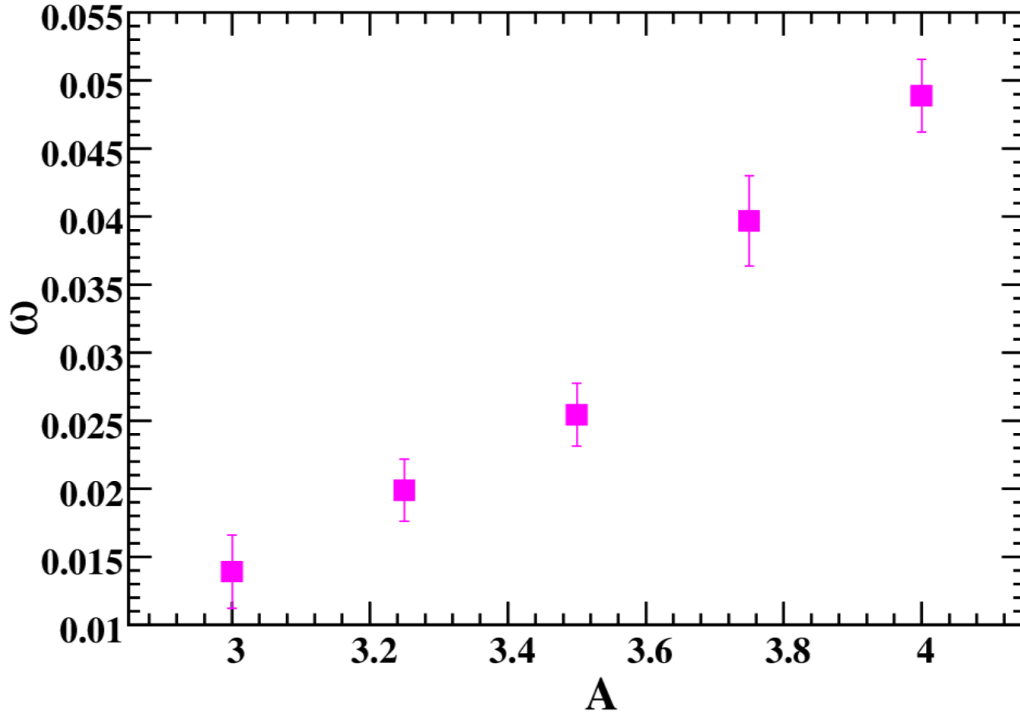


Fig. 5.10 Angular velocity w of an asymmetric swimmer for different values of amplitude A , while keeping all other parameters fixed.

figure 5.1(c). Due to the enhanced flexibility of the edges, the bending wave has larger amplitude here and the stiffness near the hinge contributes to open & close the arms perfectly. Both the facts are favorable to add up the velocity. After a maximum, the velocity starts decreasing. It is because now near the hinge, arm becomes very stiff and towards the edge it becomes very flexible. So the wave damped in a very small region as we progressively increase R_{K_b} .

Further, in figure 5.12, we have plotted the scaled velocity of the swimmer as a function of S_p . Here we have considered two cases; one is the uniform case when the swimmer has symmetric arms with uniform bending rigidity, and second is the non-uniform case when arms are symmetric but bending rigidity of the arms is gradually decreasing, where we have kept $R_{K_b} = 30$. In figure 5.12, if we compare the scaled velocity for both the cases, we can see that near the value of S_p where we get maximum velocity, there is always a hike in the velocity for non-uniform case as compared to uniform case. Now if we go towards high Sperm number, velocity follows the same trend. But if we go towards low S_p , the velocity decreases for non-uniform case as compared to uniform case. This is because in non-uniform case we arrange K_b in a geometric sequence,

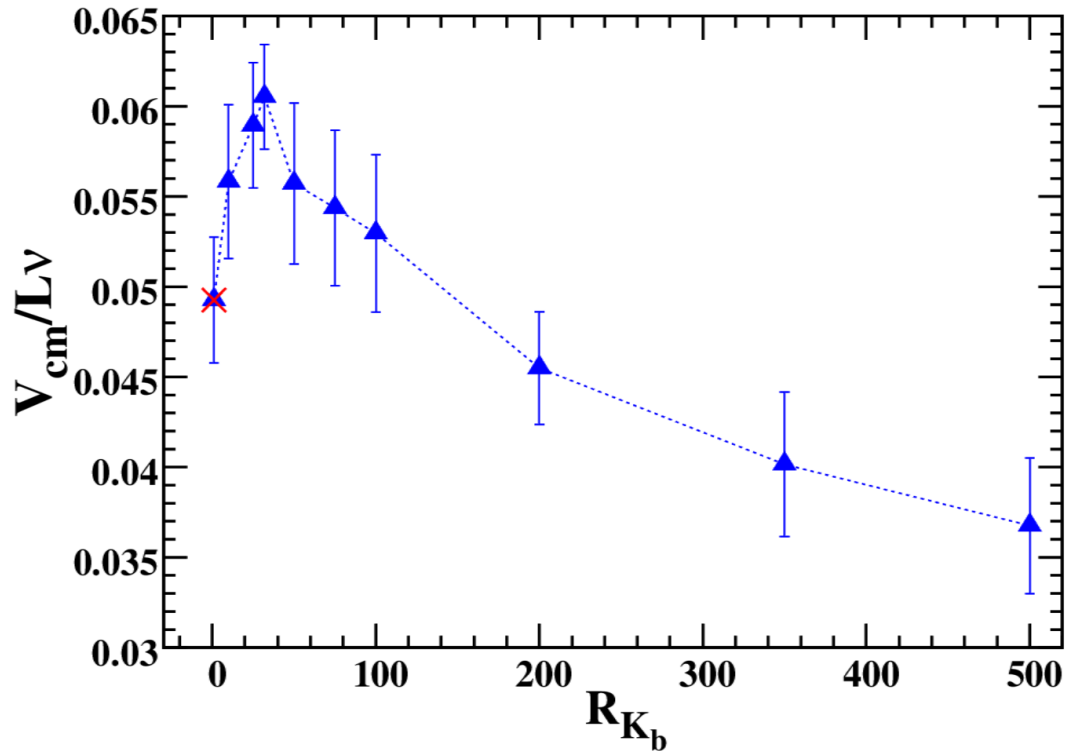


Fig. 5.11 Scaled velocity is plotted as a function of R_{K_b} . R_{K_b} = ratio of bending rigidity at hinge bead to bending rigidity at edge bead. The crossed point is used for the case of uniform bending rigidity.

increasing from tip to hinge while keeping average rigidity equals to the uniform case. We know S_p decreases that means K_b increases and for non-uniform case it is even larger near the hinge. So bending wave suppresses in a very small region that results low velocity as compare to the uniform case. From the above observation, we can conclude that if want to make such a swimmer practical, then we should use such a material for the arms of the swimmer which has gradual increment in flexibility as we move towards the edge. By doing so we can get around 25% increment in velocity.

5.3 Conclusions

In this chapter, we have studied two special cases of a two-dimensional one-hinge swimmer. First, we have considered a swimmer which has arms with asymmetric bending rigidity. We have demonstrated how asymmetry causes circular swimming trajectory and how we can change the direction of motion accordingly. If we keep right arm more rigid as compared to left arm, swimmer moves in a right circular pattern. And opposite to this if left arm is comparatively stiffer, then swimmer follows left circular path. When one

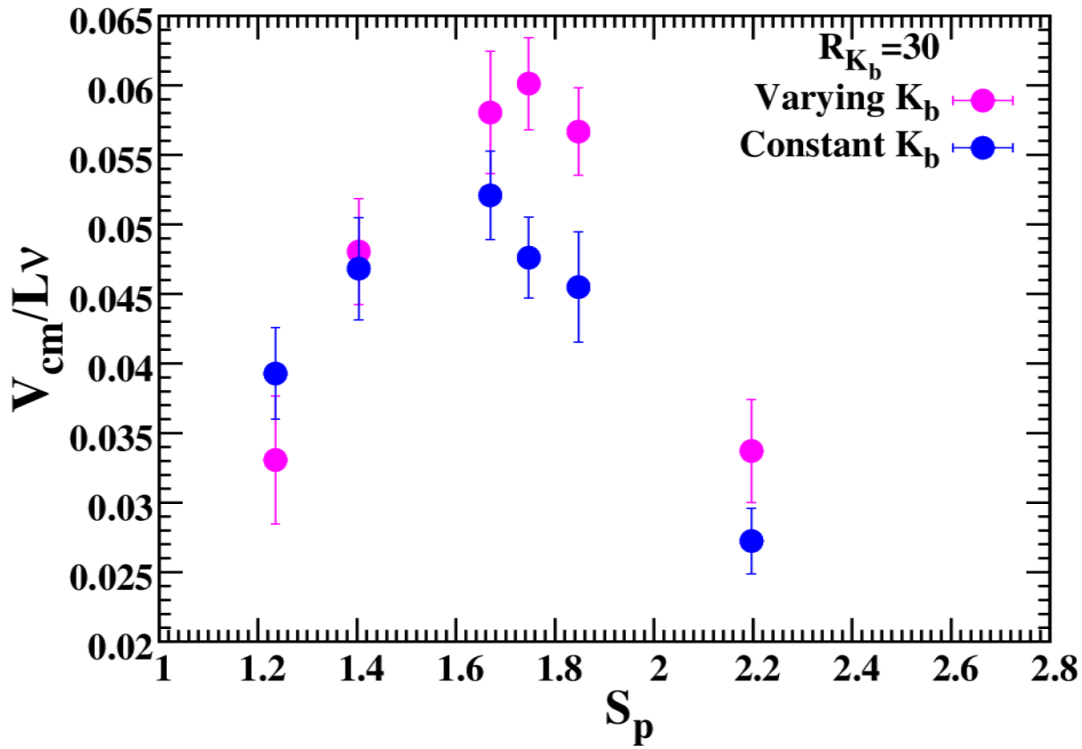


Fig. 5.12 Scaled velocity is plotted as a function of Sperm number. The blue curve and pink curve represent uniform flexibility and varying flexibility along the arms of symmetric swimmer respectively.

arm is extremely rigid and second has moderate rigidity having Sperm number $S_p \sim 1.8$, then this combination produces maximum angular velocity and swimming trajectory has larger curvature as well.

Second, we have considered a non-uniform distribution of the bending rigidity K_b along the arms. Here we have progressively changed K_b in a geometric sequence and found that by doing so (for moderate $S_p \sim 1.8$ value) we can enhance the swimming speed approximately 25%.

Chapter 6

Swimming of a 3-D elastic scallop in a viscous fluid

Locomotion in Newtonian fluids at low Reynolds number is possible only if a body goes through non-reciprocal deformations due to the Scallop theorem. We consider an elastic three dimensional scallop where elasticity of the scallop is within a range, neither too small nor too high. To model the elastic scallop, we have used bead spring model. The fluid is simulated using a multi-particle collision dynamics with Anderson thermostat. Here we show that due to the elastic property, the deformations of a scallop are non-reciprocal. Hence the elastic scallop breaks the time inversion symmetry and propels in Stokes regime. The velocity of the swimmer is studied varying the flexibility and the width of the flaps of the scallop. Our results demonstrate that artificial low Reynolds number swimmers can be designed by exploiting elastic deformations of the body.

6.1 Introduction

Most of the micro-organisms habitat in a fluid environment, where for many of them locomotion is a basic need for survival. Micro-organisms deal with an environment where they have inertial forces that are much weaker than viscous forces. Therefore the ratio of inertial force to viscous forces known as the Reynolds number (Re) is very small for them [56]. In the regime of low Reynolds number, Navier-Stokes equations of flow field

reduce to Stokes equations. And because of the time independence and the linearity of Stokes equations, if an object tries to move by a reciprocal motion it cannot go anywhere. This is the so called Scallop theorem [10].

According to the theory, a micro swimmer can propel in viscous fluid only if it is able to break the Scallop theorem [81]. The Scallop theorem is only acceptable for single swimmer that deforms its body in reciprocal fashion in unbounded static Newtonian fluid and also have no inertia, for details see review paper "Life around the scallop theorem" by Eric Lauga [81]. There are non-Newtonian physical medium [144, 150], hydrodynamic interactions [151], inertia [152] or non reciprocal kinematics [10, 56, 61], all these ingredients can break the Scallop theorem that leads to net non zero propulsion. Many biological micro swimmers make use of non reciprocal kinematics to propel themselves by passing a wave through their cell body, for example E. Coli, Chlamydomonas reinhardtii, Spermatozoa [26, 51, 75] etc. Even the nonreciprocal kinematics has become a key feature in order to make a motile artificial swimmer at the micron scale. The prototypical example is Purcell's two hinge swimmer that goes through the configurations that are non reciprocal under time inversion [10]. Thereafter several artificial model swimmers have been proposed where the non-reciprocal kinematics were used for propulsion. For instance, a simple three-sphere swimmer was proposed by Najafi and Golestanian [64], where the spheres are connected by two slender rods and the joining rods change their configuration in such a way that is not time invariant. To construct the swimmer based on upper mentioned idea one needs atleast two degrees of freedom and there are some simple possible swimmers those have only one degree of freedom, therein flexibility is a simple key feature that can destroy time inversion symmetry as we have shown in case of 2-D one-hinge swimmer in chapter 4 and 5.

The archetypal model of a simple flexible swimmer was proposed by Wiggins et al. [79], where they have shown that a flexible filament which is periodically actuated can break the time inversion symmetry and if the filament is rigid, it will obey the time inversion symmetry. Subsequently, many computational [83, 84, 94], analytical [19, 68] and experimental [15] studies were made on flexible swimmers. A simple swimmer, from where the scallop theorem originated, is a micro scallop itself [10]. Because of a single degree of freedom, a scallop performs reciprocal movements and as a result it cannot

propel in low Reynolds number. Tian et al. have demonstrated that a non-Newtonian fluid can be used to evade the Scallop theorem in case of micro scallop [144]. As we have discussed above that in case of single degree of freedom, flexibility is a crucial ingredient to elude from time reversibility.

Here, we are studying the dynamics of an elastic Scallop in a three dimensional environment and also able to show that elasticity can make a micro scallop to propel in a Newtonian viscous fluid. In section 3.2.2, we have described how we constructed our three dimensional elastic scallop using bead-spring and bending potentials. In section 3.1, we have described the multi-particle collision dynamics (MPC) simulation technique that is used here for fluid environment and section 3.3 explains how we incorporated the elastic scallop with fluid particles to resolve the hydrodynamic interactions.

The chapter is arranged as follows. In section 6.2 we show how an elastic scallop is able to swim in a Newtonian viscous fluid. We also study the velocity of the swimmer as a function of width of the scallop and bending rigidity along the flaps. This is followed by the section 6.3 i.e. conclusions.

6.2 Results and discussion

6.2.1 Enhanced diffusion

We start with a conventional scallop configuration, where we consider bending rigidity $K_{b_L} = K_{b_W} = 10^5$ it makes the flaps of the scallop very stiff. Here K_{b_L} and K_{b_W} are bending rigidity along the length and width of the scallop. We apply the bending wave potential U_w which provides the opening and closing to the flaps. As we are using curvature $\alpha = A \sin^2(2\pi\nu t)$, then during one complete cycle the curvature between the flaps undergoes a change as $\sin^2(2\pi\nu t)$. Here ν is the frequency of opening and closing. In the first half cycle, the scallop closes its flaps and in the second half cycle, it opens the flaps and as time progresses scallop keeps continuing this process. We are working in low Reynolds number regime and simple closing-opening of flaps is reciprocal motion. So this rigid scallop does not propel itself. It goes under diffusive motion with a diffusion coefficient $D \approx 0.004$. If we consider $K_b = K_w = 0$, swimmer behaves as a passive

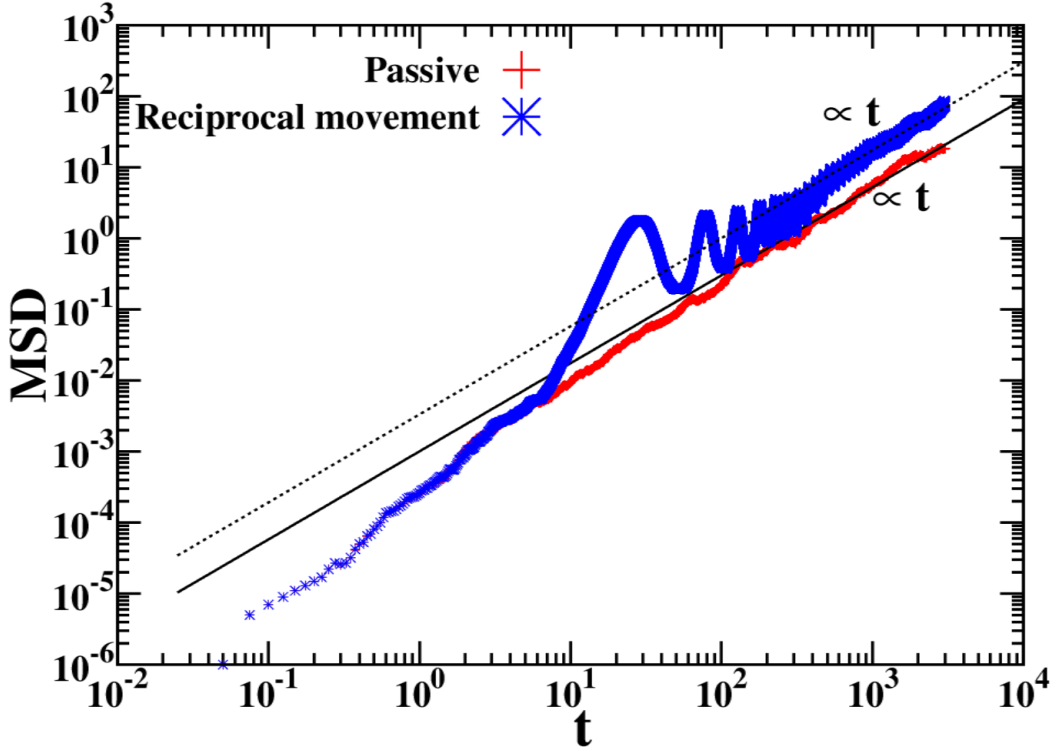


Fig. 6.1 Mean square displacement (MSD) of the center of mass is shown as a function of time t for two different cases. One, where the scallop is opening and closing its shells with reciprocal motion with a diffusion coefficient $D \approx 0.004$ and second, where scallop is passive and only thermal fluctuation is there ($D \approx 0.001$).

sheet and for this we get a diffusion coefficient $D \approx 0.001$. It means reciprocal motion enhances the diffusivity of a scallop [153]. We can see this in figure 6.1, where we have plotted the mean square displacement (MSD) of the center of mass

$$\langle \mathbf{R}^2 \rangle = \langle (\mathbf{r}_{cm}(t) - \mathbf{r}_{cm}(t_0))^2 \rangle. \quad (6.1)$$

Where $\mathbf{r}_{cm}(t_0)$ and $\mathbf{r}_{cm}(t)$ are the position of the center of mass of the swimmer at the beginning of the simulation $t = 0$ and at time t respectively. In case of reciprocal motion (blue), MSD oscillates with time due to the constant opening and closing movements. Here MSD fits with slope of 1 which verify the diffusive motion.

6.2.2 Ballistic motion

We know that flexibility is the ingredient that can break the Scallop theorem. So instead of rigid flaps we consider flexible flaps. For that we reduce the value of K_{bL} , while keeping K_{bW} constant. Due to the flexible flaps, the perturbation that creates on the

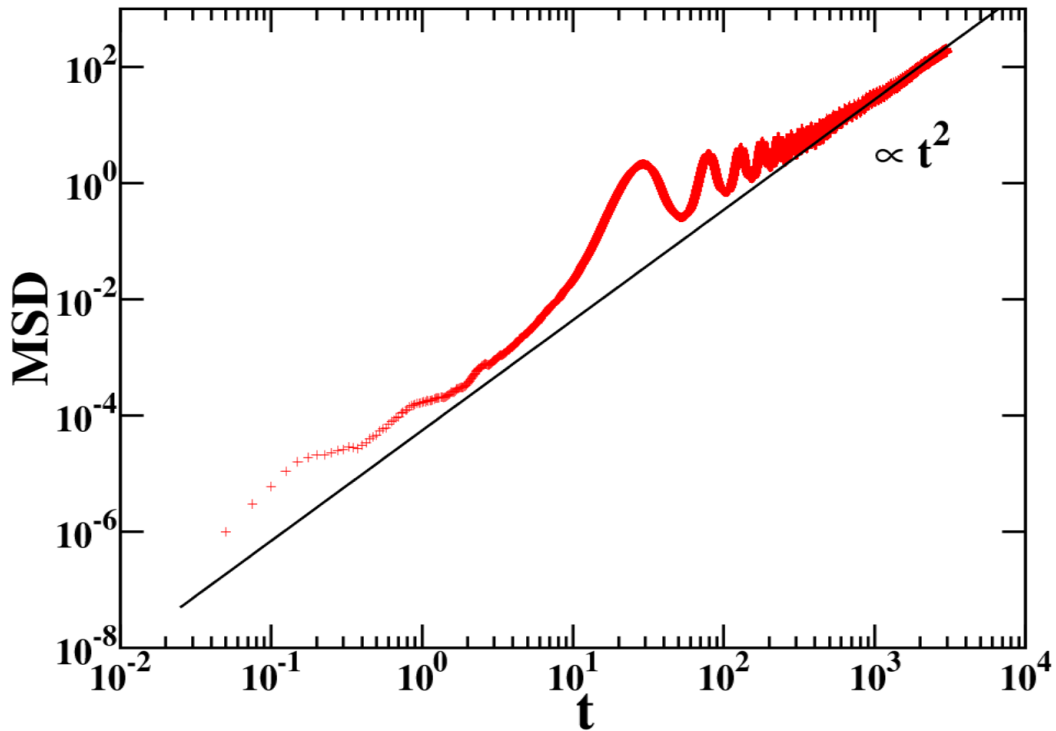


Fig. 6.2 Mean square displacement (MSD) of the center of mass is shown as a function of time t for an elastic scallop.

hinge travels toward edges. But there is a delay for the perturbation to reach the end of the flaps. Due to this the flaps closer to hinge react faster as compared to the ends. So as the flaps close, the edges bend in an outward direction. Contrary to this when flaps open, the edges bend in an inward direction. So in case of flexible flaps, the movements of closing and opening of the flaps do not remain identical under time inversion. Hence, Scallop theorem breaks here and swimmer performs ballistic motion in an upward direction. To quantify the above observation, in figure 6.2 we plot the mean square displacement of the center of mass with time. MSD fits with a slope of 2 which indicates that elastic scallop execute ballistic motion at low Reynolds number.

6.2.3 Speed

We know that the flexibility is the key ingredient here that affects the speed of the scallop. To show the dependency of velocity on flexibility, in figure 6.3 we plot scaled velocity with respect to bending rigidity K_{b_L} along the length of the flaps. Similar to elastic filament [79, 83, 84] and 2-D one-hinge swimmer, we get different regimes. One, where bending forces dominate and flaps of the scallop act like rigid sheet. Second,

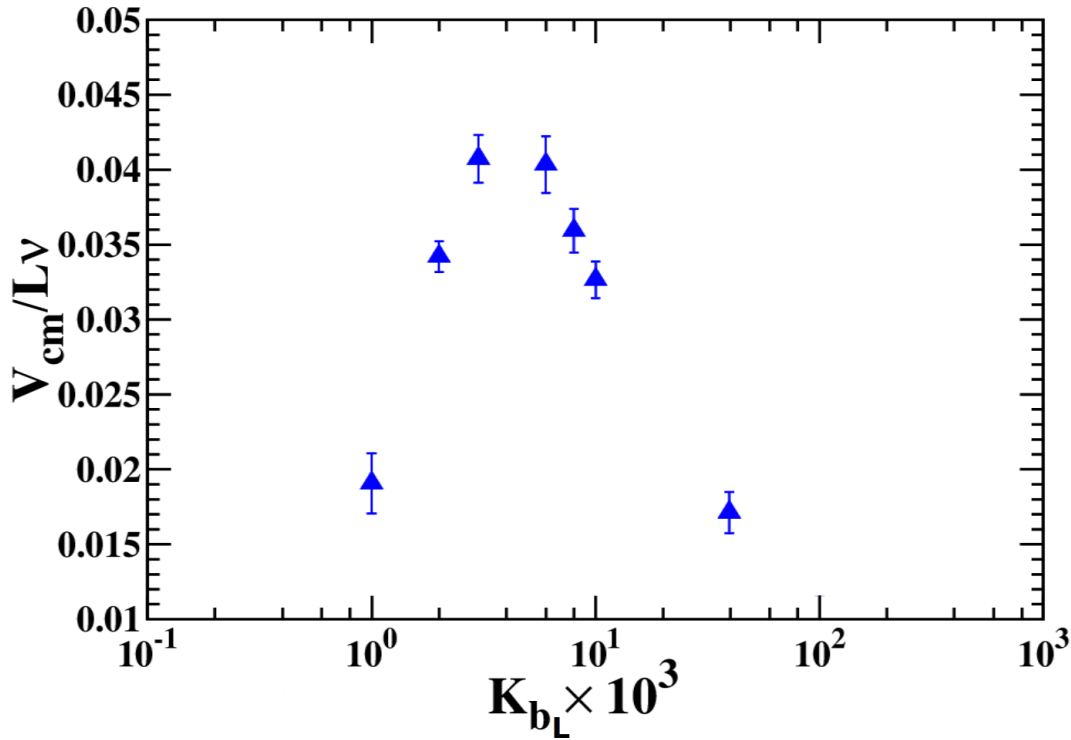


Fig. 6.3 The reduced velocity of the scallop is plotted as a function of bending rigidity K_{bL} along the length of the scallop flaps.

where the viscous forces dominate and suppress the elastic wave propagation. The middle regime between these two provides maximum speed as can be seen in figure 6.3.

We have always considered the total length of the flaps L equal to the width of the flaps W . Now we vary the width of the scallop to check what happens when $L \gg W$, while keeping L fixed. In figure 6.4, we plot the scaled velocity with respect to the width of the elastic scallop. We start with a width $W = 25$ and $L = 20$. Swimmer moves perfectly in the upward direction and as we start decreasing the value of W , the speed of the swimmer goes down. This is because when the width of the flap is large, scallop interacts with more solvent particles and force imposed by solvent, that pushes the scallop forward, has a larger magnitude and therefore swimmer swims with a greater speed. As we further decrease the width W , speed goes down monotonically and decreasing width also induce a little imbalance that generates a slight rotation in the scallop which reduces the speed and the swimming trajectory no longer remains straight. Here the flaps of the scallop have a length and a width, but do not have a breath (thickness). So in order to maintain the balance the width should be in the accordance of the length. To get the proper opening and closing shape of the scallop, we can not go for very small width. The

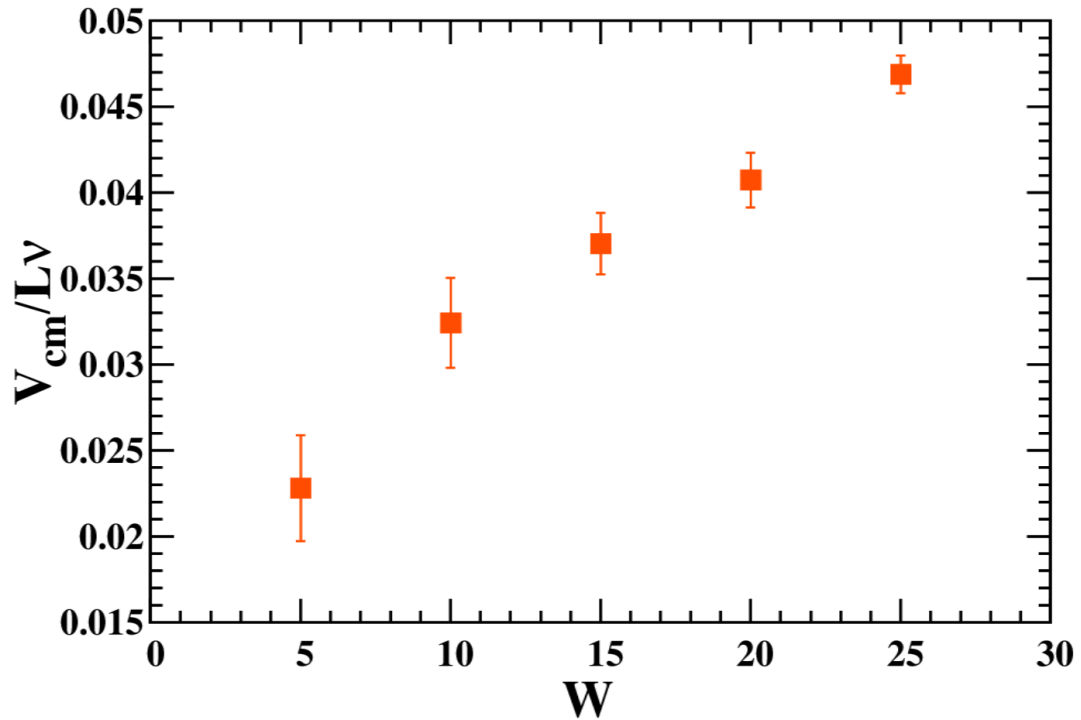


Fig. 6.4 The reduced velocity of the scallop is plotted as a function of Width W of the flaps of an elastic scallop.

minimum width we have considered is $W = 5$. For this we get a very small velocity so we did not go below that. For minimum width $W = 5$, we have considered the total length of the flaps $L = 20$. That means we have considered a width 4 times smaller than the total length of the flaps.

6.3 Conclusions

In this chapter, we have shown that the hydrodynamic interactions between the mass points of the scallop and the solvent particles can be simulated using multi-particle collision dynamics (MPC). We have demonstrated that if the flaps of scallop are very rigid, it follows the reciprocal motion and do not propel itself through the viscous fluid. When the flaps are made flexible, the time inversion symmetry is broken and scallop performs ballistic motion in low Reynolds number. We have also shown that the velocity of the scallop has a maximum for intermediate bending rigidity along the length of the flaps. For small bending rigidity, the flaps are very flexible and the actuation created at hinge are not able to reach towards the edges. While for stiff flaps, we are closer to the Scallop theorem and the velocity goes towards zero. The scaled velocity is also studied

as a function of width W of the scallop where we have shown that smaller width results into rotation and larger is the width higher is the velocity.

Chapter 7

Swimming of a waving sheet in a viscous fluid

We present the study of swimming of a finite size Taylor sheet in a viscous fluid. To model the waving Taylor sheet, we use bead-spring model with the bending potentials. To consider the hydrodynamic interactions between the beads, we employ the Rotne-Prager mobility tensor. We show in the present study that for a rectangular sheet, the frequency of the wave oscillation is proportional to the wave velocity and also the flow field created by the sheet is the similar to that of the infinitely long Taylor sheet. In the present study, we show that the ratio of the perpendicular and parallel friction coefficient is no longer a constant but varies with the dimensions of the sheet. The velocity of the sheet scales very well with the finite length approximation of the Taylor sheet. The stroke efficiency of the swimmer is also calculated which shows similar trends as the velocity with the finite dimensions of the sheet.

7.1 Introduction

Understanding the locomotion of micron scale organisms is one of the most important challenges of the science. The swimming of the African Trypanosomes in the blood vessels [96, 134] or the locomotion of algae and bacteria to find nutrient sources [26] are some of the examples. As we know that the swimming in micron-scale is entirely

different from the macro-scale swimming as inertia is absent here [10, 56]. To propel in inertia less world, micro-organisms employ different swimming machinery, like rotating flagella in *Escherichia coli* [25], planar waving flagelum in Spermatozoa [24] and two waving flagella in *Chlamydomonas reinhardtii* [51] etc. Artificial swimmers which use the strategies of the natural swimmer have also been proposed like the Taylor sheet [63] and also those who do not follow the natural biological strategies like Purcell's swimmer [10].

In 1951 Sir Taylor Geoffrey modelled a two-dimensional infinite waving sheet to explain the flagellar swimming [63]. He showed that deformation of the sheet due to propagating wave enables it to self propel at low Reynolds number. Gray and Hancock used resistive force theory and gave a general analysis for the flagellar waveforms [75]. The biological organisms have very thin flagella, so slender body theory holds good in those cases [56, 69]. The dynamics of flagella have already been investigated in detail, theoretically as well as experimentally, using slender body theory [75, 135]. It has also been studied using different simulation techniques [84, 93, 98]. Though most of the studies have been made considering very thin two-dimensional waving sheet or thin cylindrical flagella, which is the case for real organisms. In the present work we are considering an artificial swimmer or a waving sheet that has finite length as well as width and we want to investigate how the dynamics of the sheet changes as we change the geometric length as well as the width of the sheet. As in case of 3-D elastic scallop, we have seen that change in width changed the dynamics of the swimmer. These kind of waving sheet have been experimentally modelled using the heart cells of the mice [154]. In these experiments, the sheets have a finite width which motivated us to explore the case of finite width Taylor sheet as a model for these kind of artificial swimmers. In order to construct the sheet, we use bead-spring model as described in section 3.2.3 and the hydrodynamic interaction between the beads and friction with surrounding fluid is studied by using the Rotne-Prager approximation mobility tensor [11, 155].

In the present study, we have modelled a three dimensional Taylor sheet using a bead-spring model as illustrated in figure 3.11. The modelling of the swimmer is explained in section 3.2.3. As we have considered stiff springs, the beads of the sheet are well separated. So to consider the hydrodynamic interactions in an unbound fluid, we are

employing Rotne-Prager mobility tensor. In the Rotne-Prager approximation, the cross and self mobilities are given by

$$\Gamma_{ij} = \left\{ \begin{array}{l} \frac{1}{6\pi\eta r_{ij}} \left[\frac{3}{4}(\hat{\mathbf{I}} + \hat{\mathbf{r}}_{ij} \otimes \hat{\mathbf{r}}_{ij}) + \frac{1}{2} \frac{a^2}{r_{ij}^2} (\hat{\mathbf{I}} - 3\hat{\mathbf{r}}_{ij} \otimes \hat{\mathbf{r}}_{ij}) \right], i \neq j \\ \frac{\hat{\mathbf{I}}}{6\pi\eta a}, i = j \end{array} \right\} \quad (7.1)$$

where $r_{ij} = |\mathbf{r}_j - \mathbf{r}_i|$ is distance from i^{th} bead to j^{th} bead, $\hat{\mathbf{r}}_{ij} = (\mathbf{r}_j - \mathbf{r}_i)/r_{ij}$. We calculate the total force \mathbf{F}_j acting on each bead according to equation 3.11. Once the forces are calculated, the hydrodynamic interactions enter into the calculation through the mobility tensor. So the velocity of each bead is given by $\mathbf{v}_i = \sum_j \Gamma_{ij} \mathbf{F}_j$. To calculate the position of the bead after time $\delta t = 0.001$, we employ simple Euler method for integrating the equations of motion.

The chapter is arranged as follows. In section 7.2, we show how the variation of the sheet dimensions influence the dynamics of the sheet. The flow field created by such a finite sheet is also shown. The variation of the friction coefficient of the sheet is also discussed, followed by how the stroke efficiency of the swimmer changes with increasing the dimension of the sheet. In section 7.3 we conclude our results.

7.2 Results and discussion

As a first check, we have verified that total force and torque on the sheet are zero during the entire course of the simulation. We know that for the Taylor sheet, the direction of motion of the waving sheet should be in the opposite direction of the wave propagation [63]. We verified this in our code by reversing the direction of propagation of the wave and found that direction of the swimmer also reversed accordingly.

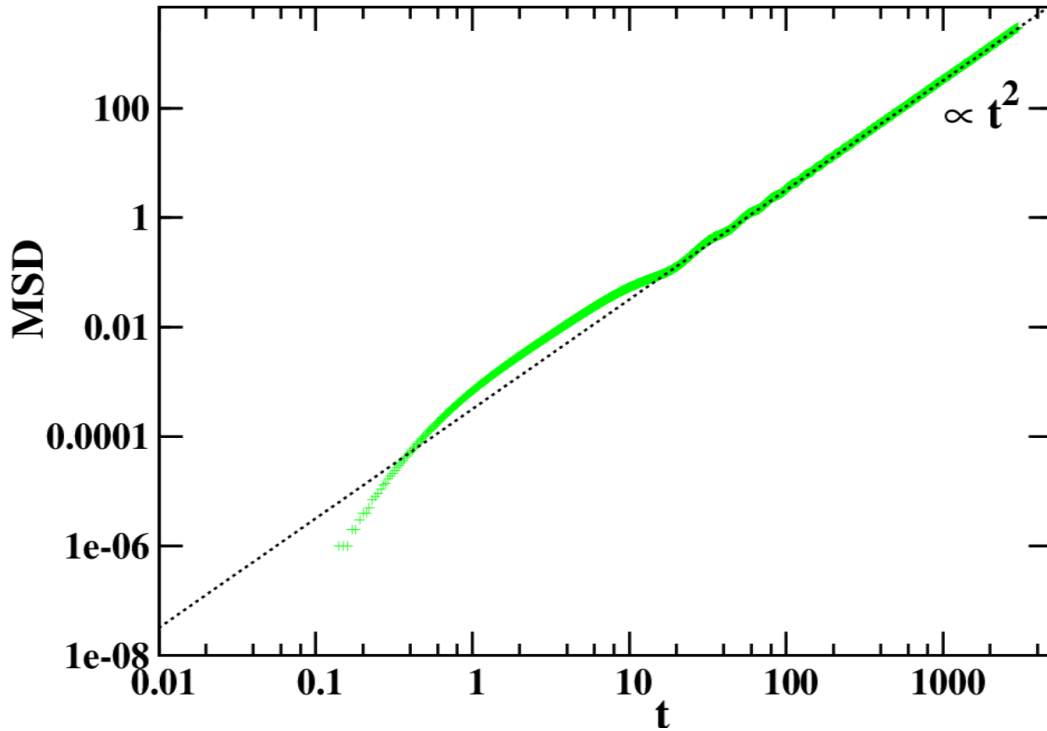


Fig. 7.1 Mean square displacement of the center of mass of sheet for $L = 30$ and $W = 3$ as a function of time. The dotted line has a slope of 2, as expected for ballistic motion.

In figure 7.1, we plot the mean square displacement (MSD) of the center of mass of the swimmer as a function of time. In the Rotne-Prager method, we do not include any thermal fluctuation. During initial time $t < 10$, we observe that the sheet takes some time to relax in steady state due to the effects of bending wave potentials as well as the hydrodynamic interactions acting within the beads. After that we observe that the MSD scales as square of time, signifying ballistic motion as expected for the Taylor sheet.

In figure 7.2, we plot the velocity of the finite Taylor sheet of length $L = 40$ and width $W = 1$ as a function of the frequency of the bending wave passing through the sheet. L is always measured when there is no wave passing through the sheet. We know that for an infinite length Taylor sheet, the frequency scales linearly with the velocity of the sheet. In the case of finite length and width Taylor sheet, we also observe that the velocity scales linearly with velocity, giving us indication that the finite Taylor sheet may be behaving similarly to the infinite length Taylor sheet.

In figure 7.3, we plot the 2-D projection of the flow field created by the swimming sheet. In figure 7.3(a), wave is propagating in positive x direction (right) and sheet is

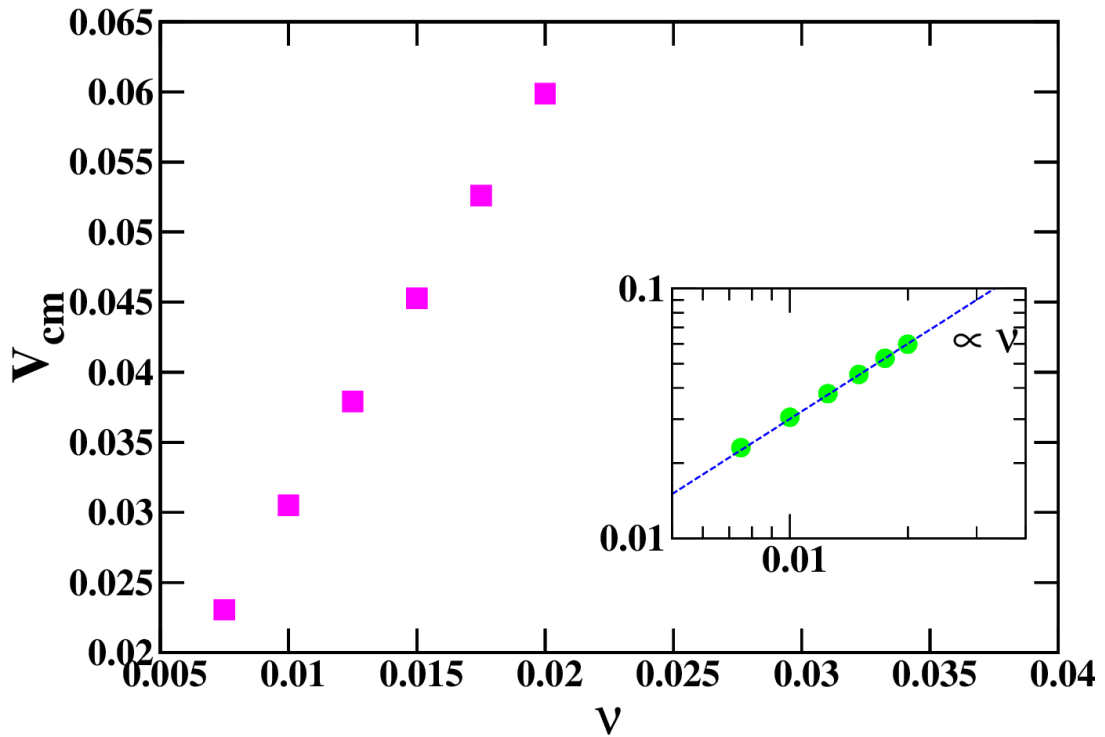


Fig. 7.2 Center of mass velocity of the sheet for $L = 40$ and $W = 1$ as a function of frequency, inset shows the dependency of velocity on frequency in log scale. The dotted line in the inset has slope of one.

moving in the negative x -direction (left) and in figure 7.3(b), wave is propagating in the negative x -direction and the sheet is moving in positive x direction. In flow field, we can observe four curls which are formed due to the formation of four crests and troughs during waving of the Taylor sheet. To analyze the flow field 7.3(a), we pick one wave train of the sheet which is represented with different colors of the beads. When we draw an arrow on the yellow beads, from the right yellow bead to left yellow bead, this indicates the local swimming direction of the swimmer, as the sheet is moving from right to the left. So for this half part of the wave train near the beads, fluid moves in an anti-clockwise direction and creates a curl that pushes the swimmer to the left due to the no slip boundary condition. Similarly, we can analyze the remaining half part of the wave train, where near the pink beads fluid is following the direction of the motion of the pink beads and so on for green and red beads. Near these beads, the fluid is moving in a clockwise direction and again creates a curl that pushes the swimmer to the left. In figure 7.3(b), the direction of the swimming is to the right, so the direction of the curls should be the opposite to that of 7.3(a). In figure 7.3(b), if we look at the left wave train it is clear that the right

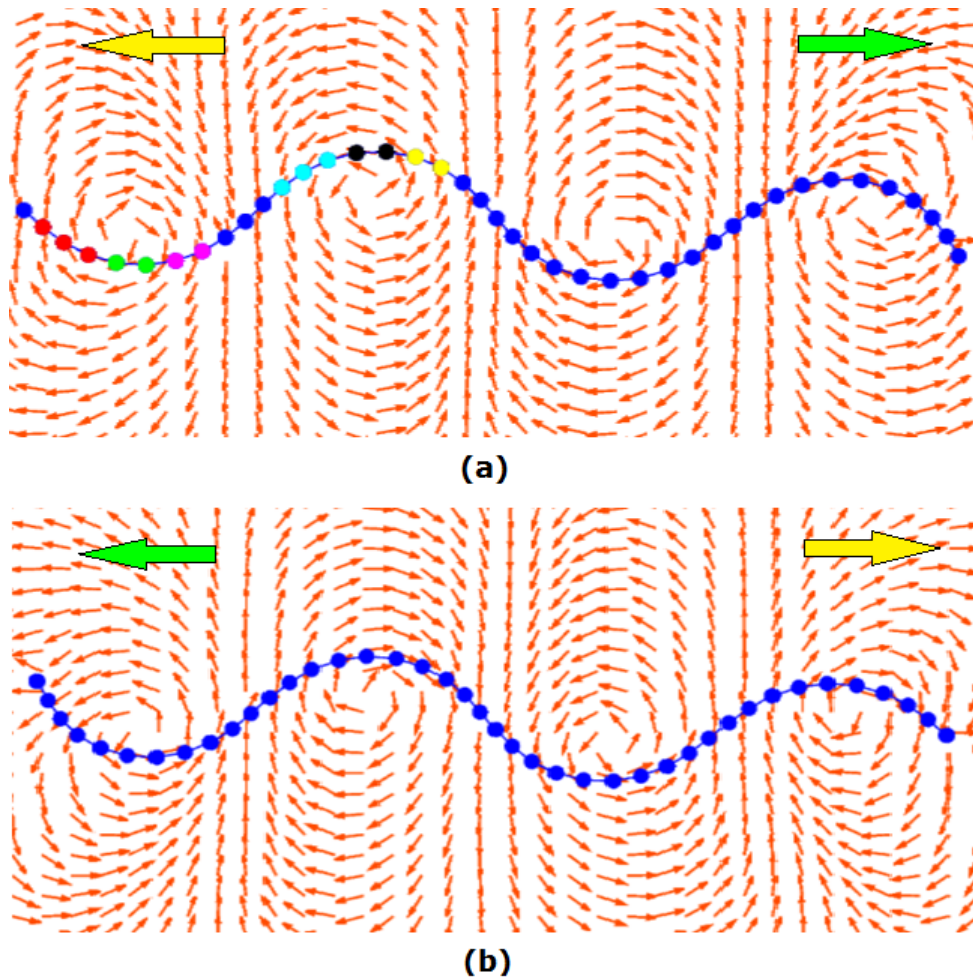


Fig. 7.3 Flow field created by the waving sheet. In (a) different colors are shown to explain flow field (see text). The green arrow shows the direction of wave propagation and yellow arrow shows the direction of motion of the sheet. The red arrows represent the unit vector of velocity obtained from simulation.

half of this wave train makes a clockwise curl and left half makes an anti-clockwise curl which is opposite to the other case as expected.

For slender bodies, according to the resistive force theory, the propulsion velocity for a finite length and zero width sheet through which a planar wave passes is given by [13]

$$V = \frac{A^2 w k}{2} \left(\frac{\xi_{\perp}}{\xi_{\parallel}} - 1 \right) \left(\frac{1}{1 + \frac{R_h}{N \lambda \xi_{\parallel}}} \right). \quad (7.2)$$

Here N is the number of wave trains in flagella, ξ_{\perp} and ξ_{\parallel} are a normal and parallel component of drag coefficient of the slender body and R_h is the drag coefficient of the passive head. In the present case we do not have the passive particle as the head, so

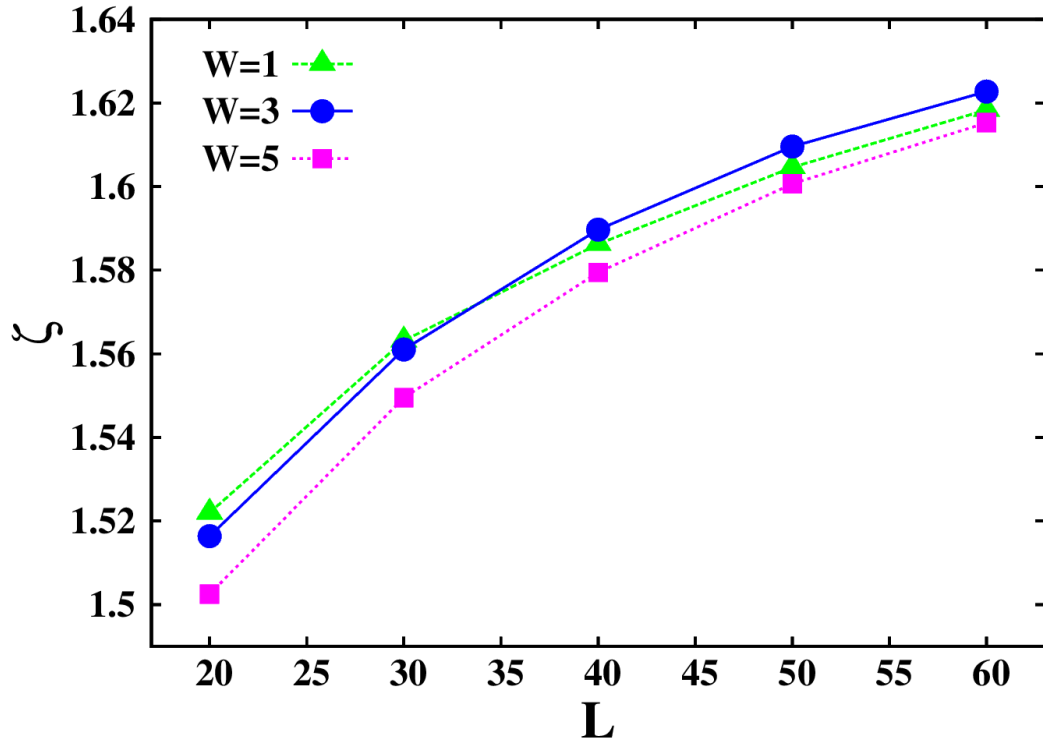


Fig. 7.4 The ratio of friction coefficient of the swimmer as a function of length of the swimmer for 3 different widths.

we consider $R_h = 0$. If we keep our amplitude, wave number and velocity of the wave constant, we know that the velocity of the swimmer depends only on the fraction of friction coefficient of the perpendicular and parallel component. To verify the dependence on the ratio $\frac{\xi_{\perp}}{\xi_{\parallel}}$, when we have finite length and width of the sheet, we plot the ratio $\frac{\xi_{\perp}}{\xi_{\parallel}} = \zeta$ versus the length of the sheet. To calculate ξ_{\perp} , we drag the flat stiff sheet along the perpendicular direction of the plane of the sheet. Then the velocity of the sheet is calculated as it moves ballistically through the fluid. The slope of the force versus the velocity curve gives us the friction coefficient along the perpendicular direction. Similarly we have calculated the parallel component of the friction coefficient. From figure 7.4, we observe that the ratio ζ is dependent on length as well as width. As the width increases, the ratio becomes smaller and smaller. In case of $W = 1$, we observe that the ratio fall below $W = 3$ for long lengths. Because for long sheets, as the width decreases the sheet becomes more and more flexible and is not able to stay stiff. For $W = 3$ we observe a similar behavior when the length of the sheet is further increased beyond $L = 60$.

As explained before, we are considering a 2-D sheet in a three-dimensional space and we are interested to know how the velocity of the swimming sheet changes as we vary

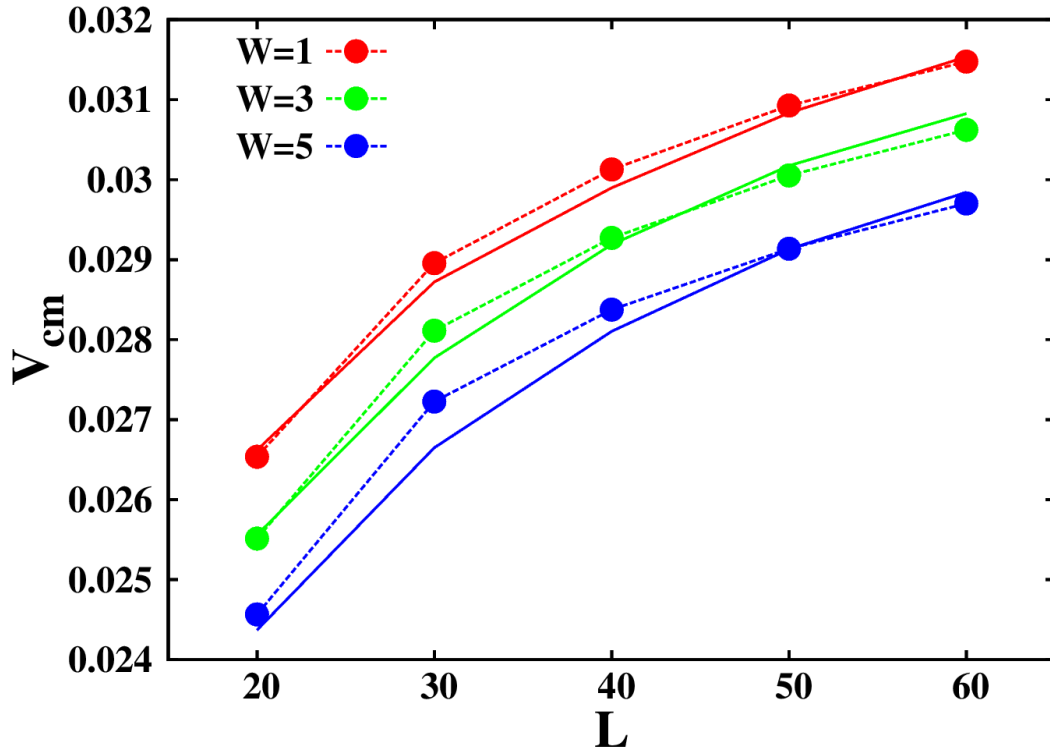


Fig. 7.5 The center of mass velocity of the swimmer as a function of the length of the swimmer for 3 different widths. The solid lines represent the analytical calculation from equation 7.2

the width. In figure 7.5, we plot the center of mass velocity of the sheet as a function of the length of the sheet for three different widths, keeping all other parameters fixed, where frequency $\nu = 0.02$, the amplitude of Taylor sheet $A = 1.35$ and wavelength $\lambda = 7.9$. Note that when we vary the length of the sheet, we keep the wave length λ and amplitude of the sheet same. To do that, we just increase the number of wave trains. For instance, if $L = 20$ contains two wave trains, and when we make length $L = 30$, one more wave train gets added up. In the figure 7.5, we can see that as we increase the width of the sheet the velocity decreases as the friction experienced by the sheet increases with the increasing width. We calculated the quantity $\beta = V/(\frac{\xi_{\perp}}{\xi_{\parallel}} - 1)$ and found that the value remains constant for particular values of width. From the slender body theory equation 7.2, we get the constant $\beta = \frac{A^2 w k}{2} \approx 0.09$. But from our simulation, for $W = 1$ we obtain $\beta = 0.051$, for $W = 3$ we obtain $\beta = 0.0495$ and for $W = 5$ we obtain $\beta = 0.0485$. The solid line in the figure 7.5 is plotted using this constant which gives us the indication that β is not following the same relation as in equation 7.2. Unfortunately, in the present model we are not able to change the amplitude and wavelength independently to study the effect on the constant β .

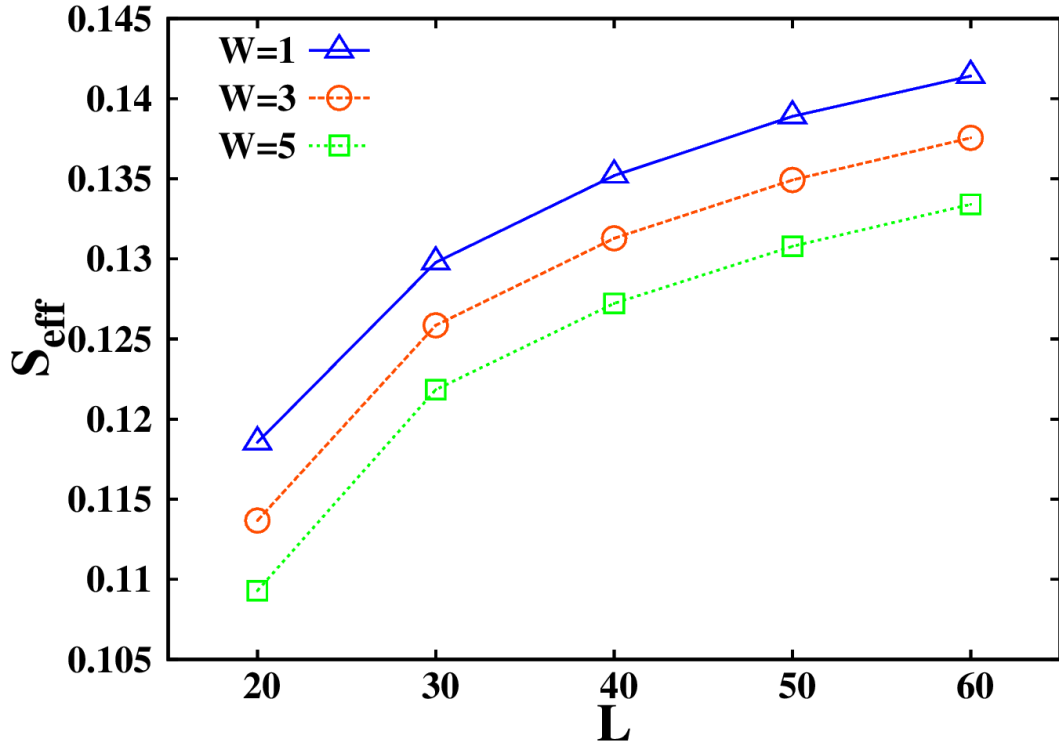


Fig. 7.6 Variation in stroke efficiency for the sheet swimmer for different lengths for 3 different widths. The lines are guide to the eyes.

In figure 7.6, we plot stroke efficiency as a function of length. We define stroke efficiency as

$$S_{eff} = \frac{\langle v_{\parallel} \rangle}{c} \quad (7.3)$$

here $\langle v_{\parallel} \rangle$ is the component of the velocity parallel to the direction of swimming and $c = \lambda\nu$ is phase velocity at which bending wave travels along the sheet, for more detail see ref. [98]. Typically for the infinite Taylor sheet $S_{eff} \approx 0.57$, if we plugin our values from the simulations. In figure 7.6, we observe that the stroke efficiency of all the swimmers that we have considered will never go above the infinite Taylor sheet. S_{eff} is decreasing as we are increasing the width. The reason being that as we increase the width of the sheet, the friction force acting on the sheet increases. Also when the length increases, the ratio of $\xi_{\perp}/\xi_{\parallel}$ increases which enhances the swimming. This is the reason why $L = 30$ with $W = 3$ has a higher efficiency than $L = 20$ with $W = 3$.

7.3 Conclusions

In this chapter, we have shown that the Rotne-Prager mobility tensor is able to simulate the dynamics of a waving sheet. We confirmed that the relation of the velocity with the frequency is linear for the finite Taylor sheet. We observed that in three-dimensions, the width of the sheet plays an important role in changing the dynamics of the sheet. Here we have shown that as we increase the width of the sheet, velocity decreases as the friction along the width increases. The ratio of the parallel and perpendicular component of the friction coefficient is no longer a constant for a finite sheet and depends on the length and the width of the sheet. The slender body theory qualitatively explains the velocity of the finite Taylor sheet. The stroke efficiency of the swimmer gets enhanced for long and slender sheets than for shorter and wider sheets.

Chapter 8

Conclusions and Future Scope of Work

8.1 Conclusions

In this thesis, we present the dynamics of an artificial micro-swimmer in a Newtonian fluid. Our results can provide important guidance in the construction of robotic micro-swimmers. The following conclusions are made on the basis of the study carried out:

- ✓ The hydrodynamic interactions between the mass points of the one-hinge swimmer and the fluid particles can be simulated using multi-particle collision dynamics (MPC).
- ✓ If the arms of the one-hinge swimmer are very rigid, it follows the Scallop theorem and the swimmer is not able to propel itself through the viscous fluid as expected. But when the arms are made semi-flexible, the time inversion symmetry is broken and swimmer performs ballistic motion.
- ✓ For small bending rigidity, the arms are very flexible and the viscous forces dominate here. While for stiff arms, bending forces dominate and we are closer to the Scallop theorem. So the velocity approaches to zero. For intermediate bending rigidity, the viscous forces and bending forces balance each other and the velocity of the swimmer reaches to maximum.
- ✓ Note that in the case of biological scallop, the rate of closing and opening of the flaps is not same which is the reason for the propulsion of the macro scallop. But in our simulations, we always considered that the rate of closing and opening of the flaps are same, and the flexible micro-scallop is still able to propel.

- ✓ We have calculated the reduced velocity of the swimmer as a function of frequency as well as the amplitude of actuation. We found that the reduced velocity scales linearly with frequency and scales as the square with amplitude, which is in agreement with elasto-hydrodynamic theory.
- ✓ The elasto-hydrodynamic theory considers small amplitude approximation, even though we have considered large amplitude in the present work, but still getting the scaling in agreement with theory.
- ✓ We have also calculated the Sperm number for the swimmer and found that the reduced velocity had a maximum at $S_p \sim 1.8$ which is consistent with what is expected for large amplitude actuation.
- ✓ We have shown that the swimming speed can be enhanced, if we progressively decrease the bending rigidity from hinge to edge. For that, we considered a swimmer with moderate $S_p \sim 1.8$ value and progressively changed the K_b in a geometric sequence and found that the speed of the swimmer enhanced approximately 25%.
- ✓ Further we have considered a swimmer which has arms with asymmetric bending rigidity. We have demonstrated that asymmetry causes circular swimming trajectory and we can change the direction of motion accordingly. If we keep right arm more rigid as compared to left arm, swimmer moves in a right circular pattern. And opposite to this, if left arm is comparatively stiffer, then swimmer follows left circular path. When one arm is extremely rigid and the second one has moderate rigidity having Sperm number $S_p \sim 1.8$, then this combination produces maximum angular velocity and swimming trajectory has a larger curvature as well.
- ✓ We have also studied the dynamics of three-dimensional flexible sheet scallop. We studied the scaled velocity as a function of width W of the flaps, where we found that smaller width results in rotation and larger is the width higher is the velocity. So for a 3-D flexible sheet scallop, there should be a finite width to obtain straight swimming trajectory.
- ✓ We observed that in 3-D, the width of the sheet plays an important role in changing the dynamics of the sheet. In case of the Taylor sheet model, we have shown that

as we increase the width of the sheet, velocity decreases as the friction along the width increases.

- ✓ The ratio of the parallel and perpendicular components of the friction coefficient is no longer constant for a finite sheet and depends on the length and width of the sheet. The slender body theory qualitatively explains the velocity of finite Taylor sheet.
- ✓ We have also shown that the stroke efficiency of the Taylor sheet gets enhanced for long and slender sheets as compared to the shorter and wider sheets.

8.2 Future scope of the work

In reality, most of the micro swimmers deal with confined fluid. The experimental observations have revealed that the presence of a boundary remarkably affects the dynamics of swimming micro-organisms, for example near surface trajectory of *E. Coli* changes from straight to circular one [156], changes in bacterial motility on a surface [157], accumulation of spermatozoa nearby boundaries [158], hydrodynamic attraction by surfaces [159]. The importance of boundaries has also been manifested by theoretical studies. Berke et al. [159] theoretically exhibited that hydrodynamic interactions of swimmers with solid walls are responsible for their reorientation in the direction parallel to the walls and their attraction by the nearest wall. Zarger et al. [160] observed the effect of the wall on three linked-sphere swimmer and shown that when the swimmer is close to the wall, the velocity of swimmer decreases as $(z/L)^2$, where z is swimmer distance to the wall and L is the arm length. Crowdy et al. [161] demonstrated a simple 2-D point singularity model of a low Reynolds number swimmer near a no-slip boundary. They showed that in the absence of boundary or in an unbounded fluid, the velocity profile created by the point singularity swimmer does not lead to any self-propulsion due to its symmetry about two axes, but the swimmer starts moving when it interacts with a boundary. These observations emphasize that the presence of the boundary plays a major role in the dynamics of the microorganisms and in order to get an extensive understanding of low Reynolds number locomotion, it is essential to study hydrodynamic interactions between organisms and boundaries.

It will be interesting to examine the dynamics of a one-hinge swimmer near boundaries. Here, we are going to show some initial results in the presence of boundaries which we can carry forward in the future. As we know that a rigid one-hinge swimmer can not propel by itself at low Reynolds number [10]. Therefore in order to understand and isolate just the hydrodynamic interaction of the swimmer and the wall, we are focusing on a non-self propelling rigid swimmer. Near the walls to implement the no-slip boundary condition we have used bounce back rule with virtual particles [113] as explained in subsection 3.1.6. At first we check the effect of a single wall. We consider a square simulation box of size $L_x = 200$ & $L_y = 200$ and place a rigid swimmer near the bottom wall of the box as shown in figure 8.1(a) and 8.1(b). The top wall of the box is at a distance of almost 8 times of the length of the arm of the swimmer from the swimmer, so we can ignore the top wall effect and for now we will talk only about the bottom wall. Lauga et al. [156] demonstrated that circular trajectories are natural outcomes of force free & torque free swimming and hydrodynamic interactions with the surfaces. As our swimmer is also force free & torque free and when it comes in contact with a wall it gets rotated as expected. Here we consider two different orientations of the initial position of the swimmer, in first case we take the left facing swimmer which rotates in an anticlockwise direction as depicted in figure 8.1(a) and in another case we take the right facing swimmer which rotates in clockwise direction as illustrated in figure 8.1(b). These rotations occur as swimmer interacts with its mirror image situated on the other side of the wall as shown in the case of puller and pusher [56]. In both the cases, we can see that the front part of the swimmer gets attracted towards the wall and as a consequence left facing swimmer rotates in anti-clockwise and right facing swimmer rotates in clockwise direction.

In the next step, we locate the swimmer in between the two walls. Similar to the previous case, we consider two initial orientations as depicted in figure 8.1(a) and 8.1(b). At first we are considering left oriented swimmer. In the beginning swimmer gets rotated in any of the direction either anti-clockwise or clockwise as indicated by the black arrow in figure 8.1(a₁) and 8.1(a₂). This is because at initial point both the walls are situated at equal distance, so the swimmer gets attracted by any of the walls. After rotation, on an average one of the arm of the swimmer is parallel to the walls and other arm is perpendicular to the walls as shown in figure. Subsequently, the swimmer instead of rotating starts moving towards the right as indicated by green arrows. When we consider

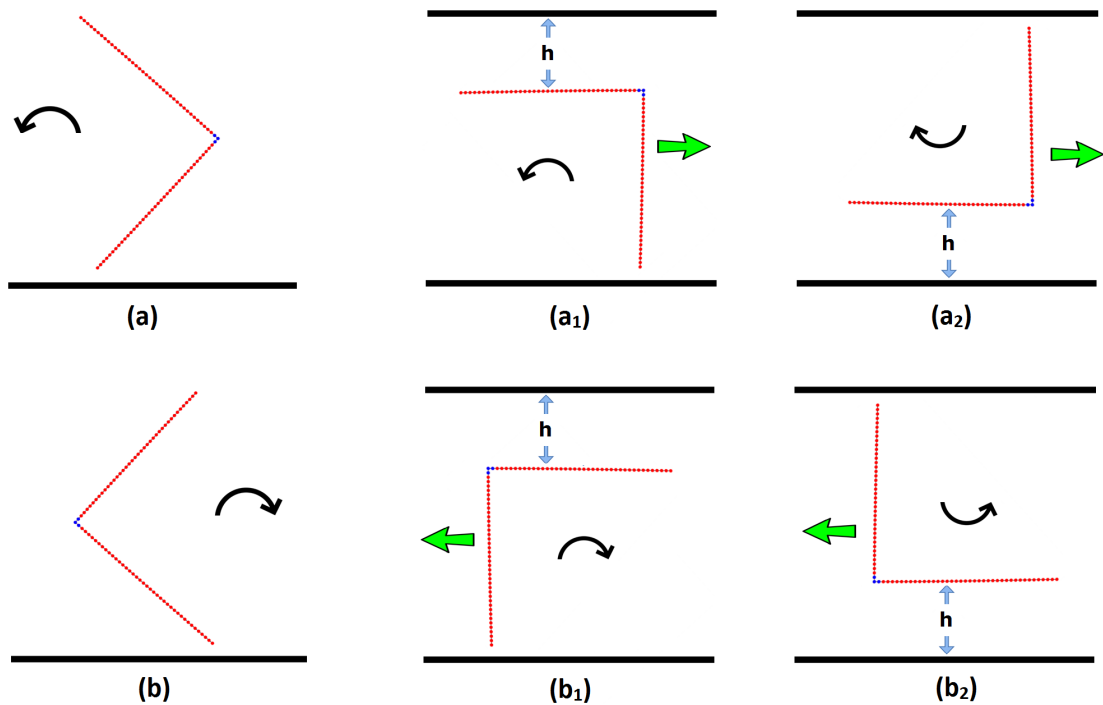


Fig. 8.1 Here (a) and (b) shows two different orientations of the initial position of the swimmer near a single wall, where the black arrows show the direction of rotation. When we place swimmer between two walls, in case of (a₁) & (a₂) initially the swimmer was oriented as shown in (a) and in case of (b₁) & (b₂) initially the swimmer was placed as shown in (b). In the beginning swimmer rotate toward any of the wall as indicated by the black arrow and after a rotation it start moving in backward direction as indicated by green arrows.

right oriented swimmer it moves towards the left as depicted in figure 8.1(b₁) and 8.1(b₂). It is surprising because we know that a rigid one-hinge swimmer can not move in a viscous fluid due to the reciprocal motion [10]. In general the no-slip boundary condition near the surface does not get satisfied by the original set of singularities [56] and an object experiences a different drag near the boundary and motility as part of consequences. For example, the translational motility of a sphere decreases near a boundary, and also the translational motility parallel to the boundary is higher than the translational motility perpendicular to the boundary [162, 163]. Here the propulsion is may be because both the arms of the swimmer are near to the walls and have different orientations, one is parallel and another is perpendicular to the walls, hence experiencing different drags [56]. Since the propulsion is also drag based, then probably it is making the swimmer motile here. Similar to the present case, Crowdy et al. showed that a point singularity swimmer does not propel unless it interacts with the boundary [161].

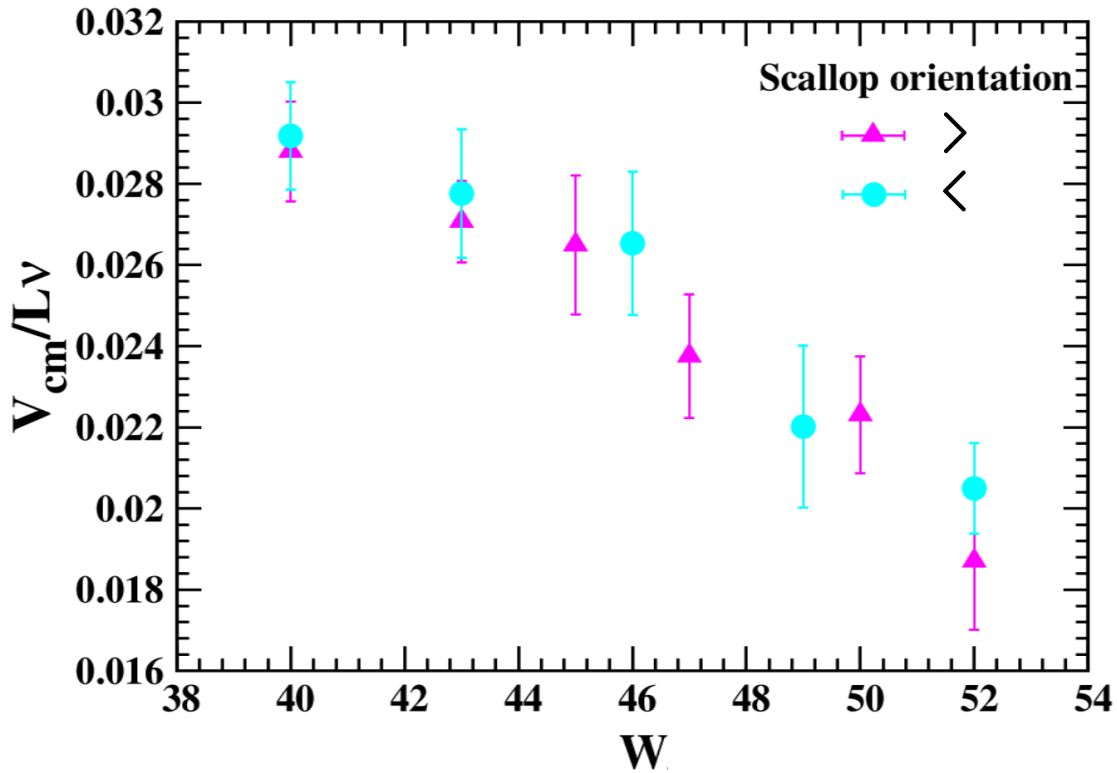


Fig. 8.2 The reduced velocity is plotted as a function of the channel width.

Further, in figure 8.2 we have shown how the reduced velocity $V_{cm}/L\nu$ of the swimmer changes as we change the distance between the walls or channel width (W). Here V_{cm} is the center of mass velocity of the swimmer, $L = 20$ is length of the arm of the swimmer and $\nu = 0.01$ is the frequency of the opening and closing of the arms. Note that the swimmer is always placed at equal distance from both the walls. Initially, we start from a channel width equal to $2L$ and then gradually increases the width of the channel and find that the reduced velocity decreases as we increase the channel width. As we have mentioned earlier that swimmer always gets attracted by any of the wall, let's say by wall X (other one is wall Y) and its arm that is perpendicular to the wall is always close to the wall X that attracted the swimmer as shown in figure 8.1. So when we increase the width of the channel, basically we are increasing the distance h between wall Y and the arm of the swimmer that is parallel to the walls as shown in figure 8.1. As we are decreasing h , velocity of the swimmer is increasing and for a maximum distance swimmer stops propelling. There will be only rotation similar to the case of a single wall. So we may speculate that the interaction of the parallel arm with wall is important for locomotion. In figure 8.2, we have shown the data for both the left and right oriented swimmer and get the same velocity within the error bar as it should be. The only difference is that the

direction of the motion is opposite. Therefore from initial orientation of the swimmer we can decide the direction of motion. Based on these findings, future scope of the work can be proposed as follows:

- A detailed investigation of why a rigid swimmer attains a small velocity when placed between two narrow walls.
- Study the dynamics of a flexible swimmer near the walls and obstacles as well.
- Study the behavior of the swimmer in Poiseuille flow.
- Other than boundary effect, we can study a swimmer with different rate of closing and opening the arms.
- Study the behavior of the swimmer when there are multiple swimmers.
- Study the dynamics of a swimmer having arms or filaments more than two in number.

References

- [1] <https://safetymessenger.in/wp-content/uploads/2014/12/robots.jpg>.
- [2] <https://jennarever.weebly.com/unit-1-cell-structure.html>.
- [3] https://commons.wikimedia.org/wiki/file:os_microbio_03_03_runtumble.jpg.
- [4] <https://microbewiki.kenyon.edu/index.php/caulobacter>.
- [5] http://cronodon.com/biotech/purple_bacteria.html.
- [6] Patricia A Rosa, Kit Tilly, and Philip E Stewart. The burgeoning molecular genetics of the lyme disease spirochaete. *Nature Reviews Microbiology*, 3(2):129–143, 2005.
- [7] <https://fineartamerica.com/featured/1-paramecium-with-ejected-trichocysts-eric-v-grave.html>.
- [8] <http://botanystudies.com/chlamydomonas-structure-reproduction/>.
- [9] J Fletcher and A Wayadande. Fastidious vascular-colonizing bacteria. the plant health instructor. *The American Phytopathological Soc.*, 2002.
- [10] E. M. Purcell. Life at low reynolds number. *American Journal of Physics*, 45(1):3–11, 1977.
- [11] Erik Gauger and Holger Stark. Numerical study of a microscopic artificial swimmer. *Phys. Rev. E*, 74:021907, Aug 2006.
- [12] J.M. McDonough. *LECTURES IN ELEMENTARY FLUID DYNAMICS: Physics, Mathematics and Applications*. University of Kentucky, Lexington.
- [13] On Shun Pak and Eric Lauga. Theoretical models of low-reynolds-number locomotion. In *Fluid-Structure Interactions in Low-Reynolds-Number Flows*, pages 100–167. Royal Society of Chemistry, 2015.
- [14] Tony S Yu, Eric Lauga, and AE Hosoi. Experimental investigations of elastic tail propulsion at low reynolds number. *Physics of Fluids*, 18(9):091701, 2006.
- [15] Marcus L. Roper Marc Fermigier Howard A. Stone Rémi Dreyfus, Jean Baudry and Jérôme Bibette. Microscopic artificial swimmers. *Nature*, 437:862–865, 2005.
- [16] Wei Gao, Sirilak Sattayasamitsathit, Kalayil Manian Manesh, Daniel Weihs, and Joseph Wang. Magnetically powered flexible metal nanowire motors. *Journal of the American Chemical Society*, 132(41):14403–14405, 2010.
- [17] Brian J Williams, Sandeep V Anand, Jagannathan Rajagopalan, and M Taher A Saif. A self-propelled biohybrid swimmer at low reynolds number. *Nature communications*, 5:3081, 2014.

- [18] Chaolei Huang, Jiu-an Lv, Xiaojun Tian, Yuechao Wang, Yanlei Yu, and Jie Liu. Miniaturized swimming soft robot with complex movement actuated and controlled by remote light signals. *Scientific reports*, 5:17414, 2015.
- [19] Eric Lauga. Floppy swimming: Viscous locomotion of actuated elastica. *Physical Review E*, 75(4):041916, 2007.
- [20] Richard P Feynman. There's plenty of room at the bottom. *Engineering and science*, 23(5):22–36, 1960.
- [21] <https://www.livestrong.com/article/456880-the-speed-of-human-swimming/>.
- [22] Espen Holthe, Egil Lund, Bengt Finstad, Eva B Thorstad, and R Scott McKinley. Swimming performance of the european minnow. *Boreal environment research*, 14(2), 2009.
- [23] <http://book.bionumbers.org/how-fast-do-cells-move/>.
- [24] Dennis Bray. *Cell movements: from molecules to motility*. Garland Science, 2001.
- [25] Howard C. Berg and Robert A. Anderson. Bacteria swim by rotating their flagellar filaments. *Nature*, 245:380–382, 1973.
- [26] *E. Coli in motion*.
- [27] H. C. Berg. Motile behavior of bacteria.
- [28] Howard C Berg. The rotary motor of bacterial flagella. *Annual review of biochemistry*, 72, 2003.
- [29] Howard C Berg. Bacterial flagellar motor. *Current Biology*, 18(16):R689–R691, 2008.
- [30] Graeme Lowe, Markus Meister, and Howard C Berg. Rapid rotation of flagellar bundles in swimming bacteria. *Nature*, 325(6105):637–640, 1987.
- [31] Linda Turner, William S Ryu, and Howard C Berg. Real-time imaging of fluorescent flagellar filaments. *Journal of bacteriology*, 182(10):2793–2801, 2000.
- [32] Shigeo Koyasu and Yasuo Shirakihara. Caulobacter crescentus flagellar filament has a right-handed helical form. *Journal of molecular biology*, 173(1):125–130, 1984.
- [33] Helen L Packer, David E Gauden, and Judith P Armitage. The behavioural response of anaerobic rhodobacter sphaeroides to temporal stimuli. *Microbiology*, 142(3):593–599, 1996.
- [34] Judith P Armitage and Rudiger Schmitt. Bacterial chemotaxis: Rhodobacter sphaeroide and sinorhizobium meliloti-variations on a theme? *Microbiology*, 143(12):3671–3682, 1997.
- [35] W Marwan, M Alam, and D Oesterhelt. Rotation and switching of the flagellar motor assembly in halobacterium halobium. *Journal of bacteriology*, 173(6):1971–1977, 1991.
- [36] Ken F Jarrell and Mark J McBride. The surprisingly diverse ways that prokaryotes move. *Nature Reviews Microbiology*, 6(6):466–476, 2008.

- [37] E Canale-Parola ed N R Krieg, MD: Williams J G Holt (Baltimore, and Wilkins). *The spirochetes Bergey's Manual of Systematic Bacteriology*. Springer, 1984.
- [38] Howard C Berg. How spirochetes may swim. *Journal of theoretical biology*, 56(2):269–273, 1976.
- [39] Stuart F Goldstein, Nyles W Charon, and Jill A Kreiling. *Borrelia burgdorferi* swims with a planar waveform similar to that of eukaryotic flagella. *Proceedings of the National Academy of Sciences*, 91(8):3433–3437, 1994.
- [40] Howard C Berg and Linda Turner. Movement of microorganisms in viscous environments. *Nature*, 278(5702):349–351, 1979.
- [41] S Nakamura, Y Adachi, T Goto, and Y Magariyama. Improvement in motion efficiency of the spirochete *brachyspira pilosicoli* in viscous environments. *Biophysical journal*, 90(8):3019–3026, 2006.
- [42] Gavin E Murphy, Eric G Matson, Jared R Leadbetter, Howard C Berg, and Grant J Jensen. Novel ultrastructures of *treponema primitia* and their implications for motility. *Molecular microbiology*, 67(6):1184–1195, 2008.
- [43] Joshua W Shaevitz, Joanna Y Lee, and Daniel A Fletcher. Spiroplasma swim by a processive change in body helicity. *Cell*, 122(6):941–945, 2005.
- [44] Howard C Berg. How spiroplasma might swim. *Journal of bacteriology*, 184(8):2063–2064, 2002.
- [45] Shlomo Trachtenberg and Rami Gilad. A bacterial linear motor: cellular and molecular organization of the contractile cytoskeleton of the helical bacterium *spiroplasma melliferum* bc3. *Molecular microbiology*, 41(4):827–848, 2001.
- [46] Charles W Wolgemuth, Oleg Igoshin, and George Oster. The motility of mollicutes. *Biophysical journal*, 85(2):828–842, 2003.
- [47] Michael Werner and Leigh W Simmons. Insect sperm motility. *Biological Reviews*, 83(2):191–208, 2008.
- [48] J QUICKE, L DONALD, SIMON N INGRAM, HELEN S BAILLIE, and PAULINE V GAITENS. Sperm structure and ultrastructure in the hymenoptera (insecta). *Zoologica Scripta*, 21(4):381–402, 1992.
- [49] Machiko HATSUMI and Ken-Ich WAKAHAMA. The sperm length and the testis length in *drosophila nasuta* subgroup. *The Japanese Journal of Genetics*, 61(3):241–244, 1986.
- [50] D Joly, C Bressac, and D Lachaise. Disentangling giant sperm. *Nature*, 377:202, 1995.
- [51] David R. Mitchell. *Chlamydomonas* flagella. *Journal of Phycology*, 36(2):261–273, 2000.
- [52] IR Gibbons. Cilia and flagella of eukaryotes. *J Cell Biol*, 91(3):107s–124s, 1981.
- [53] Sung-Jin Park, Mattia Gazzola, Kyung Soo Park, Shirley Park, Valentina Di Santo, Erin L Blevins, Johan U Lind, Patrick H Campbell, Stephanie Dauth, Andrew K Capulli, et al. Phototactic guidance of a tissue-engineered soft-robotic ray. *Science*, 353(6295):158–162, 2016.

- [54] Bumjin Jang, Emiliya Gutman, Nicolai Stucki, Benedikt F Seitz, Pedro D Wendel-Garcia, Taylor Newton, Juho Pokki, Olgac Ergeneman, Salvador Panee, Yizhar Or, et al. Undulatory locomotion of magnetic multilink nanoswimmers. *Nano letters*, 15(7):4829–4833, 2015.
- [55] Tianlong Li, Jinxing Li, Hongtao Zhang, Xiaocong Chang, Wenping Song, Yanan Hu, Guangbin Shao, Elodie Sandraz, Guangyu Zhang, Longqiu Li, et al. Magnetically propelled fish-like nanoswimmers. *Small*, 12(44):6098–6105, 2016.
- [56] Eric Lauga and Thomas R Powers. The hydrodynamics of swimming microorganisms. *Reports on Progress in Physics*, 72(9):096601, 2009.
- [57] <https://www.microscopemaster.com/nanobots.html>.
- [58] <https://electronics.howstuffworks.com/nanorobot.html>.
- [59] Stephen Childress. *Mechanics of swimming and flying*, volume 2. Cambridge University Press, 1981.
- [60] RG Cox and SG Mason. Suspended particles in fluid flow through tubes. *Annual Review of Fluid Mechanics*, 3(1):291–316, 1971.
- [61] J Lighthill Sir. Mathematical bio-uiddynamics. *SIAM: Philadelphia, PA*, 1975.
- [62] MJ Lighthill. On the squirming motion of nearly spherical deformable bodies through liquids at very small reynolds numbers. *Communications on Pure and Applied Mathematics*, 5(2):109–118, 1952.
- [63] Geoffrey Taylor. Analysis of the swimming of microscopic organisms. *Proceedings of the Royal Society of London A: Mathematical, Physical and Engineering Sciences*, 209(1099):447–461, 1951.
- [64] Ali Najafi and Ramin Golestanian. Simple swimmer at low reynolds number: Three linked spheres. *Phys. Rev. E*, 69:062901, Jun 2004.
- [65] JE Avron, O Kenneth, and DH Oaknin. Pushmepullyou: an efficient microswimmer. *New Journal of Physics*, 7(1):234, 2005.
- [66] Ali Najafi and Rojman Zargar. Two-sphere low-reynolds-number propeller. *Physical Review E*, 81(6):067301, 2010.
- [67] Alessandro Montino and Antonio DeSimone. Three-sphere low-reynolds-number swimmer with a passive elastic arm. *The European Physical Journal E*, 38(5):42, May 2015.
- [68] Babak Nasouri, Aditi Khot, and Gwynn J. Elfring. Elastic two-sphere swimmer in stokes flow. *Phys. Rev. Fluids*, 2:043101, Apr 2017.
- [69] James Lighthill. Flagellar hydrodynamics. *SIAM Review*, 18:161–230, 1976.
- [70] RG Cox. The motion of long slender bodies in a viscous fluid part 1. general theory. *Journal of Fluid mechanics*, 44(4):791–810, 1970.
- [71] GK Batchelor. Slender-body theory for particles of arbitrary cross-section in stokes flow. *Journal of Fluid Mechanics*, 44(3):419–440, 1970.
- [72] Joseph B Keller and Sol I Rubinow. Slender-body theory for slow viscous flow. *Journal of Fluid Mechanics*, 75(4):705–714, 1976.

- [73] RE Johnson and CJ Brokaw. Flagellar hydrodynamics. a comparison between resistive-force theory and slender-body theory. *Biophysical journal*, 25(1):113–127, 1979.
- [74] Robert E Johnson. An improved slender-body theory for stokes flow. *Journal of Fluid Mechanics*, 99(2):411–431, 1980.
- [75] J Gray and GJ Hancock. The propulsion of sea-urchin spermatozoa. *Journal of Experimental Biology*, 32(4):802–814, 1955.
- [76] Ingmar H Riedel-Kruse, Andreas Hilfinger, Jonathon Howard, and Frank Jülicher. How molecular motors shape the flagellar beat. *HFSP journal*, 1(3):192–208, 2007.
- [77] Sébastien Camalet and Frank Jülicher. Generic aspects of axonemal beating. *New Journal of Physics*, 2(1):24, 2000.
- [78] Charles W Wolgemuth, Thomas R Powers, and Raymond E Goldstein. Twirling and whirling: Viscous dynamics of rotating elastic filaments. *Physical Review Letters*, 84(7):1623, 2000.
- [79] Chris H. Wiggins and Raymond E. Goldstein. Flexive and propulsive dynamics of elastica at low reynolds number. *Phys. Rev. Lett.*, 80:3879–3882, Apr 1998.
- [80] Chris H Wiggins, D Riveline, Albrecht Ott, and Raymond E Goldstein. Trapping and wiggling: Elastohydrodynamics of driven microfilaments. *Biophysical Journal*, 74(2):1043–1060, 1998.
- [81] Eric Lauga. Life around the scallop theorem. *Soft Matter*, 7:3060–3065, 2011.
- [82] D Riveline, Chris H Wiggins, RE Goldstein, and A Ott. Elastohydrodynamic study of actin filaments using fluorescence microscopy. *Physical Review E*, 56(2):R1330, 1997.
- [83] M Cosentino Lagomarsino, F Capuani, and CP Lowe. A simulation study of the dynamics of a driven filament in an aristotelian fluid. *Journal of Theoretical Biology*, 224(2):215–224, 2003.
- [84] Christopher P Lowe. Dynamics of filaments: modelling the dynamics of driven microfilaments. *Philosophical Transactions of the Royal Society of London B: Biological Sciences*, 358(1437):1543–1550, 2003.
- [85] KE Machin. Wave propagation along flagella. *Journal of Experimental Biology*, 35(4):796–806, 1958.
- [86] KE Machin. The control and synchronization of flagellar movement. In *Proc. R. Soc. Lond. B*, volume 158, pages 88–104. The Royal Society, 1963.
- [87] Yong Woon Kim and Roland R Netz. Pumping fluids with periodically beating grafted elastic filaments. *Physical review letters*, 96(15):158101, 2006.
- [88] Gábor Kósa, Moshe Shoham, and Menashe Zaaroor. Propulsion of a swimming micro medical robot. In *Robotics and Automation, 2005. ICRA 2005. Proceedings of the 2005 IEEE International Conference on*, pages 1327–1331. IEEE, 2005.
- [89] Marcus Roper, Rémi Dreyfus, Jean Baudry, Marc Fermigier, Jérôme Bibette, and Howard A Stone. On the dynamics of magnetically driven elastic filaments. *Journal of Fluid Mechanics*, 554:167–190, 2006.

- [90] Yanlei Yu, Makoto Nakano, and Tomiki Ikeda. Photomechanics: directed bending of a polymer film by light. *Nature*, 425(6954):145–145, 2003.
- [91] Anatoly Malevanets and Raymond Kapral. Mesoscopic model for solvent dynamics. *The Journal of chemical physics*, 110(17):8605–8613, 1999.
- [92] Anatoly Malevanets and Raymond Kapral. Solute molecular dynamics in a mesoscale solvent. *The Journal of Chemical Physics*, 112(16):7260–7269, 2000.
- [93] Yingzi Yang, Jens Elgeti, and Gerhard Gompper. Cooperation of sperm in two dimensions: Synchronization, attraction, and aggregation through hydrodynamic interactions. *Phys. Rev. E*, 78:061903, Dec 2008.
- [94] Matthew T Downton and Holger Stark. Simulation of a model microswimmer. *Journal of Physics: Condensed Matter*, 21(20):204101, 2009.
- [95] Andreas Zöttl and Holger Stark. Nonlinear dynamics of a microswimmer in poiseuille flow. *Physical review letters*, 108(21):218104, 2012.
- [96] Sujin B Babu and Holger Stark. Modeling the locomotion of the african trypanosome using multi-particle collision dynamics. *New Journal of Physics*, 14(8):085012, 2012.
- [97] Jinglei Hu, Mingcheng Yang, Gerhard Gompper, and Roland G Winkler. Modelling the mechanics and hydrodynamics of swimming e. coli. *Soft matter*, 11(40):7867–7876, 2015.
- [98] Jan L Münch, Davod Alizadehrad, Sujin B Babu, and Holger Stark. Taylor line swimming in microchannels and cubic lattices of obstacles. *Soft matter*, 12(35):7350–7363, 2016.
- [99] Mario Theers, Elmar Westphal, Gerhard Gompper, and Roland G Winkler. Modeling a spheroidal microswimmer and cooperative swimming in a narrow slit. *Soft matter*, 12(35):7372–7385, 2016.
- [100] Jens Elgeti, U Benjamin Kaupp, and Gerhard Gompper. Hydrodynamics of sperm cells near surfaces. *Biophysical journal*, 99(4):1018–1026, 2010.
- [101] Raymond Kapral. Multiparticle collision dynamics: simulation of complex systems on mesoscales. *Advances in Chemical Physics*, 140:89, 2008.
- [102] G. Gompper, T. Ihle, D. M. Kroll, and R. G. Winkler. *Multi-Particle Collision Dynamics: A Particle-Based Mesoscale Simulation Approach to the Hydrodynamics of Complex Fluids*, pages 1–87. Springer Berlin Heidelberg, Berlin, Heidelberg, 2009.
- [103] T Ihle and DM Kroll. Stochastic rotation dynamics: a galilean-invariant mesoscopic model for fluid flow. *Physical Review E*, 63(2):020201, 2001.
- [104] Thomas Ihle and Daniel M Kroll. Stochastic rotation dynamics. i. formalism, galilean invariance, and green-kubo relations. *Physical Review E*, 67(6):066705, 2003.
- [105] Tongyang Zhao, Xiaogong Wang, Lei Jiang, and Ronald G Larson. Assessment of mesoscopic particle-based methods in microfluidic geometries. *The Journal of chemical physics*, 139(8):084109, 2013.

- [106] Michael P Allen et al. Introduction to molecular dynamics simulation. *Computational soft matter: from synthetic polymers to proteins*, 23:1–28, 2004.
- [107] Robert D Groot and Patrick B Warren. Dissipative particle dynamics: Bridging the gap between atomistic and mesoscopic simulation. *The Journal of chemical physics*, 107(11):4423–4435, 1997.
- [108] Thomas Soddemann, Burkhard Dünweg, and Kurt Kremer. Dissipative particle dynamics: A useful thermostat for equilibrium and nonequilibrium molecular dynamics simulations. *Physical Review E*, 68(4):046702, 2003.
- [109] Hiroshi Noguchi, Norio Kikuchi, and Gerhard Gompper. Particle-based mesoscale hydrodynamic techniques. *EPL (Europhysics Letters)*, 78(1):10005, 2007.
- [110] Hiroshi Noguchi and Gerhard Gompper. Transport coefficients of dissipative particle dynamics with finite time step. *EPL (Europhysics Letters)*, 79(3):36002, 2007.
- [111] Hiroshi Noguchi and Gerhard Gompper. Transport coefficients of off-lattice mesoscale-hydrodynamics simulation techniques. *Physical Review E*, 78(1):016706, 2008.
- [112] Ingo O Götze, Hiroshi Noguchi, and Gerhard Gompper. Relevance of angular momentum conservation in mesoscale hydrodynamics simulations. *Physical Review E*, 76(4):046705, 2007.
- [113] A. Lamura and G. Gompper. Numerical study of the flow around a cylinder using multi-particle collision dynamics. *Eur. Phys. J. E*, 9(5):477–485, 2002.
- [114] JT Padding, A Wysocki, H Löwen, and AA Louis. Stick boundary conditions and rotational velocity auto-correlation functions for colloidal particles in a coarse-grained representation of the solvent. *Journal of Physics: Condensed Matter*, 17(45):S3393, 2005.
- [115] Dan S. Bolintineanu, Jeremy B. Lechman, Steven J. Plimpton, and Gary S. Grest. No-slip boundary conditions and forced flow in multiparticle collision dynamics. *Phys. Rev. E*, 86:066703, Dec 2012.
- [116] A Lamura, TW Burkhardt, and G Gompper. Semiflexible polymer in a uniform force field in two dimensions. *Physical Review E*, 64(6):061801, 2001.
- [117] Antonio Lamura, Gerhard Gompper, Thomas Ihle, and DM Kroll. Multi-particle collision dynamics: Flow around a circular and a square cylinder. *EPL (Europhysics Letters)*, 56(3):319, 2001.
- [118] E Allahyarov and G Gompper. Mesoscopic solvent simulations: Multiparticle-collision dynamics of three-dimensional flows. *Physical Review E*, 66(3):036702, 2002.
- [119] L Cannavacciuolo, RG Winkler, and G Gompper. Mesoscale simulations of polymer dynamics in microchannel flows. *EPL (Europhysics Letters)*, 83(3):34007, 2008.
- [120] N Kikuchi, A Gent, and JM Yeomans. Polymer collapse in the presence of hydrodynamic interactions. *The European Physical Journal E: Soft Matter and Biological Physics*, 9(1):63–66, 2002.

- [121] N Kikuchi, CM Pooley, JF Ryder, and JM Yeomans. Transport coefficients of a mesoscopic fluid dynamics model. *The Journal of chemical physics*, 119(12):6388–6395, 2003.
- [122] I Ali, D Marenduzzo, and JM Yeomans. Dynamics of polymer packaging. *The Journal of chemical physics*, 121(17):8635–8641, 2004.
- [123] I Ali and JM Yeomans. Polymer translocation: The effect of backflow. *The Journal of chemical physics*, 123(23):234903, 2005.
- [124] I Ali, D Marenduzzo, and JM Yeomans. Ejection dynamics of polymeric chains from viral capsids: effect of solvent quality. *Biophysical journal*, 94(11):4159–4164, 2008.
- [125] Andrew Cressman, Yuichi Togashi, Alexander S Mikhailov, and Raymond Kapral. Mesoscale modeling of molecular machines: cyclic dynamics and hydrodynamical fluctuations. *Physical Review E*, 77(5):050901, 2008.
- [126] SB Babu and H Stark. Dynamics of semi-flexible tethered sheets. *The European Physical Journal E: Soft Matter and Biological Physics*, 34(12):1–7, 2011.
- [127] Sujin B. Babu, Christian Schmeltzer, and Holger Stark. Swimming at low reynolds number: From sheets to the african trypanosome. *Notes Numer. Fluid Mech. Multidiscip. Des.*, 119:25–41, 2012.
- [128] M.P. Allen and D.J. Tildesley. *Computer Simulation of Liquids*. Oxford: Clarendon Pr, 1987.
- [129] D.C. Rapaport. *The Art of Molecular Dynamics Simulation*. Cambridge University Press, 2004.
- [130] Daan Frenkel and Berend Smit. *Understanding molecular simulation: From algorithms to applications*, 2002.
- [131] A. Malevanets and J. M. Yeomans. Dynamics of short polymer chains in solution. *EPL (Europhysics Letters)*, 52(2):231, 2000.
- [132] Hiroshi Noguchi and Gerhard Gompper. Dynamics of fluid vesicles in shear flow: Effect of membrane viscosity and thermal fluctuations. *Physical Review E*, 72(1):011901, 2005.
- [133] JT Padding and AA Louis. Hydrodynamic interactions and brownian forces in colloidal suspensions: Coarse-graining over time and length scales. *Physical Review E*, 74(3):031402, 2006.
- [134] Bryce T. McLelland Michael Oberholzer, Miguel A. Lopez and Kent L. Hill. Social motility in African trypanosomes. *PLoS Pathogens*, 6(1):1000739, 2010.
- [135] A Pacey, J Cosson, and M Bentley. The acquisition of forward motility in the spermatozoa of the polychaete arenicola marina. *Journal of experimental Biology*, 195(1):259–280, 1994.
- [136] J E Avron and O Raz. A geometric theory of swimming: Purcell’s swimmer and its symmetrized cousin. *New Journal of Physics*, 10(6):063016, 2008.
- [137] Edward M Purcell. The efficiency of propulsion by a rotating flagellum. *Proceedings of the National Academy of Sciences*, 94(21):11307–11311, 1997.

- [138] Daniel A. P. Reid, H. Hildenbrandt, J. T. Padding, and C. K. Hemelrijk. Fluid dynamics of moving fish in a two-dimensional multiparticle collision dynamics model. *Phys. Rev. E*, 85:021901, Feb 2012.
- [139] Knut Drescher, Raymond E. Goldstein, Nicolas Michel, Marco Polin, and Idan Tuval. Direct measurement of the flow field around swimming microorganisms. *Phys. Rev. Lett.*, 105:168101, Oct 2010.
- [140] Andreas Zöttl and Holger Stark. Hydrodynamics determines collective motion and phase behavior of active colloids in quasi-two-dimensional confinement. *Phys. Rev. Lett.*, 112:118101, Mar 2014.
- [141] J Elgeti, R G Winkler, and G Gompper. Physics of microswimmers—single particle motion and collective behavior: a review. *Reports on Progress in Physics*, 78(5):056601, 2015.
- [142] Prohm, C., Gierlak, M., and Stark, H. Inertial microfluidics with multi-particle collision dynamics. *Eur. Phys. J. E*, 35(8):80, 2012.
- [143] Raymond E Goldstein. Green algae as model organisms for biological fluid dynamics. *Annual review of fluid mechanics*, 47, 2015.
- [144] Tian Qiu, Tung-Chun Lee, Andrew G Mark, Konstantin I Morozov, Raphael Münster, Otto Mierka, Stefan Turek, Alexander M Leshansky, and Peer Fischer. Swimming by reciprocal motion at low reynolds number. *Nature communications*, 5:5119, 2014.
- [145] Niko Heddergott, Timothy Krüger, Sujin B Babu, Ai Wei, Erik Stellamanns, Sravanti Uppaluri, Thomas Pfohl, Holger Stark, and Markus Engstler. Trypanosome motion represents an adaptation to the crowded environment of the vertebrate bloodstream. *PLoS Pathog*, 8(11):e1003023, 2012.
- [146] Christopher Brennen and Howard Winet. Fluid mechanics of propulsion by cilia and flagella. *Annual Review of Fluid Mechanics*, 9(1):339–398, 1977.
- [147] Ambarish Ghosh and Peer Fischer. Controlled propulsion of artificial magnetic nanostructured propellers. *Nano letters*, 9(6):2243–2245, 2009.
- [148] Andrew G Mark, John G Gibbs, Tung-Chun Lee, and Peer Fischer. Hybrid nanocolloids with programmed three-dimensional shape and material composition. *Nature materials*, 12(9):802, 2013.
- [149] Priyanka Choudhary, Subhayan Mandal, and Sujin B. Babu. Locomotion of a flexible one-hinge swimmer in stokes regime, 2017.
- [150] E. Lauga. Life at high Deborah number. *EPL (Europhysics Letters)*, 86(6):64001, 2009.
- [151] Renaud Trouilloud, Tony S. Yu, A. E. Hosoi, and Eric Lauga. Soft swimming: Exploiting deformable interfaces for low reynolds number locomotion. *Phys. Rev. Lett.*, 101:048102, Jul 2008.
- [152] David Gonzalez-Rodriguez and Eric Lauga. Reciprocal locomotion of dense swimmers in stokes flow. *Journal of Physics: Condensed Matter*, 21(20):204103, 2009.
- [153] Eric Lauga. Enhanced diffusion by reciprocal swimming. *Physical review letters*, 106(17):178101, 2011.

- [154] Adam W Feinberg, Alex Feigel, Sergey S Shevkoplyas, Sean Sheehy, George M Whitesides, and Kevin Kit Parker. Muscular thin films for building actuators and powering devices. *Science*, 317(5843):1366–1370, 2007.
- [155] J.K.G. Dhont. *An Introduction to Dynamics of Colloids*. Elsevier Science, 1996.
- [156] Eric Lauga, Willow R DiLuzio, George M Whitesides, and Howard A Stone. Swimming in circles: motion of bacteria near solid boundaries. *Biophysical journal*, 90(2):400–412, 2006.
- [157] Rasika M Harshey. Bacterial motility on a surface: many ways to a common goal. *Annual Reviews in Microbiology*, 57(1):249–273, 2003.
- [158] J Cosson, P Huitorel, and C Gagnon. How spermatozoa come to be confined to surfaces. *Cytoskeleton*, 54(1):56–63, 2003.
- [159] Allison P Berke, Linda Turner, Howard C Berg, and Eric Lauga. Hydrodynamic attraction of swimming microorganisms by surfaces. *Physical Review Letters*, 101(3):038102, 2008.
- [160] Rojman Zargar, Ali Najafi, and MirFaez Miri. Three-sphere low-reynolds-number swimmer near a wall. *Physical Review E*, 80(2):026308, 2009.
- [161] Darren G Crowdy and Yizhar Or. Two-dimensional point singularity model of a low-reynolds-number swimmer near a wall. *Physical Review E*, 81(3):036313, 2010.
- [162] J Happel. H., brenner. *Low Reynolds Number Hydrodynamics*, Prentice-Hall, Englewood Cliffs, NJ, 133, 1965.
- [163] S Kim and S Karrila. J. 1991 microhydrodynamics: Principles and selected applications.

Appendix

Publications from thesis work

1. **Priyanka Choudhary**, Subhayan Mandal, Sujin. B. Babu, Locomotion of a flexible one-hinge swimmer in Stokes regime, *Journal of Physics communications*, **2** (2018) 2.
2. **Priyanka Choudhary**, Subhayan Mandal, Non self-propelled swimmer in a confined viscous fluid, *AIP Conference Proceedings*, **1953** (2018) 1.
3. **Priyanka Choudhary**, Subhayan Mandal, Sujin Babu, Swimming of a Waving sheet in Viscous fluid, *Macromolecular Symposia*, **376** (2017) 1.

